A study on identifiability of fracture properties of concrete given experimental data

Simona Dobrilla

Par **Simona DOBRILLA**

A study on identifiability of fracture properties of concrete given experimental data

Thèse présentée en cotutelle pour l'obtention du grade de Docteur de l'UTC

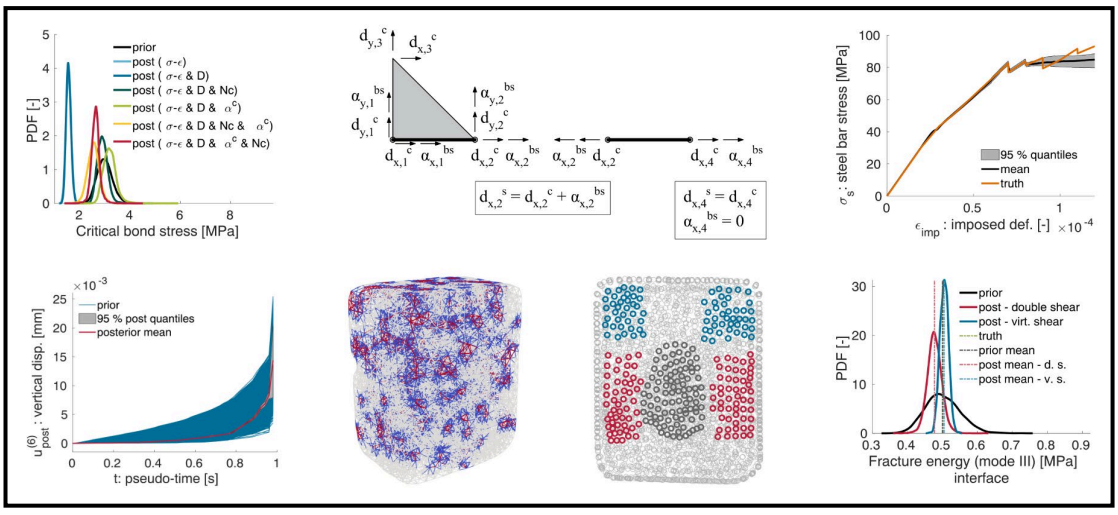

Soutenue le 14 juillet 2022

Spécialité : Mécanique Numérique : Unité de recherche en Mécanique - Laboratoire Roberval (FRE UTC - CNRS 2012)

D2696

A STUDY ON IDENTIFIABILITY OF FRACTURE PROPERTIES OF CONCRETE GIVEN EXPERIMENTAL DATA

Thèse

Spécialité : Mécanique Numérique

approved by the

Faculty of Architecture, Civil Engineering and Environmental Sciences

Universität Braunschweig – Institute of Technology

in Cotutelle with the

Roberval Laboratory, University of Technology of Compiègne

Sorbonne University

in candidacy for the degree of a

Doktor-Ingenieurin (Dr.-Ing.) /

Docteur de l'Université de Technologie de Compiègne *)

by Simona DOBRILLA

Defended on July 14, 2022

Professorial advisors :

Prof. Hermann G. Matthies, Ph.D.
Prof. Adnan Ibrahimbegovic, Ph.D.

*) Only one of both titles may be used.

The doctoral thesis was defended on July 14, 2022 at the Technical University of Braunschweig, in front of the committee members:

Reviewers:

- **Prof. Anna Kučerová**, Faculty of Civil Engineering, Czech Technical University in Prague, Czech Republic,
- **Prof. Ivica Kožar**, Faculty of Civil Engineering, University of Rijeka, Croatia.

Members of the jury:

- **Prof. Ursula Kowalsky**, Institute of Structural Analysis, Technical University of Braunschweig, Germany,
- **Prof. Delphine Brancherie**, University of Technology of Compiègne, Sorbonne University, France,
- **Prof. Pavao Marović**, Faculty of Civil Engineering, Architecture and Geodesy, University of Split, Croatia,
- **Asst. Prof. Mijo Nikolić**, Faculty of Civil Engineering, Architecture and Geodesy, University of Split, Croatia,
- **Prof. Adnan Ibrahimbegovic**, University of Technology of Compiègne, Sorbonne University, France,
- **Prof. Hermann G. Matthies**, Institute of Scientific Computing, Technical University of Braunschweig, Germany.

Invited:

- **Prof. Manfred Krafczyk**, Institute for Computational Modeling in Civil Engineering, Technical University of Braunschweig, Germany,
- **Asst. Prof. Andjelka Stanić**, Faculty of Engineering Technology, University of Twente, The Netherlands.

"When artists create pictures and thinkers search for laws and formulate thoughts, it is in order to salvage something from the great dance of death, to make something last longer than we do."

H. Hesse, *Narcissus and Goldmund*

Abstract

Ageing and deterioration of reinforced concrete structures are ongoing problems of a main concern. The state of building materials is changing over the service life of structures, thereby affecting the structural reliability and durability.

Numerical models are a powerful tool for the assessment of safety and serviceability of existing structures. However, regardless of the level of model complexity, they are merely an approximation of the real systems. Hence, any model prediction is characterised by a certain degree of uncertainty. To improve the predictive capabilities, numerical models need to be enriched with the description of uncertainties, which can further be reduced by gathering the available information about the observed structure.

In this work, a probabilistic framework for parameter estimation in nonlinear mechanical models and a study on identifiability are proposed. The parameter estimation is based on Bayesian inference, which combines both the prior knowledge and information from experimental data to reduce the uncertainty in the probabilistic description of uncertain model parameters. Moreover, the goal is to find optimal experiments from the point of view of parameter identifiability, ease of implementation and the associated costs.

Bayesian inference, in its filtering form, is applied for parameter estimation of uncertain mechanical properties in both plain and reinforced concrete, with the focus on fracture and bond parameters governing the crack propagation and bond-slip. For that purpose, observational data (i.e. stress-deformation curve, displacement field) from uniaxial tensile tests on reinforced concrete beams and double shear experiments on mortar specimen are used. Issues of parameter identifiability, shortcomings and challenges which arise due to peculiarities of the experimental setup are addressed and alternative experimental designs which increase the sensitivity with respect to parameters of interest and subsequently, reduce the discrepancy between the computed and observed quantities of interest, are proposed.

Reduction of the epistemic uncertainty via Bayesian inference leads to more accurate estimates of the system parameters and state and thereby allows more reliable predictions of the system's future state. This matter is very important from the point of view of structural durability and integrity.

Zusammenfassung

Die Alterung und der Verfall von Stahlbetonkonstruktionen sind ein ständiges Problem, das Anlass zu großer Sorge gibt. Der Zustand der Baumaterialien ändert sich im Laufe der Lebensdauer der Bauwerke, was sich auf die Zuverlässigkeit und Dauerhaftigkeit der Bauwerke auswirkt.

Numerische Modelle sind ein leistungsfähiges Instrument für die Bewertung der Sicherheit und Gebrauchstauglichkeit bestehender Bauwerke. Unabhängig vom Grad der Modellkomplexität stellen sie jedoch lediglich eine Annäherung an die realen Systeme dar. Daher ist jede Modellvorhersage mit einem gewissen Grad an Unsicherheit behaftet. Um die Vorhersagefähigkeiten zu verbessern, müssen numerische Modelle mit der Beschreibung von Unsicherheiten angereichert werden, die durch das Sammeln der verfügbaren Informationen über die beobachtete Struktur weiter reduziert werden können.

In dieser Arbeit werden ein probabilistischer Rahmen für die Parameterschätzung in nichtlinearen mechanischen Modellen und eine Studie zur Identifizierbarkeit vorgeschlagen. Die Parameterschätzung basiert auf Bayes'scher Inferenz, die sowohl das Vorwissen als auch Informationen aus experimentellen Daten kombiniert, um die Unsicherheit in der probabilistischen Beschreibung unsicherer Modellparameter zu reduzieren. Darüber hinaus ist es das Ziel, optimale Experimente unter den Gesichtspunkten der Parameteridentifizierbarkeit, der einfachen Implementierung und der damit verbundenen Kosten zu finden.

Die Bayes'sche Inferenz wird in ihrer Filterform für die Parameterschätzung unsicherer mechanischer Eigenschaften sowohl in einfachem als auch in bewehrtem Beton angewandt, wobei der Schwerpunkt auf Bruch- und Verbundparametern liegt, die die Rissausbreitung und den Verbundschlupf bestimmen. Zu diesem Zweck werden Beobachtungsdaten (d.h. Spannungs-Verformungs-Kurve, Verschiebungsfeld) aus einachsigen Zugversuchen an Stahlbetonbalken und Doppelscherexperimenten an Mörtelproben verwendet. Fragen der Identifizierbarkeit von Parametern, Unzulänglichkeiten und Herausforderungen, die sich aus den Besonderheiten des Versuchsaufbaus ergeben, werden angesprochen, und es werden alternative Versuchspläne vorgeschlagen, die die Empfindlichkeit in Bezug auf die interessierenden Parameter erhöhen und folglich die Diskrepanz zwischen den berechneten und den beobachteten interessierenden Größen verringern.

Die Verringerung der epistemischen Unsicherheit durch Bayes'sche Inferenz führt zu genaueren Schätzungen der Systemparameter und des Systemzustands und ermöglicht somit zuverlässigere Vorhersagen über den zukünftigen Zustand des Systems. Dieser Aspekt ist unter dem Gesichtspunkt der strukturellen Dauerhaftigkeit und Integrität sehr wichtig.

Résumé étendu

Le vieillissement et la détérioration des structures en béton armé sont des problèmes permanents qui constituent une préoccupation majeure. L'état des matériaux de construction évolue au cours de la durée de vie des structures, ce qui affecte la fiabilité et la durabilité des structures.

Les modèles numériques sont un outil puissant pour l'évaluation de la sécurité et de l'aptitude au service des structures existantes. Cependant, quel que soit le niveau de complexité du modèle, ils ne sont qu'une approximation des systèmes réels. Par conséquent, toute prédiction de modèle est caractérisée par un certain degré d'incertitude. Pour améliorer les capacités de prédiction, les modèles numériques doivent être enrichis par la description des incertitudes, qui peuvent être réduites en rassemblant les informations disponibles sur la structure observée.

Dans ce travail, un cadre probabiliste pour l'estimation des paramètres dans les modèles mécaniques non linéaires et une étude sur l'identifiabilité sont proposés. L'estimation des paramètres est basée sur l'inférence bayésienne, qui combine à la fois les connaissances préalables et les informations provenant des données expérimentales pour réduire l'incertitude dans la description probabiliste des paramètres incertains du modèle. En outre, l'objectif est de trouver des expériences optimales du point de vue de l'identifiabilité des paramètres, de la facilité de mise en uvre et des coûts associés.

L'inférence bayésienne, sous sa forme filtrante, est appliquée à l'estimation des paramètres des propriétés mécaniques incertaines du béton et du béton armé, en mettant l'accent sur les paramètres de rupture et de liaison régissant la propagation des fissures et le glissement de liaison. À cette fin, des données d'observation (c'est-à-dire la courbe contrainte-déformation, le champ de déplacement) provenant d'essais de traction uniaxiale sur des poutres en béton armé et d'expériences de double cisaillement sur des spécimens de mortier sont utilisées. Les questions d'identifiabilité des paramètres, les lacunes et les défis qui surviennent en raison des particularités de la configuration expérimentale sont abordés et des conceptions expérimentales alternatives qui augmentent la sensibilité par rapport aux paramètres d'intérêt et, par la suite, réduisent l'écart entre les quantités d'intérêt calculées et observées, sont proposées.

La réduction de l'incertitude épistémique via l'inférence bayésienne conduit à des estimations plus précises des paramètres et de l'état du système et

permet ainsi des prédictions plus fiables de l'état futur du système. Cette question est très importante du point de vue de la durabilité et de l'intégrité des structures.

Acknowledgements

First and foremost, I would like to express my sincere gratitude to my doctoral advisors, Prof. Hermann G. Matthies and Prof. Adnan Ibrahimbegovic, for giving me the opportunity to work on this interesting topic and develop myself as a researcher. I am heartily thankful to Prof. Matthies for his guidance, understanding and empathy. His passion for research has inspired me to become very keen on the study of stochastic problems. I am grateful for all the help from Prof. Ibrahimbegovic, who unselfishly shared his knowledge and ideas and challenged me to continue to thrive.

This thesis would not have been possible without the financial, academic and technical support of the Research Training Group Graduiertenkolleg GRK2075 and German Research Foundation (DFG), whose contribution is greatly acknowledged. I would like to thank Prof. Dr.-Ing. Dieter Dinkler and Prof. Dr.-Ing. Manfred Krafczyk for accepting me as a member of the GRK2075 group. The training activities I had the opportunity to attend and precious feedback from numerous workshops have greatly enriched my research and me as a young researcher.

I want to thank Matteo Lunardelli, Prof. Bojana Rosić and Dr. Mijo Nikolić, who contributed to a part of the work presented in this thesis. I appreciate our long discussions from which I learned a lot. Thank you for providing such great and motivating work environment. I am grateful to Dr. Noémi Friedman, who helped me to get familiar with the field of stochastics and Alexey Kiriyenko, who was always there to help with any technical issues.

PhD is never only about the research work, though. It is a time of personal growth and an emotional roller coaster, which is much easier to bare when surrounded by colleagues who are understanding and motivating. Their kind words and precious support have helped the completion of this work more than they could have imagined. A very personal thank you to Bojana, who was not only a colleague and a collaborator, but a true friend and huge support during this whole journey. Not only did I learn so much from her, but she has always been such an inspiration. I am forever grateful to Cosima for her help with the endless paperwork and for taking care of me and standing up for me, especially in the beginning when everything was new and overwhelming. A special thank you to Sharana, with whom I shared the office throughout my whole PhD journey and who was always there to share both happy and difficult moments. I also want to thank the whole WiRe and

Roberval group for the unforgettable time and memories that will stay with me forever. Particularly, I am thankful to Andjelka, for numerous discussions about mechanics and her kind words of motivation when I struggled with my research as well as the whole Italian group, with whom our big office was much happier. Sincere thanks to Adela and Cong Uy who have kindly welcomed me in Compiègne and for our many fruitful conversations about work and life.

Lastly, but not least, I am grateful to my family and friends, for their love, patience and support. You kept me going forward.

Simona Dobrilla
Braunschweig, May 2022

Contents

Chapter 1

Introduction

Numerical models are extensively used for predicting and assessing the behaviour of real systems. In the context of structural durability, they are powerful tools for the assessment of safety and serviceability of existing structures. Advances in computer technology facilitate the use of more complex numerical models. However, regardless of the level of complexity, numerical models are merely an approximation of complex multi-dimensional reality. This stems from the fact that our understanding and knowledge about the real-world phenomena is scarce and imprecise and computing resources are rather limited. In regard to civil engineering structures, there is a significant amount of uncertainty associated with the design process, modelling and construction. Namely, in real-world problems neither the strength of a structure, loads nor internal effects during the structure life-time can be predicted accurately. Due to changes in usage, the actual loads may differ from the predicted ones in magnitude and distribution. Moreover, 2D models which are commonly used due to their simplicity are not an exact description of real 3D structures and hence the predicted state may deviate from the actual one. The choice of material laws within the predictive models plays an important role in results of numerical simulations. In the construction process, reinforced concrete structures may have initial defects which are not accounted for in the analysis and the strength of the material may differ from the design strength or its magnitude may vary within structure itself. In engineering practice, this is usually compensated implicitly by introducing the safety factors.

Reinforced concrete structures are designed to withstand the external ac-

tions throughout an expected service life of 50-100 years. This forecast holds true under assumption of an ideal state of building materials and structural members throughout the whole lifespan. In practice, however, state of the material (e.g. its mechanical properties) changes over the period of use due to ageing induced defects, which may impair the structural safety by causing a decrease in resistance of structures to external impacts. As the material is deteriorating due to ageing, once small discontinuities propagate and become more prominent, leading to significant reduction of structural durability. Due to its low tensile strength, development of cracks in concrete is inevitable. The first cracks may appear even prior to load application as a result of restrained shrinkage. Formation of cracks further evolves at loads substantially below the service limit, with an increase in loading followed by the increase in number of cracks and their widths. Cracking in concrete is affected by many different factors, among others by its highly heterogeneous mesostructure, causing the crack patterns to significantly vary within a population of structural members which share the same geometric and mechanical characteristics.

Considering the aforementioned sources of uncertainty present in different aspects of the structural life, from design and numerical analysis to construction and ageing, the choice of model input parameters and their values, as well as modelling and measurement error cannot be specified with absolute certainty. Correspondingly, numerical models may produce imperfect estimates of the desired responses (e.g. deflections, crack widths) in the presence of uncertainties. In order to improve their predictive capabilities, numerical models need to be enriched with a proper description of uncertainties, defining the so-called *stochastic models*.

The aim of stochastic models is to capture and quantify the uncertainty in the model inputs and the respective outputs. In this regard, uncertain model parameters are modelled as *random variables* (RV) or *random fields* (RF), the probabilistic description of which reflects the lack of knowledge about their true values. The uncertainty in the model inputs, and possibly boundary and initial conditions, is further propagated through the computational model defining the so-called *stochastic forward problem*, the aim of which is to produce estimates of the measurements given model inputs. The *stochastic inverse problem*, on the other hand, is tackled by comparing the measurement forecast from the forward problem with the actual data. Inverse problems are usually ill-posed as many different combinations of parameters may lead to the same output, the input parameters may be sensitive to the observation or an actual observation may be out of range of the observation operator, which

leads to the observation operator being not invertible. Taking a *Bayesian* viewpoint alleviates these issues and transforms an ill-posed inverse problem into a well-posed one with a stochastic solution, where prior information acts as a regularising term. The resulting posterior probability distributions may be obtained either by the sampling-based Monte Carlo (MC) methods or the highly efficient alternative combining filtering techniques and functional approximations.

The choice of measurements used for Bayesian inference of uncertain model parameters is conditioned by the parameters one seeks to identify. An optimal experiment provides the highest information gain from the data and leads to accurate posterior estimates. The ability to correctly estimate the model parameters from the observed data, known as the parameter *identifiability*, thus becomes an important aspect of parameter estimation. To achieve the best possible estimates of the target parameters and subsequently minimise the discrepancy between the predicted and the observed *quantities of interest* (QoI), sometimes requires integration of datasets from experiments of a different type. For instance, dissipation and local quantities, such as crack opening, may yield more information about the properties related to fracture. On contrary, the global observations, such as the force-displacement curve, may be more suitable for inference of elastic properties. Improved parameter identifibility, ultimately resulting in more accurate estimates of the system parameters and state, allows more reliable predictions of the system's future state, which is very important from the point of view of structural durability and estimation of service life of structures.

1.1 State of the art

Parameter identification is a commonly used procedure, the intent of which is to reduce the uncertainty in unknown model inputs, such that the discrepancies between the predictions of the model output and actual structural observations are minimised. The used methodology usually relies on two major approaches: deterministic procedures which are based on mathematical *optimisation* and probabilistic procedures relying on *Bayes' theorem*.

In deterministic approach, a set of unknown model inputs is typically sought by minimising a cost function defined as a spatial and temporal sum of the difference between the model forecast and the actual observations. This approach often relies on a gradient-based or evolutionary algorithms. A number

of works featuring the aforementioned approach in the context of structural durability can be found in literature. Gajewski and Garbowski [48] calibrated the material parameters of concrete using a minimisation gradient-based algorithm and observations from digital image correlation. Král et al. [95, 94] have used the global optimisation procedure known as evolutionary algorithm and experimental data from a tensile test to find the optimal parameters of a Continuous Surface Cap Model, a nonlinear material model of concrete. Schnur and Zabaras [158] have estimated the elastic material properties as well as position and size of the circular inclusions in a large-deformation problem using a method which incorporates constrained optimisation and finite element analysis with automatic mesh generation. Sarhosis and Sheng [152] have employed an optimisation procedure to calibrate the masonry material parameters by minimising the discrepancy between the responses measured from the large scale tests and their computationally obtained counterparts. Similar work has been done by Morbiducci [119], using a Levenberg-Marquardt based minimisation method to estimate parameters of interface and continuum model for brick masonry using monotonic and cyclic experimental data. Karimpour and Rahmatalla [89] performed a structural model updating based on minimisation techniques to determine the system parameters and boundary conditions for the structural health monitoring applications. Kučerová et al. [98] have applied a combination of the radial basis function network and an evolutionary algorithm GRADE to address the identification of material parameters in a damage model using data from a virtual uniaxial tensile test and a three-point bending test. Deterministic approaches to parameter calibration are advantageous due to their straightforward implementation and low computational cost. However, they lack the ability to account for the probabilistic aspects of the unknown model parameters.

In contrast to deterministic approaches, which search for a single optimal value of target parameters, stochastic parameter estimation describes a whole ensemble of plausible values given experimental data. Hence, values of the target parameters are given in terms of probability distributions, from which one can deduce the relevant quantities, such as mean and confidence intervals for the chosen quantities of interest. See e.g. [153] for an overview of application of stochastic parameter estimation techniques to the practical problems in mechanical systems.

Bayesian approach to parameter identification of the mechanical models stems from the work of Isenberg [77], who proposed a procedure for identification of elastic parameters governing the behaviour of a linear elastic

model. Subsequently, the proposed Bayesian identification framework has been applied for estimation of elastic parameters in various linear problems. Daghia et al. [31] have used the Bayesian and maximum variance estimators to identify the elastic constants of thick laminated composite plates in a dynamic setting. Arnst et al. [9] have modelled the Young's modulus of an elastic and isotropic material as a random field using the spectral approximation and identified its posterior polynomial chaos coefficients by the Markov chain Monte Carlo method. In a similar manner, Koutsourelakis [91] identified the spatially varying elastic constants using the same estimation method. Gogu et al. [55] have identified the elastic constants in a simple three-bar truss example and shown the superior performance of the Bayesian inference in comparison to the deterministic least-squares approach. Recursive identification of elastic constants of an anisotropic material by means of the Kálmán filter was explored in the work of Furukawa and Pan [47].

In the last decade, the Bayesian approach has been extended to more complex models accounting for the inelastic behaviour of civil engineering materials and composites, such as viscoelasticity, viscoplasticity, elastoplasticity and damage models. Rappel et al. [140] employed the Markov chain Monte Carlo method to estimate the parameters of a viscoelastic model using virtual uniaxial tensile relaxation, constant strain-rate and creep tests. Adeli et al. [3] identified parameters of a viscoplastic-damage model using different Bayesian inference methods. Inference of elastoplastic material parameters of one-dimensional single spring is tackled in the works of Rappel et al. [141, 142] using data from a virtual uniaxial tensile test and employing the sampling-based Markov chain Monte Carlo method. Rosić et al. [145] have applied the linear Bayesian update enhanced by functional approximations for estimation of material parameters of an elastoplastic model. Damage models have been addressed in the work of Waeytens and Rosić [182], where Kálmán filter is employed for the identification of a moving load on a reinforced concrete beam and the detection of damage in concrete and steel bar of the beam using observations stemming from strain sensors. In addition, the authors compare the chosen probabilistic method against deterministic Tikhonov based regularisation.

Bayesian approach has also been successfully applied to tackle the material heterogeneities. Kučerová et al. [97] have applied the stochastic Galerkin method to update the uncertainty in a coupled heat and moisture transport model in heterogeneous materials. In [73], Ibrahimbegovic et al. have identified spatially variable uncertain material parameters in an elastoplastic multi-scale model in a Bayesian manner. The work provides a probabilistic

interpretation of the size effect for dominant failure mechanism. More recent developments in the same field include the works of Ibrahimbegovic et al. [71] and Sarfaraz et al. [151], where Bayesian inference has been employed to provide the posterior probability distributions of the macro-scale uncertain parameters of a nonlinear multi-scale model for concrete. These contributions give two different interpretations of dealing with aleatoric uncertainties.

All of the above listed references have in common the use of virtual observations, rather than real experimental data generated in a laboratory or resulting from monitoring of existing structures.

Significantly smaller number of contributions relevant for the field of structural durability employs real experimental data to assess the current state of material or its parameters. Wu et al. [190] have estimated mechanical parameters of cement mortar by using Bayesian approach via incorporation of the experimental data from a three-point bending test. In [64], Hinze et al. have employed the experimental data from long-term creep tests on salt concrete to infer the parameters of a viscoelastic model. Kožar et al. [93] have estimated the bond parameters in fibre-reinforced concrete using a stochastic inverse model relying on the non-linear least squares approach with the help of the experimental fibre pull-out curves. In the more recent contribution, Kožar et al. [92] have taken a data-driven approach to recover the values of unknown model parameters of fibre-reinforced concrete beams from three-point bending tests. Similarly, Kučerová and Lepš [96] have applied an inverse procedure based on cascade Artificial Neural Networks to infer the parameters of concrete described by the M4 model [13] given a representative set of experimental data. A similar approach based on Artificial Neural Networks is employed by Mareš et al. [107] to calibrate the parameters of the affinity hydration model for concrete given simulated and experimental data. A practical application of Bayesian inference exploiting the structural health monitoring data is found in the works of Sevieri et al. [159, 160], where the in-situ measurements on an existing concrete dam are utilised to identify the elastic properties of concrete. Janouchová and Kučerová [79] have identified material parameters of a viscoplastic model of copper alloy using real experimental data from a series of cyclic loading test at high temperature. In [78], Janouchová et al. have applied the sampling-based Bayesian inference to estimate parameters of a lattice discrete particle model for concrete using experimental data from an unconfined compression cube test and notched three-point bending test. Another relevant contribution for understanding of the behaviour of concrete is given by Balaji Rao [11], in which the author

uses the alpha-stable distribution, characterised by heavy tails, to model large fluctuations in surface strain at the level of steel. The parameters of the proposed distribution are estimated from the four-point bending tests using an optimisation procedure based on minimising the sum of squares.

Parameter estimation, especially in its probabilistic form, has gained a lot of popularity in the last decades, with new research contributions emerging daily. However, the field still lacks the application to more complex mechanical models accounting for inelastic behaviour, such as damage or plasticity and bond-slip. Moreover, the field lacks the comprehensive use of actual experimental data with proper addressing of challenges which may arise due to peculiarities of the experimental setup (e.g. unknown boundary conditions). Finally, there is a lack of systematic approach, which would fuse all the stages, from the optimal experimental design and modelling to employing the gathered data for parameter estimation, and provide a comprehensive interpretation of the concept of parameter identifiability.

1.2 Scope and research relevance

Our knowledge about the characteristics and inner structure of building materials is rather incomplete. The state of materials is changing over the service life of structures due to ageing induced defects and unfavourable external effects, thereby affecting the structural reliability and durability.

Nonlinear numerical models describing the complex behaviour of materials are widely used for the study on structural durability, which is closely related to propagation of damage and cracking in structures. To improve the predictive capabilities of numerical models and as a result, the prediction of the service life of concrete structures, one has to properly address the uncertainties arising in civil engineering systems.

Hence, the primary aims of this research work are:

- to investigate the presence of uncertainties in nonlinear numerical models describing the quasi-brittle fracture in concrete and bond-slip,
- to reduce the epistemic uncertainty pertaining to target model parameters via Bayesian inference,

- to study the parameter identifiability given experimental data simulating the shear and tensile fracture in plain and reinforced concrete,
- to improve the parameter identifiability by proposing alternative experiments, which show greater sensitivity with respect to target model parameters, while bearing in mind the ease of implementation and limitations of the testing facilities, and
- to give practical solutions to the problems, which may arise when the experimental data stems from actual experiments.

In the focus of this research is the parameter identifiability, which is studied in [59, 53, 52, 183, 104, 16, 178, 177]. However, so far there is a lack of contributions which concern the nonlinear models of concrete.

1.3 Thesis outline

The thesis outline is summarised as follows:

Chapter 2 gives a general overview of the methods for modelling of uncertainties and the approaches to solving the stochastic inverse problem of parameter estimation. In focus is the Bayesian inference and its filtering formulation based on the approximation of the conditional expectation.

Chapter 3 introduces different approaches to modelling of quasi-brittle fracture in reinforced and plain concrete. In focus are the two types of numerical models which are used for computing predictions of inelastic behaviour, which are further used for uncertainty quantification and parameter estimation. First to be introduced is a predictive meso-scale 2D damage model for simulation of fracture in concrete based on embedded discontinuities, with an appropriate description of bond-slip at the concrete-steel interface. That is followed by a brief introduction to a 3D lattice model consisting of spatial Timoshenko beams with embedded dicontinuities, able to model the fracture mechanisms on a finer scale, taking into account heterogeneous mesostructure of concrete.

Chapter 4 presents the results of Bayesian inference of material parameters of a damage model for reinforced concrete. Observations from different types of experiments are combined and their influence on the posterior estimates

is discussed. Chapter concludes with the main findings on the experiments which improve the identifiability of the uncertain parameters of interest.

Chapter 5 focuses on the Bayesian inference of uncertain material parameters and load. A novel approach for the sequential Bayesian inference which does not require coupling of the computer program for stochastic analysis and the finite element solver is described. The chapter tackles the issue of parameter identifiability given real and virtual experimental data and suitability of the proposed experiments for identification of the target parameters, as well as issues stemming from the peculiarities of the experimental implementation, such as uncertainty in the boundary and loading conditions.

Chapter 6 summarises the completed work and gives an outlook.

Chapter 2

Stochastic parameter estimation in a Bayesian setting

"We are far too willing to reject the belief that much of what we see in life is random."
D. Kahneman, *Thinking, Fast and Slow*

Given a thorough description of a physical system, one can predict its behaviour for a chosen set of initial and boundary conditions. This defines the so-called *forward problem*. The *inverse problem* [170], on the other hand, involves the inference of parameters describing the underlying physical system by exploiting the outcomes of a sequence of actual observations.

In deterministic setting, the forward problem has a unique solution, but the same does not hold for its inverse counterpart. Namely, inverse problems are typically ill-posed [41] due to the fact that the observations do not contain enough information to uniquely determine the dependence on parameters. That can manifest itself in terms of the absence of a solution, the existence of a non-unique solution or a solution which is very sensitive with respect to the output or noise. In order to achieve the uniqueness of the solution, additional information has to be provided. In an attempt to avoid applying some regularisation procedure (e.g. *Tikhonov regularisation*, see [173, 174]), a deterministic ill-posed problem in the sense of Hadamard

may be placed in a probabilistic setting in order to eliminate the ill-posedness by reformulating the inverse problem as a well-posed problem of *Bayesian inference* [170, 86, 167] in a larger space of probability distributions. While the classical regularisation produces solely single estimates of the desired quantities, the probabilistic approach yields a collection of values or a distribution.

Real-world problems are characterised by a high level of uncertainty, the improper modelling of which results in discrepancies between the model predictions and empirical results deriving from the real processes. Identifying and properly accounting for the sources of uncertainty can often be a challenging task, considering that one does not always have a complete knowledge about the relevant physical mechanisms and one cannot easily indicate the most influential parameters. Moreover, the choice of the model parameters characterising the underlying physical system is generally not unique. Another source of discrepancies in the results is the significant influence of both modelling error (e.g. due to modelling assumptions and approximations) and the inherent measurement noise.

In general, uncertainties in engineering systems are typically categorised either as *aleatoric* or *epistemic* [35]. The former is referred to as an irreducible, inherent randomness of a phenomenon, whereas the latter is perceived as uncertainty due to lack of knowledge and can be reduced by gathering additional information. As authors report in [35], in many applications there is no strict distinction between these types of uncertainty, it mostly depends on the context and peculiarities of the application. Moreover, the nature of uncertainties is a reflection of the subjective interpretation of the analyst. In this view, some material property can be considered both aleatoric and epistemic, depending on whether a structure is already existing or yet to be constructed [35]. In the former case, the uncertainty in the target material properties can be reduced by gathering observations of the structural behaviour.

In design and modelling of civil engineering systems, the main sources of uncertainty [162, 169, 35] are summarised below:

- *Model form uncertainty.* The uncertainty attributed to the fact that mathematical models are merely a reflection of reality, an approximation of the underlying physical problem. Often, the relations between inputs and outputs are not straightforward and some variables are not

considered due to simplifications or lack of information about the model dependencies. Moreover, essentially nonlinear behaviour of the materials is usually approximated with different types of constitutive laws (e.g. plasticity, damage) or in some cases with a linear form. The extent to which this impacts the predictions may be modelled through the modelling error.

- *Parametric uncertainty.* This uncertainty pertains to the lack of knowledge about the actual values of the model parameters, such as material properties, load or initial and boundary conditions. It is typically considered as epistemic uncertainty, as it can be significantly reduced with considerable quantity and quality of observational data.

- *Experimental uncertainty.* This type of uncertainty is reflected in limited or incomplete experimental data and limitation in the accuracy of the measuring devices. Often, carrying out measurements on actual structures is not feasible, particularly in the case of massive structures (e.g. bridges, dams). Instead, experimental validation is performed on smaller-scale surrogate models or structural members which are easier to set up in a testing facility. For a number of applications, where experimental validation is ruled out, we rely solely on numerical models, the quality of which is also in a great manner affected by the lack of experimental data. The limited accuracy of the measuring devices is another aspect of the experimental uncertainty which is manifested in terms of a measurement error, usually taken as mean-free Gaussian noise.

In this contribution, both the epistemic uncertainty arising from the lack of knowledge about the true values of mechanical properties of plain and reinforced concrete and the aleatoric uncertainty, the effects of which are noticeable through different outcomes of repeated measurements are explored. The aim is to combine both our engineering knowledge and information from data to produce more accurate estimates of the system's state and parameters and thereby achieve more reliable predictions of the system's future states. The target parameters often cannot be observed directly, but only through some system response quantities polluted with measurement noise. The uncertain model parameters are probabilistically described through random variables, $q : \Omega \to \mathcal{Q}$, and their *a posteriori* distributions are inferred from the observations generated by the observation operator $Y_Q : \mathcal{Q} \to \mathcal{Y}$. As already stated above, the observation operator Y_Q is usually not invertible, which in deterministic setting leads to ill-posedness of the parameter estimation problem.

This chapter tackles the probabilistic approach to modelling uncertainties in mechanical systems and the methodology concerning the parameter estimation in a Bayesian setting. It starts by placing the chosen method for solving the stochastic inverse problem of parameter estimation into a wider context of available approaches. Afterwards, the basic notion of probability theory is introduced and the stochastic model is set up in an abstract manner. This is followed by Sections 2.3 and 2.4, which deal with the reduction of dimensionality and computational burden. Lastly, inverse problems are described from the Bayesian viewpoint, focusing on the chosen approach for obtaining the posterior estimates based on approximation of the *conditional expectation* (CE).

2.1 An overview of numerical approaches for solving stochastic inverse problems

The procedure of computing the posterior distribution may be approached from two different perspectives, by computing either its estimates or its samples. In most practical applications, knowledge about the full posterior *probability density function* (PDF) is not required and one needs only some specific estimates (e.g. the mean or expected value).

One of the most frequently used single-point estimation methods is the *maximum likelihood estimator* (MLE) [86, 90], where the unknown parameters of interest are estimated with the help of observational data by maximising the likelihood function, more precisely by maximising the conditional probability of observing the data. This method yields reliable estimates when the sample size is fairly large and should be avoided otherwise. For the case of uniform prior, the MLE is a special case of another commonly used estimator, the *maximum a posteriori estimator* (MAP) [86, 12]. Unlike the MLE which belongs to the family of frequentist methods, MAP is essentially a Bayesian method. Namely, the latter maximises the posterior density, thus the likelihood is weighted by the prior. Another commonly used Bayesian estimator is the *minimum mean square estimator* (MMSE) [90, 86], where the loss function is of a quadratic type and the MMSE is thus given in terms of the posterior mean.

One of the most widely used sampling-based approaches for computing the posterior is the class of *Markov chain Monte Carlo* methods (MCMC) [62,

172, 58], including the well known *Metropolis-Hastings algorithm* (MH) [115, 114, 62, 27] and the *Gibbs sampler* [51]. The method is based on constructing a memory-less Markov chain, the equilibrium distribution of which is the target posterior distribution sought through the random walk. As it is a pure sampling procedure, it is characterised by a slow convergence and a burn-in period. Moreover, it can be very demanding for the large-scale problems, hence it is often used together with a proxy model instead of the high-fidelity forward solver.

In various applications, the observational data is time-dependent, with observations at different time instances providing information about the state of the system. For such nonstationary inverse problems, a suitable approach for solving a stochastic inverse problem is via Bayesian *filtering* methods, based on the approximation of the conditional expectation. Among these, the most noted and commonly used is the *Kálmán filter* (KF) [87, 6, 28], which approximates the CE with linear (affine) maps. In the classical sense, the Kálmán filter assumes Gaussian random variables, a linear model operator and a linear measurement operator. It is formulated in terms of linear transformations of the mean and covariance, which under the above conditions preserve the Gaussianity of the posterior. It should be noted that this statement holds only for linear problems [169], whereas in other cases it leads to approximations and underestimation of the covariance. The Kálmán filter can also be used for stationary Bayesian inverse problems, in which case it is referred to as the *Kálmán smoother*. An extension to the nonlinear problems is called the *extended Kálmán filter* (EKF) [81], which restates the linearity of the model and measurement operators by means of a first order truncation of a Taylor series expansion.

A sampling interpretation of the linear Kálmán filtering procedure is the *ensemble Kálmán filter* (EnKF) [43, 44, 75], where all the quantities are expressed in terms of Monte Carlo ensembles. In real-world applications, though, the models are sometimes not given in a closed form, they may not be differentiable or the linearisation of the model and measurement operator is not feasible. In such a case, it is convenient to use the *particle filters* (PF) [57, 103, 38, 54, 25], which successfully cope with the nonlinearities of the system and sequentially estimate the posteriror densities in terms of ensembles of Monte Carlo samples.

A generalisation of the classical Kálmán filter to nonlinear problems and non-Gaussian random variables is the so-called *Gauss-Markov-Kálmán filter* (GMKF) [111, 145, 108], which can further be accelerated by describing all

random variables in terms of functional approximations [144, 109, 110, 136, 137, 42]. Alternatively, the CE can be approximated by the *square-root PCE-based GMKF* (SRPCU) [138, 135]. The square-root approach shows great efficiency in terms of memory and implementation requirements, as it does not extend the polynomial basis upon gathering additional observations in a sequential update setting.

Recently, data-driven approaches are increasingly gaining popularity in the field of parameter estimation. *Machine learning* tools, such as *Artificial Neural Networks* (ANN) [56], can be employed to estimate the parameters of the underlying physical model by learning the mapping from data to parameters. That is done by training the neural network on a large number of model realisations resulting from different sets of parameter values. The trained neural network can then be applied to the actual observations to yield the parameter estimates, alongside with the information regarding the statistical accuracy [185]. Moreover, the parameter estimation using ANN can be formulated from a viewpoint of a recursive Bayesian inference problem [19], where Bayes rule is applied for each online learning step to approximate the posterior of weights of the neural network (e.g. see [132, 188, 133, 128]). Nevertheless, these methods require a large training dataset, which may be prohibitive for large-scale problems. Alternatively, the parameter identification problem may be formulated in terms of physics-informed neural networks (PINN) [7], which includes both prior knowledge in terms of physical laws behind the observations and noisy observational data. The respective method is applicable to high dimensional problems.

2.2 Abstract model problem

The true value of the model parameters, collected in a random vector $\boldsymbol{q}$, is assumed to be unknown. The lack of knowledge about the model inputs is modelled by *random variables* $q_f : \Omega \to \mathcal{Q}$, in which the index f denotes the forecast. Random vector $\boldsymbol{q}$ lives in the *probability space* $(\Omega, \mathfrak{F}, \mathbb{P})$, where Ω stands for the *sample space* of all possible outcomes, the set of events $\mathfrak{F}$ is a *σ-algebra* of subsets of Ω and $\mathbb{P} : \mathfrak{F} \to [0, 1]$ is a *probability measure*. Both the parameter space $\mathcal{Q}$ and the measurement space $\mathcal{Y}$ are considered to be finite dimensional vector spaces equipped with an inner product $\langle q_1, q_2 \rangle_{\mathcal{Q}}$ and induced norm $||q||_{\mathcal{Q}} = \sqrt{q \cdot q}$.

A mathematical model of the studied physical system can symbolically be written as

$$\mathscr{A}(\boldsymbol{u}, \boldsymbol{q}) = f(\boldsymbol{q}), \tag{2.1}$$

where $\boldsymbol{u}$ is the state of the system assumed to belong to a vector space $\mathcal{U}$, $\boldsymbol{q} \in \mathcal{Q}$ are the uncertain model parameters and $f(\boldsymbol{q}) \in \mathcal{U}^*$ is the source term (e.g. loading, initial conditions) placed in the dual space $\mathcal{U}^*$, which is the space of all linear forms over $\mathcal{U}$. The term $\mathscr{A}$ represents a nonlinear *forward model* describing the relationship between the model parameters and the external influence, such that $\mathscr{A} : \mathcal{U} \to \mathcal{U}^*$. It is assumed that Eq. (2.1) describes a well-posed problem such that there exists a unique solution $\boldsymbol{u} \in \mathcal{U}$, which is a function of the model parameters $\boldsymbol{q}$ and the external influence $f(\boldsymbol{q})$ and satisfies

$$\boldsymbol{u} = S(\boldsymbol{q}, f(\boldsymbol{q})), \tag{2.2}$$

where S is a *solution operator* which relates $\boldsymbol{u}$ to $\boldsymbol{q}$ in an explicit manner.

It is assumed that neither the state nor the model parameters are directly observable and one can only observe a function of them. Therefore, an *observation operator* Y_Q relating the uncertain model parameters $\boldsymbol{q}$ to a set of predicted observations $\boldsymbol{y} \in \mathcal{Y}$ is defined, i.e. $Y_Q : \mathcal{Q} \to \mathcal{Y}$, where $\mathcal{Y}$ is a finite dimensional vector space $\mathbb{R}^m$ collecting the information from m measurements. In reality, one cannot observe directly $\boldsymbol{y}$, as it is characterised by some *measurement noise* $\boldsymbol{\varepsilon}$. The prediction of the observations $\boldsymbol{y}_f \in \mathcal{Y}$ is defined as a sample of the observation operator and the noisy observations $\boldsymbol{z}_f$ are then expressed as

$$\begin{aligned} \boldsymbol{z}_f(\omega, \eta) &= \boldsymbol{y}_f(\omega) + \boldsymbol{\varepsilon}(\eta) \\ &= Y_Q(\boldsymbol{q}(\omega), S(\boldsymbol{q}(\omega), f(\boldsymbol{q}(\omega)))) + \boldsymbol{\varepsilon}(\eta), \end{aligned} \tag{2.3}$$

in which $\boldsymbol{\varepsilon}(\eta) \sim \mathcal{N}(0, C_{\boldsymbol{\varepsilon}})$ is a realisation of the measurement noise distributed according to zero-mean Gaussian distribution with covariance $C_{\boldsymbol{\varepsilon}}$. The elements in $\boldsymbol{\varepsilon}$ are considered to be independent of the uncertainty in the model parameters $\boldsymbol{q}$.

2.3 Polynomial surrogate model

Numerical models describing complex behaviour of physical systems, such as the ones introduced in Sections 3.2 and 3.3 modelling cracking and bond-slip

in reinforced and plain concrete, respectively, often come with high computational burden. Hence, for the purpose of calculating the forward statistics, performing the sensitivity analysis and solving the stochastic inverse problem, the high-fidelity numerical models are replaced by computationally efficient lower-fidelity *surrogate* or *proxy* models.

Surrogate models are an engineering method utilised in order to facilitate evaluation of the complex systems. They mimic the behaviour of the underlying high-fidelity simulation model, retaining its accuracy and the essential physics, while decreasing the computational burden. The internal characteristics of the model, as well as the inner working of the simulation code does not have to be precised, solely the relation between the input and output is relevant.

A commonly used surrogate model is the polynomial surrogate model. It is based on the notion that any random variable $q(\omega) \in L_2(\Omega)$ may be represented as a linear combination of multivariate polynomials $\Psi_\alpha(\theta(\omega))$ in terms of uncorrelated and independent variables $\theta(\omega)$

$$\forall \alpha \in \mathcal{J}_M : \; q(\theta(\omega)) \approx \sum_{\alpha \in \mathcal{J}_M} q^{(\alpha)} \Psi_\alpha(\theta(\omega)), \tag{2.4}$$

where $q^{(\alpha)}$ are the polynomial coefficients and α denotes a multi-index from a finite multi-index set $\mathcal{J}_M$. The required number M of the polynomials after which the expression in Eq. (2.4) is truncated may be computed from

$$M + 1 = \frac{(N_p + N_\theta)!}{N_p! N_\theta!}. \tag{2.5}$$

The term N_p in Eq. (2.5) denotes the maximal degree of polynomials and N_θ is the number of random variables.

The functional approximation in Eq. (2.4) is known as the *Wiener polynomial chaos expansion* (PCE) [186, 191]. It is based on the orthogonality relation

$$\mathbb{E}[\Psi_i \Psi_j] = \int_\Omega \Psi_i(\theta) \Psi_j(\theta) \pi(\theta) \, d\theta \propto \delta_{ij}, \tag{2.6}$$

stating that the polynomials are orthogonal with respect to the joint probability density function of the approximated random variables. Polynomials satisfying the orthogonality relation are different for different probability densities. For instance, for random variables which follow the Gaussian distribution, the surrogate model is built by using the *Hermite polynomials*. The

term δ_{ij} in (2.6) denotes the Kronecker delta function with the following properties

$$\delta_{ij} = \begin{cases} 0; & i \neq j \\ 1; & i = j. \end{cases} \tag{2.7}$$

Polynomial coefficients $q^{(\alpha)}$ may be determined by stochastic collocation, projection, regression, stochastic Galerkin etc. In this work, coefficients are evaluated by regression, i.e. by minimising the sum of squares of errors.

2.4 Sensitivity analysis

In practical applications, number of the model parameters may be quite large. Nevertheless, not all of them are equally significant for the analysis. More precisely, some random model parameters may not significantly contribute to the variability of the output and hence can be fixed to nominal values. In this regard, the dimensionality of the stochastic problem is considerably reduced and the high-fidelity finite element (FE) solver is replaced by a proxy model, which uses a lower-dimensional set of input variables [162]. This concept is formalised in terms of *global sensitivity analysis* (SA) [163], which quantifies to which extent the output depends upon variations of particular uncertain model parameters and their combinations.

Sensitivity analysis is closely related to the *analysis of variance* (ANOVA) [65], which illustrates a variance-based decomposition of a function. Recalling the previously introduced notation, let $\boldsymbol{q}_f(\boldsymbol{\theta})$ be the N_θ-dimensional vector of uncertain inputs expressed in terms of independent RVs $\boldsymbol{\theta}$ and $\boldsymbol{y}_f(\boldsymbol{q}_f(\boldsymbol{\theta})) \in \mathcal{Y}$ the model output given by $\boldsymbol{y}_f(\boldsymbol{q}_f(\boldsymbol{\theta})) = Y_Q(q_{f,1}(\theta_1), ..., q_{f,N_\theta}(\theta_{N_\theta}))$. For the sake of simplicity, variables $\boldsymbol{q}_f(\boldsymbol{\theta})$, $\boldsymbol{y}_f(\boldsymbol{q}_f(\boldsymbol{\theta}))$, Y_Q and N_θ are abbreviated to $\boldsymbol{q}(\boldsymbol{\theta})$, $\boldsymbol{y}(\boldsymbol{\theta})$, Y and N, respectively. Supposing that $Y(\boldsymbol{\theta})$ is a general square-integrable function defined on the unit hypercube $[0,1]^N$, its elementary functional decomposition according to [65] is defined as

$$Y(\boldsymbol{\theta}) = Y_0 + \sum_{i=1}^{N} N_i(\theta_i) + \sum_{i<j}^{N} Y_{i,j}(\theta_i, \theta_j) + ... + Y_{1,2,...,N}(\boldsymbol{\theta}). \tag{2.8}$$

According to [163], the term Y_0 in Eq. (2.8) is constant and the individual terms can be calculated uniquely under the following condition

$$\int_0^1 Y_{i_1,...,i_s}(\theta_{i_1},...,\theta_{i_s})d\theta_{i_k} = 0, \quad 1 \leq k \leq s, \quad i_1,...,i_s \subseteq 1,...,N, \tag{2.9}$$

stating that all the terms in the functional decomposition in Eq. (2.9) are orthogonal and hence they can be expressed as conditional expected values [65]. Due to orthogonality, the output variance can be decomposed as

$$Var(\boldsymbol{y}) = \sum_{i=1}^{N} D_i(\boldsymbol{y}) + \sum_{i<j}^{N} D_{i,j}(\boldsymbol{y}) + ... + D_{1,2,...,N}(\boldsymbol{y}), \tag{2.10}$$

where $Var(\boldsymbol{y})$ is the total variance and the *partial variances* are given by

$$\begin{aligned} D_i(\boldsymbol{y}) &= Var[\mathbb{E}(\boldsymbol{y}|\theta_i)], \\ D_{i,j}(\boldsymbol{y}) &= Var[\mathbb{E}(\boldsymbol{y}|\theta_i,\theta_j)] - D_i(\boldsymbol{y}) - D_j(\boldsymbol{y}). \end{aligned} \tag{2.11}$$

Finally, one can define the *Sobol indices* [163], which quantify the contribution $D_i(\boldsymbol{y})$ of a particular input parameter θ_i in the output variance $Var(\boldsymbol{y})$ as

$$\begin{aligned} S_i &= \frac{D_i(\boldsymbol{y})}{Var(\boldsymbol{y})}, \\ S_{i,j} &= \frac{D_{i,j}(\boldsymbol{y})}{Var(\boldsymbol{y})}, \end{aligned} \tag{2.12}$$

where the terms S_i denote the first-order Sobol sensitivity indices and $S_{i,j}$ refer to the second-order Sobol sensitivity indices representing the influence of interaction terms. Higher order Sobol indices are usually not examined in practical problems. Large values of Sobol indices imply the parameters which strongly influence the response variance.

The total impact of a particular parameter on the response can be quantified using the total sensitivity indices [66]

$$S_{T_i} = S_i \sum_{i<j} S_{i,j} + \sum_{j\neq i, k\neq i, j<k} S_{i,j,k} + ... = \sum_{l \in \sharp i} S_l, \tag{2.13}$$

where $\sharp i$ are the subsets of $1,...,N$, including i.

2.4.1 Calculation of Sobol indices from PCE coefficients

Recalling the polynomial chaos expansion, one can derive the expressions for the Sobol indices directly from the PCE coefficients. The orthogonality property of the polynomial chaos basis functions stated in Eq. (2.6) leads to expressions for the expected value and partial variances defined as

$$\mu_0 = \mathbb{E}(\boldsymbol{y}) = \boldsymbol{y}^{(0)}, \tag{2.14}$$

$$D_i = Var(\boldsymbol{y}) = \sum_{\substack{\alpha \in \mathbb{N}^N \\ \alpha \neq 0}} (\boldsymbol{y}^{(\alpha)})^2. \tag{2.15}$$

Finally, the computation of the first-order Sobol indices from the PCE reads

$$S_i = \frac{\sum_{\alpha \in \mathcal{A}_i} (\boldsymbol{y}^{(\alpha)})^2}{\sum_{\alpha \neq 0} (\boldsymbol{y}^{(\alpha)})^2}, \tag{2.16}$$

where $\mathcal{A}_i = \{\alpha \in \mathcal{A} | \alpha_i > 0, \alpha_{j \neq i} = 0\}$.

Similarly, the total sensitivity indices can be obtained from

$$S_{T_i} = \frac{\sum_{\alpha \in \mathcal{A}_{T_i}} (\boldsymbol{y}^{(\alpha)})^2}{\sum_{\alpha \neq 0} (\boldsymbol{y}^{(\alpha)})^2}, \tag{2.17}$$

where $\mathcal{A}_{T_i} = \{\alpha \in \mathcal{A} | \alpha_i > 0\}$. Higher-order indices can be obtained in a similar manner.

2.5 Bayesian approach to parameter estimation

Bayesian inference [170, 167, 42] is a probabilistic description of inverse problems based on Bayes' theorem [99]. The lack of knowledge about the true values of the model parameters is modelled by random variables collected in a random vector $\boldsymbol{q}$ and described through *prior* probability density functions $\pi_0(\boldsymbol{q})$. In a Bayesian setting, the latter represents the additional information needed to solve the inverse problem in a unique sense. Knowledge about the model parameters may be updated by conditioning on the observations, hence changing the probabilistic description of unknown model parameters to the *posterior* probability density functions by means of *Bayes' rule* [99].

Under the assumption that uncertain parameters $\boldsymbol{q}$ and observations $\hat{\boldsymbol{z}}$ have a joint probability density function $\pi(\boldsymbol{q}, \hat{\boldsymbol{z}})$, Bayes' rule may be used in its density form as

$$\pi(\boldsymbol{q}|\hat{\boldsymbol{z}}) = \frac{\pi(\hat{\boldsymbol{z}}|\boldsymbol{q})\pi_0(\boldsymbol{q})}{P(\hat{\boldsymbol{z}})} \propto L(\boldsymbol{q})\pi_0(\boldsymbol{q}), \tag{2.18}$$

where $\pi(\boldsymbol{q}|\hat{\boldsymbol{z}})$ and $\pi_0(\boldsymbol{q})$ denote the posterior and prior probability density functions, respectively, where $\hat{\boldsymbol{z}}$ are the noisy (actual) measurements defined as $\hat{\boldsymbol{z}} := Y_Q(\boldsymbol{q}_{true}) + \hat{\boldsymbol{\varepsilon}}$. The term $L(\boldsymbol{q}) = \pi(\hat{\boldsymbol{z}}|\boldsymbol{q})$ refers to the *likelihood* function which incorporates the information from the data into the updating of the probability description of the uncertain parameters. The term in the denominator, $P(\hat{\boldsymbol{z}})$, specifies the normalising constant, also called *evidence*, such that the joint posterior probability density function integrates to unity, $P(\hat{\boldsymbol{z}}) = \int_\Omega \pi(\hat{\boldsymbol{z}}|\boldsymbol{q})\pi_0(\boldsymbol{q})d\boldsymbol{q}$. Bayes' rule in Eq. (2.18) may be extended in order to accommodate the nonstationary problems. In that case, the posterior density is sequentially updated for a set of m independent observations as

$$\pi(\boldsymbol{q}|\hat{z}_1, ..., \hat{z}_m) \propto L(\boldsymbol{q}|\hat{z}_m)\pi_0(\boldsymbol{q}|\hat{z}_1, ..., \hat{z}_{m-1}). \tag{2.19}$$

As the posterior probability density functions usually cannot be computed analytically in practice, one has to employ some computational algorithm. Sampling-based approaches such as the Markov-chain Monte Carlo method [62, 172] are typically characterised by a slow convergence. Moreover, practical applications often do not require knowledge about the full posterior density, but only its estimates, among the most significant ones is the expected value. Hence, instead of computing the conditional posterior density $\pi(\boldsymbol{q}|\hat{\boldsymbol{z}})$ one can evaluate the conditional expectation [109], which is quantified as

$$\mathbb{E}(\boldsymbol{q}|\mathfrak{B}) := \int_{\mathcal{Q}} \boldsymbol{q}\pi(\boldsymbol{q}|\hat{\boldsymbol{z}})d\boldsymbol{q}, \tag{2.20}$$

where $\mathfrak{B} := \sigma(Y_Q)$ is the *Borel* sub-σ-algebra, $\mathfrak{B} \subset \mathfrak{F}$, generated by the measurement operator Y_Q. The expression in Eq. (2.20) holds under the assumption that random variables contained in the random vector $\boldsymbol{q}$ have finite variance, which implies that they belong to the *Hilbert space* $\mathcal{S} := L_2(\Omega, \mathfrak{F}, \mathbb{P})$. In that case, conditional expectation may be viewed as an orthogonal projection $P_\mathfrak{B} : \mathcal{S} \to \mathcal{S}_\mathfrak{B}$ of $\boldsymbol{q}$ onto the closed subspace $\mathcal{S}_\mathfrak{B} := L_2(\Omega, \mathfrak{B}, \mathbb{P})$ of all random variables consistent with the observations. Hence, the conditional expectation minimises the difference between the random vector $\boldsymbol{q}$ and its projection, which leads to a minimisation problem of finding an optimal $\tilde{\boldsymbol{q}}$ for which the mean square error is minimised as

$$\tilde{\boldsymbol{q}}_{MSE}(\hat{\boldsymbol{z}}) = \mathbb{E}(\boldsymbol{q}|\hat{\boldsymbol{z}}) = \arg\min_{\tilde{\boldsymbol{q}}} \mathbb{E}\left((\boldsymbol{q} - \tilde{\boldsymbol{q}})^T (\boldsymbol{q} - \tilde{\boldsymbol{q}}) \,|\hat{\boldsymbol{z}}\right). \tag{2.21}$$

From Eq. (2.21) follows that the vector of uncertain parameters $\boldsymbol{q}$ can be orthogonally decomposed into the projected $\boldsymbol{q}_p := P_{\mathfrak{B}}\boldsymbol{q}$ and the orthogonal $\boldsymbol{q}_o = (I - P_{\mathfrak{B}})\boldsymbol{q}$ component. Any new observation alters the projected part, while the orthogonal part acts as the residual of the prior $\boldsymbol{q}_f$. Thus, the decomposition reads

$$\boldsymbol{q}_a = \mathbb{E}\left(\boldsymbol{q}_f|\hat{\boldsymbol{z}}\right) + \left(\boldsymbol{q}_f - \mathbb{E}\left(\boldsymbol{q}_f|\boldsymbol{z}_f\right)\right), \tag{2.22}$$

in which the first term represents the information coming from data and the latter one the information coming from prior. The index a in $\boldsymbol{q}_a$ indicates the assimilated or a posteriori random variable. According to the *Doob-Dynkin lemma*, anything that is learnt from a measurement is a function of the measurement. Hence, the CE can be viewed as $\mathbb{E}(\boldsymbol{q}_f|\boldsymbol{z}_f) := \varphi(\boldsymbol{z}_f)$ and Eq. (2.22) after rearranging the terms further modifies to

$$\boldsymbol{q}_a = \boldsymbol{q}_f + \varphi\left(\hat{\boldsymbol{z}}\right) - \varphi\left(\boldsymbol{z}_f\right), \tag{2.23}$$

which is a generalised Kálmán filter equation. The term φ in Eq. (2.23) stands for a measurable map describing the mapping from an observation to the parameter set, i.e. $\varphi : \mathcal{Y} \to \mathcal{Q}$, and can be approximated either by linear of higher order maps. From Eq. (2.23) and by assuming only linear (affine) maps, one can build the Gauss-Markov-Kálmán filter [111, 144], described in the following Section 2.5.1.

Although the Kálmán filter is mainly intended for strictly linear problems described in terms of Gaussian random variables, it can be extended to nonlinear operators, such as the one employed in the work herein, and non-Gaussian random variables. In that case, the estimation of conditional expectation is not exact, but merely an approximation containing an additional approximation error.

2.5.1 Gauss-Markov-Kálmán filter update via functional approximations

Posterior of the target parameters is computed from Eq. (2.23) by introducing the approximation of the conditional expectation in terms of linear maps as

$$\mathbb{E}(\boldsymbol{q}_f|\boldsymbol{z}_f) \approx \varphi(\boldsymbol{z}_f) := \boldsymbol{K}\boldsymbol{z}_f + \boldsymbol{b}, \tag{2.24}$$

with coefficients $\boldsymbol{K}$ and $\boldsymbol{b}$ obtained from the minimisation of the orthogonal component $\boldsymbol{q}_o$ in the mean square error (MSE) sense as

$$\begin{aligned} &\arg\min_{\boldsymbol{K},\boldsymbol{b}} \mathbb{E}((||\boldsymbol{q}_f - \mathbb{E}(\boldsymbol{q}_f|\boldsymbol{z}_f)||_2^2) = \\ &\arg\min_{\boldsymbol{K},\boldsymbol{b}} \mathbb{E}((||\boldsymbol{q}_f - \boldsymbol{K}\boldsymbol{z}_f - \boldsymbol{b})||_2^2). \end{aligned} \tag{2.25}$$

This results in a linear Gauss-Markov-Kálmán filter equation taking the form of

$$\boldsymbol{q}_a(\omega,\eta) = \boldsymbol{q}_f(\omega) + \boldsymbol{K}(\hat{\boldsymbol{z}} - \boldsymbol{z}_f(\omega,\eta)), \tag{2.26}$$

where $(\hat{\boldsymbol{z}} - \boldsymbol{z}_f(\omega,\eta))$ is the *innovation* and $\boldsymbol{K}$ is the *Kálmán gain* defined as

$$\boldsymbol{K} = \boldsymbol{C}_{\boldsymbol{q}_f,\boldsymbol{y}_f}(\boldsymbol{C}_{\boldsymbol{y}_f} + \boldsymbol{C}_{\boldsymbol{\varepsilon}})^{\dagger}. \tag{2.27}$$

In case of singularity, $\dagger$ in Eq. (2.27) denotes the pseudo-inverse and $\boldsymbol{C}_{\boldsymbol{q}_f,\boldsymbol{y}_f} := \mathbb{E}\left(\tilde{\boldsymbol{q}}_f \otimes \tilde{\boldsymbol{y}}_f\right)$, $\boldsymbol{C}_{\boldsymbol{y}_f} := \mathbb{E}\left(\tilde{\boldsymbol{y}}_f \otimes \tilde{\boldsymbol{y}}_f\right)$, $\boldsymbol{C}_{\boldsymbol{\varepsilon}} := \mathbb{E}\left(\boldsymbol{\varepsilon} \otimes \boldsymbol{\varepsilon}\right)$ are the corresponding covariances, in which $\tilde{\boldsymbol{q}}_f$ and $\tilde{\boldsymbol{y}}_f$ refer to the fluctuating part of random variables $\boldsymbol{q}$ and $\boldsymbol{y}_f$ obtained by subtracting the mean, i.e. $\tilde{\boldsymbol{q}}_f := \boldsymbol{q}_f - \bar{\boldsymbol{q}}_f$. For a more thorough derivation of the GMKF see, e.g. [111, 109, 108, 144].

Performance of the GMKF can be further accelerated by representing the inputs in terms of functional approximations based on the polynomial chaos expansion introduced in Section 2.3. By taking into account Eq. (2.4), the uncertain model parameters may be expanded as

$$\forall \alpha \in \mathcal{J}_M : \ \boldsymbol{q}_f\left(\boldsymbol{\theta}\left(\omega\right)\right) \approx \sum_{\alpha \in \mathcal{J}_M} \boldsymbol{q}^{(\alpha)} \Psi_\alpha\left(\boldsymbol{\theta}\left(\omega\right)\right), \tag{2.28}$$

where $\boldsymbol{q}^{(\alpha)}$ are the polynomial coefficients and α denotes a multi-index from a finite multi-index set $\mathcal{J}_M$.

The remaining terms in the filtering Eq. (2.26) can be written in the same manner as in Eq. (2.28). Hence, the approximation of the observable $\boldsymbol{y}_f$ reads

$$\forall \alpha \in \mathcal{J}_M : \ \boldsymbol{y}_f\left(\boldsymbol{\theta}\left(\omega\right)\right) \approx \sum_{\alpha \in \mathcal{J}_M} \boldsymbol{y}^{(\alpha)} \Psi_\alpha\left(\boldsymbol{\theta}\left(\omega\right)\right), \tag{2.29}$$

while the functional approximation of the measurement error is defined as

$$\forall \beta \in \mathcal{J}_E : \ \boldsymbol{\varepsilon}\left(\boldsymbol{\xi}\left(\eta\right)\right) \approx \sum_{\beta \in \mathcal{J}_E} \boldsymbol{e}^{(\beta)} \Psi_\beta\left(\boldsymbol{\xi}\left(\eta\right)\right). \tag{2.30}$$

The difference in the PCE basis in Eq. (2.28) and Eq. (2.30) implies the independence of the measurement error $\boldsymbol{\varepsilon}$ from the uncertainty in the model parameters $\boldsymbol{q}$.

Measurements $\hat{\boldsymbol{z}}$ may also be expressed in terms of PCE, but being deterministic quantities their PCE contains only the first term corresponding to the zero-th polynomial $\Psi_0(\boldsymbol{\xi}(\eta)) = 1$, such that

$$\forall \beta \in \mathcal{J}_E : \ \hat{\boldsymbol{z}} \approx \sum_{\beta=0} \boldsymbol{z}^{(0)} \Psi_\beta(\boldsymbol{\xi}(\eta)). \tag{2.31}$$

By taking into account Eqs. (2.28)-(2.30), the GMKF formula given in Eq. (2.26) can be expressed in terms of PCE representation as

$$\begin{aligned} \forall \gamma \in \mathcal{J}_G : \sum_{\gamma \in \mathcal{J}_G} \boldsymbol{q}_a^{(\gamma)} \Psi_\gamma(\boldsymbol{\theta}, \boldsymbol{\xi}) = \sum_{\gamma \in \mathcal{J}_G} \boldsymbol{q}_f^{(\gamma)} \Psi_\gamma(\boldsymbol{\theta}, \boldsymbol{\xi}) + \\ + \boldsymbol{K} \left(\sum_{\gamma=0} \boldsymbol{z}^{(0)} \Psi_\gamma(\boldsymbol{\theta}, \boldsymbol{\xi}) - \left(\sum_{\gamma \in \mathcal{J}_G} \boldsymbol{y}^{(\gamma)} \Psi_\gamma(\boldsymbol{\theta}, \boldsymbol{\xi}) + \sum_{\gamma \in \mathcal{J}_G} \boldsymbol{e}^{(\gamma)} \Psi_\gamma(\boldsymbol{\theta}, \boldsymbol{\xi}) \right) \right), \end{aligned} \tag{2.32}$$

in which the PCE approximations are written in the extended basis $\Psi_\gamma(\boldsymbol{\theta}, \boldsymbol{\xi})$, containing all the basis functions used for the expansion of $\boldsymbol{q}$, $\boldsymbol{z}_f$, $\hat{\boldsymbol{z}}$ and $\boldsymbol{\varepsilon}$.

Exploiting the linearity property, the expansion in Eq. (2.32) may be rewritten in such manner that the assimilation is carried out directly for the PCE coefficients as

$$\forall \gamma \in \mathcal{J}_G : \boldsymbol{q}_a^{(\gamma)} = \boldsymbol{q}_f^{(\gamma)} + \boldsymbol{K} \left(\hat{\boldsymbol{z}} - \left(\boldsymbol{y}^{(\gamma)} + \boldsymbol{e}^{(\gamma)} \right) \right), \tag{2.33}$$

The greatest advantage of the PCE based GMKF lies in the fact that Eq. (2.23) becomes purely algebraic and the computation of the posterior quantities straightforward.

2.5.2 The generalised ensemble Kálmán filter

Although the PCE formulation of the KF greatly reduces the computational burden, the drawback of such representation is that in the case of high dimensionality of the stochastic problem, it requires a large number of evaluations of the high-fidelity model to be able to accurately compute the polynomial

coefficients. In the problem considered herein, heterogeneous nature of concrete at finer scales results in a large number of input variables and considering the complexity of the numerical model, constructing a PCE approximation becomes prohibitive. As an alternative, a sampling-based generalised ensemble Kálmán filter (EnGKF) is employed to compute the posterior estimates.

The ensemble Kálmán filter is a sampling interpretation of the classical Kálmán filter, where all random variables are expressed in terms of Monte Carlo ensembles. Filtering equation given in Eq. (2.23) can be rewritten in matrix notation to accommodate the ensembles of random variables as

$$\boldsymbol{Q}_a = \boldsymbol{Q}_f + \boldsymbol{K}\left(\hat{\boldsymbol{Z}} - (\boldsymbol{Y}_f + \boldsymbol{E})\right), \tag{2.34}$$

in which $\boldsymbol{Q}_f := [\boldsymbol{q}_f(\omega_1), ..., \boldsymbol{q}_f(\omega_N)]$, $\boldsymbol{Y}_f := [\boldsymbol{y}_f(\omega_1), ..., \boldsymbol{y}_f(\omega_N)]$ and $\boldsymbol{E} := [\boldsymbol{\varepsilon}(\eta_1), ..., \boldsymbol{\varepsilon}(\eta_N)]$ denote the ensembles of prior model input parameters, predicted observations and measurement error, respectively, composed of N independent random samples. The Kálmán gain is denoted by $\boldsymbol{K}$, while the covariances are approximated by the Monte Carlo samples as

$$\boldsymbol{C}_{\boldsymbol{q}_f,\boldsymbol{y}_f} \approx \frac{1}{N-1}\sum_{i=1}^{N}\left(\boldsymbol{q}_f(\omega_i) - \bar{\boldsymbol{q}}_f\right)\left(\boldsymbol{y}_f(\omega_i) - \bar{\boldsymbol{y}}_f\right)^T, \tag{2.35}$$

$$\boldsymbol{C}_{\boldsymbol{y}_f} \approx \frac{1}{N-1}\sum_{i=1}^{N}\left(\boldsymbol{y}_f(\omega_i) - \bar{\boldsymbol{y}}_f\right)\left(\boldsymbol{y}_f(\omega_i) - \bar{\boldsymbol{y}}_f\right)^T, \tag{2.36}$$

$$\boldsymbol{C}_{\boldsymbol{\varepsilon}} \approx \frac{1}{N-1}\sum_{i=1}^{N}\left(\boldsymbol{\varepsilon}(\eta_i) - \bar{\varepsilon}\right)\left(\boldsymbol{\varepsilon}(\eta_i) - \bar{\varepsilon}\right)^T, \tag{2.37}$$

where the bar over a variable denotes its sample mean, i.e. $\bar{\boldsymbol{q}}_f = \frac{1}{N}\sum_{i=1}^{N}\boldsymbol{q}_f(\omega_i)$, $\bar{\boldsymbol{y}}_f = \frac{1}{N}\sum_{i=1}^{N}\boldsymbol{y}_f(\omega_i)$, $\bar{\varepsilon} = \frac{1}{N}\sum_{i=1}^{N}\boldsymbol{\varepsilon}(\eta_i)$.

2.5.3 Nonlinear formulation

Bayesian inference formulated as a linearised version of conditional expectation may be inaccurate if the observation operator is highly nonlinear. It can, however, be extended to a nonlinear formulation, where the conditional expectation is approximated with higher order terms.

If one assumes a quadratic map of the conditional expectation as

$$\mathbb{E}(\boldsymbol{q}_f|\boldsymbol{z}_f) \approx \varphi(\boldsymbol{z}_f) := {}^2\boldsymbol{H}\boldsymbol{z}_f^2 + {}^1\boldsymbol{H}\boldsymbol{z}_f + {}^0\boldsymbol{H}, \tag{2.38}$$

in which ${}^2\boldsymbol{H}$, ${}^1\boldsymbol{H}$ and ${}^0\boldsymbol{H}$ denote the coefficients derived from a minimisation problem analogous to the one in Eq. (2.21).

The linear filtering Eq. (2.26) is now extended for the additional terms as

$$\begin{aligned}\boldsymbol{q}_a(\omega,\eta) &= \boldsymbol{q}_f(\omega) + {}^2\boldsymbol{H}(\hat{\boldsymbol{z}}^2 - \boldsymbol{z}_f^2(\omega,\eta)) + {}^1\boldsymbol{H}(\hat{\boldsymbol{z}} - \boldsymbol{z}_f(\omega,\eta)) \\ &= \boldsymbol{q}_f(\omega) + \boldsymbol{P} : \boldsymbol{R}^{-1}(\hat{\boldsymbol{z}}^2 - \boldsymbol{z}_f^2(\omega,\eta)) + (\boldsymbol{K} - \boldsymbol{P} : \boldsymbol{R}^{-1}\boldsymbol{F})(\hat{\boldsymbol{z}} - \boldsymbol{z}_f(\omega,\eta)),\end{aligned} \tag{2.39}$$

where $\boldsymbol{K}$ is the Kálmán gain from Eq. (2.27) and matrices $\boldsymbol{F}$, $\boldsymbol{P}$ and $\boldsymbol{R}$ are defined as

$$\boldsymbol{F} = \boldsymbol{C}_{\boldsymbol{y}_f^2,\boldsymbol{y}_f}(\boldsymbol{C}_{\boldsymbol{y}_f} + \boldsymbol{C}_{\boldsymbol{\varepsilon}})^\dagger, \tag{2.40}$$

$$\boldsymbol{P} = \boldsymbol{C}_{\boldsymbol{q}_f,\boldsymbol{y}_f^2} - \boldsymbol{C}_{\boldsymbol{q}_f,\boldsymbol{y}_f}(\boldsymbol{C}_{\boldsymbol{y}_f} + \boldsymbol{C}_{\boldsymbol{\varepsilon}})^\dagger \boldsymbol{C}_{\boldsymbol{y}_f,\boldsymbol{y}_f^2}, \tag{2.41}$$

$$\boldsymbol{R} = \boldsymbol{C}_{\boldsymbol{y}_f^2} - \boldsymbol{C}_{\boldsymbol{y}_f^2,\boldsymbol{y}_f}(\boldsymbol{C}_{\boldsymbol{y}_f} + \boldsymbol{C}_{\boldsymbol{\varepsilon}})^\dagger \boldsymbol{C}_{\boldsymbol{y}_f,\boldsymbol{y}_f^2}. \tag{2.42}$$

A full derivation and comparison with the linear Bayesian update is given in [102].

2.5.4 Sequential approach

Filtering approaches are well suited for sequential estimation of parameters in time-dependent problems. Namely, immediately upon the first set of observations $\hat{\boldsymbol{z}}^{(k)}$ at a discrete update step t_k is available, an estimate of the model parameters $\boldsymbol{q}_a^{(k)}$ is produced. The process is repeated for each update step, altering the knowledge about the uncertain model parameters with each new observation. The filtering Eq. (2.26) rewritten in a sequential form reads

$$\forall k : \boldsymbol{q}_a^{(k)}(\omega,\eta) = \boldsymbol{q}_f^{(k)}(\omega) + \boldsymbol{K}\left(\hat{\boldsymbol{z}}^{(k)} - \left(\boldsymbol{y}^{(k)}(\omega) + \boldsymbol{e}^{(k)}(\eta)\right)\right), \tag{2.43}$$

with the prediction of noisy observations taking the form of

$$\forall k : \boldsymbol{z}_f^{(k)}(\omega,\eta) = Y_{Q,\Delta t}\left(\boldsymbol{q}_f^{(k)}(\omega), \boldsymbol{u}_f^{(k)}(\omega), \Delta t\right) + \boldsymbol{\varepsilon}^{(k)}(\eta). \tag{2.44}$$

where the posterior from the previous step $\boldsymbol{q}_a^{(k-1)}(\omega,\eta)$ now becomes prior $\boldsymbol{q}_f^{(k)}(\omega,\eta)$ for the current step. Whenever a new set of observations is

gathered and the probabilistic description of random parameters is updated, the current state $\boldsymbol{u}_f^{(k)}(\omega) = \boldsymbol{u}_a^{(k-1)}(\omega)$ needs to be altered as well. In its updated form, $\boldsymbol{u}_a^{(k)}(\omega)$, the state is further used for computing the prediction of the observations $\boldsymbol{y}_f^{(k+1)}(\omega)$, resulting from the propagation of prior uncertainty from the update step t_k to t_{k+1}.

The computational procedure of a sequential PCE-based GMKF is summarised in Algorithm 1 for N_t update steps and N samples of random parameters.

Algorithm 1: Sequential PCE-based sampling-free GMKF

loop over discrete update steps
for $t = t_{k-1}, \ldots, t_k;\ k \in \{1, \ldots, N_t\}$ **do**

- define prior densities of the uncertain model parameters $\pi(\boldsymbol{q}_f(t_k)) = \pi(\boldsymbol{q}_a(t_{k-1}))$

loop over samples of prior distribution
for $n = 1, \ldots, N$ **do**

- run the FE solver wrt. samples of $\pi(\boldsymbol{q}_f(t_k))$ $\boldsymbol{y}_f(t_k) = Y_{Q,\Delta t}(\boldsymbol{q}_f(t_k), \boldsymbol{u}_f(t_k), \Delta t);\ \Delta t = t_k - t_{k-1}$

end

- make PCE (in extended basis) of:
  (a) predicted uncertain parameters $\boldsymbol{q}_f(t_k, \boldsymbol{\theta}, \boldsymbol{\xi}) \approx \sum_{\gamma \in \mathcal{J}_G} \boldsymbol{q}^{(\gamma)} \Psi_\gamma(t_k, \boldsymbol{\theta}, \boldsymbol{\xi})$,
  (b) predicted observations $\boldsymbol{y}_f(t_k, \boldsymbol{\theta}, \boldsymbol{\xi}) \approx \sum_{\gamma \in \mathcal{J}_G} \boldsymbol{y}^{(\gamma)} \Psi_\gamma(t_k, \boldsymbol{\theta}, \boldsymbol{\xi})$,
  (c) measurement error $\boldsymbol{\varepsilon}(t_k, \boldsymbol{\theta}, \boldsymbol{\xi}) \approx \sum_{\gamma \in \mathcal{J}_G} \boldsymbol{e}^{(\gamma)} \Psi_\gamma(t_k, \boldsymbol{\theta}, \boldsymbol{\xi})$,
  (d) actual observations $\hat{\boldsymbol{z}}(t_k, \boldsymbol{\theta}, \boldsymbol{\xi}) \approx \sum_{\gamma=0} \boldsymbol{z}^{(0)} \Psi_\gamma(t_k, \boldsymbol{\theta}, \boldsymbol{\xi})$
- update PCE coeff. of the uncertain parameters by PCE-GMKF $\boldsymbol{q}_a^{(k,\gamma)} = \boldsymbol{q}_f^{(k,\gamma)} + \boldsymbol{K}\left(\hat{\boldsymbol{z}} - \left(\boldsymbol{y}_f^{(k,\gamma)} + \boldsymbol{\varepsilon}^{(k,\gamma)}\right)\right)$
- update the state: run the FE solver wrt. samples of $\pi(\boldsymbol{q}_a(t_k))$

end

Chapter 3

Modelling of quasi-brittle fracture in concrete

"A model is a good model if first it interprets a wide range of observations in terms of a simple and elegant model, and second if the model makes definite predictions that can be tested, and possibly falsified, by observation."

S. Hawking

Concrete is the most extensively used building material due to its many remarkable properties, among which its ability to be cast into almost any shape, its water and high-temperature resistance, while being economically efficient and having low maintenance requirements. Though, its biggest drawback is its low tensile strength which is only a small fraction (approximately 10 times) of its compressive strength.

The addition of steel bars into plain concrete significantly improves concrete's ability to withstand shear and tensile loads, making it a common choice for design of massive structures for which durability plays an important role. Although the appearance and propagation of damage in concrete is just a matter of time, structures built of reinforced concrete typically do not fail, as steel takes over carrying tensile forces upon cracking of concrete. While

concrete softens, a properly designed reinforcement alleviates the brittleness of plain concrete, leading to a more ductile response and more favourable crack patterns.

When the tensile force in concrete is considerably below the ultimate load, the composite behaves elastically, characterised by concrete and steel sharing the same deformation. At moderate levels of load below the serviceability limit, heterogeneities at the interface between aggregate and cement paste become locations of the microscopic crack nucleation induced by tensile stresses. A further increase in load causes the coalescence of the microscopic cracks, forming a *fracture process zone* (FPZ) in the weakest region of a structural member, indicating the start of material hardening. When the load is further increased and stresses in concrete reach its tensile strength, the material is subjected to a more prominent degradation characterised by the *strain-softening* behaviour. Microscopic damage in the FPZ further evolves and takes the form of a macroscopic crack, while the surrounding material unloads. Macroscopic crack propagates through the FPZ, eventually leading to *localised failure* in concrete. At this stage, concrete ceases to contribute to the carrying capacity of the member at the locations of macro-cracks, as the stress transfer between the cracked parts of the cross section is no longer possible and the entire amount of tensile force is carried by steel. At considerably higher levels of load, tensile stresses in steel reach the yielding point, causing the structural members to exhibit sizeable permanent (plastic) deformation under constant load. The latter scenario is not explored within this work.

Another important aspect of the material behaviour in the presence of damage is the quality of the bond between concrete and steel. Namely, once concrete is cracked, bond plays a crucial role in stress redistribution by permitting the transfer of stresses between concrete and steel even beyond cracking in concrete taking place. Due to bond between concrete and steel, the intact section of concrete between adjacent cracks carries a portion of tensile force normal to the cracked plane and contributes to the overall stiffness of the specimen, which is known as *tension-stiffening* property. Besides, efficient bond provides a good resistance to slip of the steel bars with respect to surrounding concrete, which also affects the crack patterns. It eventually leads to a larger number of fine, narrow cracks, as opposed to bond with a weaker grip leading to a small number of rather wide cracks. In general practice, the quality of the bond is ensured by giving preference to ribbed reinforcement bars over the smooth ones.

3.1 An overview of numerical methods for fracture simulation

The first attempts on modelling of propagation of fracture in materials stem from the work of Griffith [60], one of the pioneers of the theory of *linear elastic fracture mechanics*, which considers the initial defects as an inherent material property. The propagation of these defects and formation of macroscopic cracks is further governed by the energy release rate exceeding the critical value.

Since then, two main trends in computational modelling of quasi-brittle fracture in concrete have emerged: *discrete* crack concept and *smeared* crack representations [32], extensively used within the finite element framework. Noteworthy attempts on modelling fracture in concrete date back to 1960s with the works of Ngo and Scordelis [121] and Rashid [143], introducing the aforementioned fracture modelling concepts.

The latter work outlines the concept of the smeared crack approach, where a cracked solid is assumed to be a continuum, with cracks being smeared over a distinct region and represented in terms of narrow bands of high strains. However, the assumption of the displacement continuity stands in the high contrast with the notion of a crack as a geometrical discontinuity. The crack bands in the smeared approach, though, might better support the idea of a fracture process zone characterised by the appearance of many microscopic discontinuities distributed within a region ahead of the tip of a macroscopic crack. Moreover, this approach is superior for modelling of diffuse cracking, e.g. in large-scale shear panels, where the scale of the specimen is significantly larger than the scale of the crack spacing [146]. Mesh objectivity is in this case ensured by regularisation of the constitutive models with respect to mesh size and crack band width, thereby preserving the fracture energy. Details on the implementation and applications can be found in [181, 180, 176, 15, 147, 33, 14] for a fixed orientation of cracks throughout the whole computation and in [29, 187, 61], where the traditional concept is extended in order to allow rotations of cracks alongside the principal strain axes.

The counterpart of the smeared crack approach is the discrete crack concept, elaborated in [121, 127, 179, 76]. The respective approach is based on principles of fracture mechanics, modelling a crack as a geometric entity by introducing the displacement discontinuity. In contrast to the smeared crack approach where material degradation is expressed by means of stress-strain

relations within a crack band, here constitutive response is defined in terms of a cohesive traction-separation law. In finite element setting, cracks are usually resolved either by separating the edges of the finite elements or by introducing the interface finite elements at the locations of discontinuities. The biggest drawback of the method is the fact that the location of crack opening and crack propagation path need to be predefined. Hence, unlike the smeared crack approach which retains the initial topology of the finite element mesh, the discrete approach often requires the use of adaptive remeshing techniques, which makes its finite element implementation rather onerous. Although the discrete crack approach is a preferred choice for modelling localised failure, its complex implementation limits its widespread use in practice.

In recent decades, new methods for modelling quasi-brittle fracture have emerged in order to alleviate the implementation shortcomings, while promoting the favourable features of the aforementioned modelling concepts. Of particular interest is the *strong embedded discontinuity* approach [161, 129, 84, 120, 131], based on enhancement of the classical theoretical formulation of the finite elements by including the discontinuous displacement modes. Propagation of macroscopic cracks is thereby modelled by displacement jumps across the discontinuity surface. The strain field in this case consists of a regular and a singular part. Depending on the character of enrichment of the kinematics of standard finite elements, a distinction is made between the *embedded (strong) discontinuity* finite element method (ED-FEM) [82, 101, 72, 189] and the *extended* finite element method (X-FEM) [17, 118, 117, 83, 18, 168] based on the notion of *partition of unity* (PUFEM) [113, 10].

In ED-FEM, the enrichment of the displacement field is local, with additional degrees of freedom along the discontinuity surface being condensed at the element level. In X-FEM, on the other hand, the nature of the enrichment is global, with additional degrees of freedom attached to the nodes of finite elements located at the discontinuity surface. In that regard, the former method acts as a localisation limiter and by stabilising the localised fracture process zone it leads to a mesh-independent release of fracture energy [69]. It is able to capture the displacement jump across an arbitrary crack path, which is in better accordance with the random nature of the cracking process. Namely, crack paths can significantly vary within the same population of specimens, subjected to the same loading and boundary conditions, due to strong dependence of the crack propagation on the material mesostructure and initial defects. The embedded discontinuity approach is employed in various structural and solid applications involving modelling of mechanisms

of inelastic material behaviour, see, e.g. [40, 4, 23, 39, 130, 8, 150, 123, 164, 165].

Unlike ED-FEM, the extended finite element method suffers from the cumbersome implementation, as the additional degrees of freedom appear globally, altering the dimensions of the stiffness matrix and residual throughout the simulation. Nevertheless, the X-FEM method is preferred in cases where the treated phenomena is indeed global, e.g. in the case of modelling of bond-slip in reinforced concrete, where the additional degrees of freedom capturing the slip at the concrete-steel interface need to stay connected [37, 70, 149].

More recent developments in modelling of fracture come in terms of a special class of discrete models, the so-called *lattice* models [67, 63, 157, 156, 154, 155, 134, 126], which are able to capture the material mesostructure and complex crack paths, including the crack branching and coalescence of multiple cracks. The material mesostructure is mapped onto a lattice consisting of an assembly of discrete one-dimensional elements, the properties of which reflect the distinct phases of composite materials, e.g. cement matrix and aggregate. Lattice models can be implemented together with classical remeshing techniques [76] in order to simulate fracture or, following a more refined approach, in the spirit of ED-FEM by embedding the discontinuities in each beam member, see, e.g. [125, 124].

Another relatively recent addition to the class of models for fracture propagation are the energy minimisation based *phase-field* models stemming from the Francfort and Marigo's variational formulation [46]. These models, belonging to the class of gradient damage models [34], are recently gaining a lot of attention due to their ability to predict complex crack patterns by solving the partial differential equations. The state of the material is described by means of a continuous field variable, ranging from the intact to a fully damaged material state, which provides a smooth transition between the fracture phases and avoids explicit modelling of cracks as geometrical discontinuities [116, 5].

This work follows the approach introduced by Brancherie and Ibrahimbegovic [23], in which fracture in concrete is modelled by a combined cracking model able to account for two distinct types of dissipation: a volume dissipation governed by the diffuse damage mechanisms at formation of the FPZ and a surface dissipation corresponding to localised failure due to propagation of a macroscopic crack. Cracks are modelled with the enhanced kinematics by incorporating the embedded discontinuities, implemented in the spirit of *incompatible modes* [74], whereas the consequent relative slip between concrete

and steel is modelled in terms of X-FEM, where all slips are connected along a single reinforcement bar.

In the next stage, lattice model consisting of discrete beam elements enhanced by embedded discontinuities is employed to reproduce the geometry obtained from the computed tomography scan and fracture pattern resulting from a double shear test. Both of the chosen approaches are briefly introduced in the following sections.

3.2 Predictive damage model for simulation of fracture in reinforced concrete

Concrete is a heterogeneous, multi-scale material, the properties of which are conditioned by the scale of the problem. On the scale of structural members, here denoted as *coarse-scale*, it is considered to be homogeneous and hence can be modelled as a continuum, following the principles of continuum mechanics. Thus, on the coarse-scale composite consists of concrete, steel reinforcement and the bond between them.

Cracking, as an essential part of tensile behaviour of concrete, ranges from diffuse microscopic discontinuities nucleating in the fracture process zone to their coalescence in the form of macroscopic cracks and localised failure. Localised failure in quasi-brittle materials is typically accompanied by the strain-softening phenomenon, characterised by a further increase of deformations, while the surrounding material outside of the fracture process zone experiences unloading. This behaviour is usually described by suitable models based on principles of nonlinear fracture mechanics, damage mechanics or plasticity. A special care needs to be put into modelling of the post-peak behaviour characterised by the total *fracture energy*, which can be visualised as the area under the softening curve. In the context of this work, behaviour of concrete is described by an elasto-damage model able to account for both formation of microscopic damage in the bulk material and localised cracking. Model derives from the work of Brancherie et al. (see [23, 22] and references thereof). Total failure of a specimen and a complete pull-out of the reinforcement bar is beyond the scope of this work, thus steel is modelled with a simple linear elasticity. Bond-slip at the concrete-steel interface is considered as an inelastic deformation and modelled with an elasto-plastic law. Constitutive laws for all three ingredients of the composite are shown in Fig. 3.1.

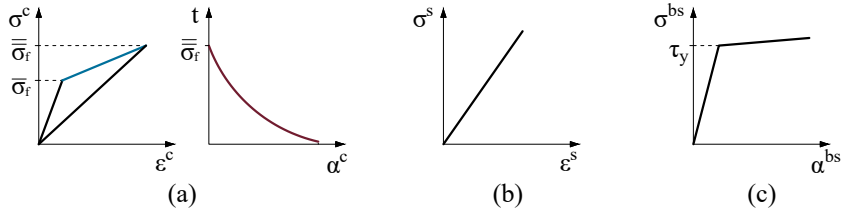

Figure 3.1: Constitutive laws: a) concrete elasto-damage model with hardening and softening; b) linear elastic model for steel; c) elasto-plastic bond-slip model

In the following sections, both damage models describing different mechanisms of energy dissipation due to cracking are briefly introduced. Propagation of macroscopic cracks in concrete leads to degradation of the bond, the result of which is the frictional slip of the reinforcement bar with respect to surrounding concrete. The redistribution of stresses taking place upon cracking in concrete ultimately determines the final crack spacing and opening. Hence, an overview of the damage model for concrete is followed by a formulation of the bond model capable of capturing the bond-slip at the concrete-steel interface. Numerical model is originally developed by Rukavina et al. [148, 149] (see also references of the earlier contributions to the topic, e.g. [70, 21, 37, 36, 139]) and modified in the context of this thesis to cope with the problem-specific peculiarities.

3.2.1 Continuum damage model for simulation of diffuse fracture in concrete bulk

Concrete and steel have the same thermal expansion coefficient, which is making them mutually constrained by sharing the same value of strain at their undamaged state. Moreover, at relatively low stress levels, bond between them is still intact, allowing the transfer of forces between concrete and steel and thereby their mutual efforts in carrying the external loads. In this phase, composite can be modelled as a linear elastic continuum following Hooke's law.

At levels of stress above the elasticity limit, the initial elastic response is replaced by the inelastic effects in the concrete bulk. The formation of the FPZ in the bulk material and progressive development of the microscopic

cracks (Fig. 3.2) indicate the initiation of fracture in concrete. Evolution of damage in the bulk is modelled by the *isotropic damage model* of *Kachanov* with *associated isotropic hardening* (see, e.g. [69] for details of the formulation) and represented in terms of two internal variables, tensor of damage compliance $\bar{\boldsymbol{D}}$ and a scalar hardening variable $\bar{\xi}$. The admissibility of stress field is verified by the isotropic damage criterion expressed as

$$\bar{\phi}(\boldsymbol{\sigma}, \bar{q}(\bar{\xi})) = \| \boldsymbol{\sigma} \|_{\boldsymbol{D}^e} - \frac{1}{\sqrt{E^c}}(\bar{\sigma}_f - \bar{q}(\bar{\xi})) \leq 0, \tag{3.1}$$

where $\bar{\phi}(\boldsymbol{\sigma}, \bar{q}(\bar{\xi})) < 0$ denotes the elastic domain. The term $\bar{\boldsymbol{D}} = \boldsymbol{D}^e$ in Eq. (3.1) is the elastic compliance tensor for the bulk material, E^c is the Young's modulus for concrete and $\bar{\sigma}_f$ is the elasticity limit. The term $\bar{q}(\bar{\xi})$ denotes the stress-like hardening variable accounting for evolution of damage threshold, here governed by a linear isotropic hardening law

$$\bar{q}(\bar{\xi}) = -\bar{K}\bar{\xi}, \tag{3.2}$$

with $\bar{K}$ being the hardening modulus. The elasticity limit and hardening modulus govern the start and progression of damage propagation in the FPZ and thus they are among the target parameters, which need to be identified given experimental data.

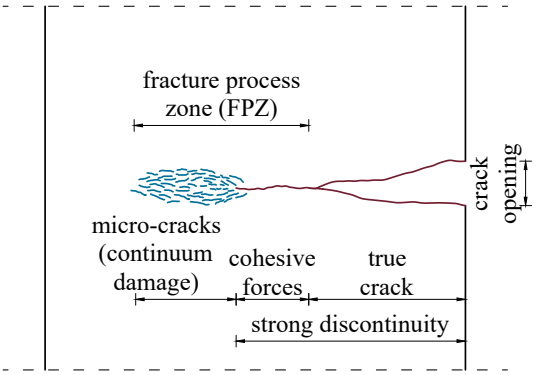

Figure 3.2: Diffuse and localised fracture

3.2.2 Strong embedded discontinuity model for simulation of localised failure in concrete

The increase of load is accompanied by the progression of damage and coalescence of microscopic cracks into a macroscopic one represented by a discontinuity surface. This results in surface dissipation and development of a localisation zone. Once principal stress σ_{pr} reaches the tensile strength of concrete, material exhibits strain-softening behaviour, which is modelled by means of an *anisotropic multi-surface damage model* [100, 69]. The post-peak softening response is characterised by a decrease in traction and an increase in crack opening (Fig. 3.1(a)), as the crack surfaces across the crack tip are gradually separated. That is known as the cohesive approach formulated in terms of a *traction-separation law*, which relates the traction $\boldsymbol{t}$ at the discontinuity and the crack opening $\boldsymbol{\alpha}^c$ as

$$\boldsymbol{t} = \bar{\bar{\boldsymbol{Q}}}^{-1}\boldsymbol{\alpha}^c, \tag{3.3}$$

where $\bar{\bar{\boldsymbol{Q}}}$ denotes the damage compliance tensor at the discontinuity.

In this work, it is assumed that fracture in concrete can be realised either as the crack opening due to tensile stress in normal direction (mode I) or as sliding along the discontinuity surface due to shear stress in the tangential direction (mode II) with respect to the discontinuity surface. Each of the modes is taken into account separately by formulating two uncoupled damage laws, one for each direction at the discontinuity surface, as

$$\bar{\bar{\phi}}_1(\boldsymbol{t}, \bar{\bar{q}}(\bar{\bar{\xi}})) = \boldsymbol{t}\cdot\boldsymbol{n} - (\bar{\bar{\sigma}}_f - \bar{\bar{q}}(\bar{\bar{\xi}})) \leq 0, \tag{3.4}$$

$$\bar{\bar{\phi}}_2(\boldsymbol{t}, \bar{\bar{q}}(\bar{\bar{\xi}})) = |\boldsymbol{t}\cdot\boldsymbol{m}| - (\bar{\bar{\sigma}}_s - \frac{\bar{\bar{\sigma}}_s}{\bar{\bar{\sigma}}_f}\bar{\bar{q}}(\bar{\bar{\xi}})) \leq 0, \tag{3.5}$$

where Eq. (3.4) takes into account fracture due to the normal component of traction, $\boldsymbol{n}$, and Eq. (3.5) models the shear effects introduced by the tangential counterpart, $\boldsymbol{m}$. The ratio $\frac{\bar{\bar{\sigma}}_s}{\bar{\bar{\sigma}}_f}$ in Eq. (3.5) relates the ultimate stress in shear $\bar{\bar{\sigma}}_s$ to the ultimate stress in tension $\bar{\bar{\sigma}}_f$. The term $\bar{\bar{q}}(\bar{\bar{\xi}})$ refers to the traction-like softening variable which depends upon strain-like softening variable $\bar{\bar{\xi}}$ that can incur either by mode I or mode II fracture process. Fracture evolves under the assumption of exponential post-peak behaviour, which takes the form of

$$\bar{\bar{q}}(\bar{\bar{\xi}}) = \bar{\bar{\sigma}}_f\left[1 - \exp\left(-\frac{\bar{\bar{\beta}}^c}{\bar{\bar{\sigma}}_f}\bar{\bar{\xi}}\right)\right], \tag{3.6}$$

in which $\bar{\bar{\beta}}^c$ denotes the initial slope of the softening curve.

In discrete approximation, the zones of localisation of deformation are taken into account through the introduction of strong discontinuities of the displacement field. Once the maximum principal stress reaches the value of the ultimate stress, a macro-crack perpendicular to the direction of the maximum principal stress is embedded into the corresponding finite element. The crack opening is taken into account through an incompatible mode function [72], thus the total displacement field is a sum of the standard compatible and the incompatible part such that

$$\boldsymbol{u}^c(\boldsymbol{x}) = \boldsymbol{N}\boldsymbol{d}^c + \boldsymbol{M}\boldsymbol{\alpha}^c, \tag{3.7}$$

where $\boldsymbol{d}^c$ are the nodal displacements for standard degrees of freedom, whereas $\boldsymbol{\alpha}^c$ stands for the crack opening defined by means of the incompatible displacements. The theoretical framework for such enhancement of kinematics is provided by the method of incompatible modes and *Hu-Washizu mixed variational formulation* [161, 184]. The terms $\boldsymbol{N}$ and $\boldsymbol{M}$ refer to the standard linear and incompatible shape functions [69], respectively. The incompatible shape functions are defined as

$$\boldsymbol{M} = M\boldsymbol{I}; \quad M = H_\Gamma - \sum_{a \in \Omega^{e+}} N_a, \tag{3.8}$$

where H_Γ denotes the Heaviside function taking a unit value inside the subdomain Ω^{e+} and zero elsewhere.

As a result of introducing the strong discontinuity of the displacement field in Eq. (3.7), the strain field is also enhanced in terms of incompatible modes as

$$\boldsymbol{\epsilon}^c(\boldsymbol{x}) = \boldsymbol{B}\boldsymbol{d}^c + \boldsymbol{G}_r\boldsymbol{\alpha}^c, \tag{3.9}$$

where $\boldsymbol{B}$ and $\boldsymbol{G}_r$ are the derivatives of the standard and the incompatible shape functions, respectively. The operator $\boldsymbol{G}_r$ can be additively decomposed into a regular (bounded) $\bar{\boldsymbol{G}}_r$ part and a singular part $\bar{\bar{\boldsymbol{G}}}_r = \boldsymbol{n}\delta_{\Gamma_s}$, where $\boldsymbol{n}$ is the normal vector at the discontinuity and δ_{Γ_s} is the Dirac delta function centered at the crack discontinuity surface Γ_s.

Energy dissipation in reinforced concrete is a result of an irreversible dissipative process in which energy introduced into the system by external loads is converted to other forms (e.g. heat), followed by an increased production of entropy. The corresponding free energy of Helmholtz $\psi(\boldsymbol{\varepsilon}, \boldsymbol{D}, \xi)$ represents

the thermodynamic potential of the chosen damage model and is formulated such that it takes into account both hardening and softening contribution as

$$\begin{aligned}\psi(\boldsymbol{\varepsilon},\boldsymbol{D},\xi) &= \underbrace{\frac{1}{2}\boldsymbol{\varepsilon}\bar{\boldsymbol{D}}^{-1}\boldsymbol{\varepsilon}+\bar{\Xi}(\bar{\xi})}_{\psi(\boldsymbol{\varepsilon},\bar{\boldsymbol{D}},\bar{\xi})}+\underbrace{\frac{1}{2}\boldsymbol{\alpha}^c\bar{\bar{\boldsymbol{Q}}}^{-1}\boldsymbol{\alpha}^c+\bar{\bar{\Xi}}(\bar{\bar{\xi}})}_{\psi(\boldsymbol{\alpha}^c,\bar{\bar{\boldsymbol{Q}}},\bar{\bar{\xi}})}\delta_{\Gamma_s};\\ \bar{\Xi}(\bar{\xi}) &= -\bar{q}\bar{\xi};\quad \bar{\bar{\Xi}}(\bar{\bar{\xi}})=-\bar{\bar{q}}\bar{\bar{\xi}},\end{aligned} \tag{3.10}$$

where $\boldsymbol{\varepsilon}$ is total strain of concrete, $\bar{\boldsymbol{D}}$ and $\bar{\bar{\boldsymbol{Q}}}$ are respectively the damage compliance tensor for the bulk and damage compliance tensor at the discontinuity and $\boldsymbol{\alpha}^c$ is the displacement jump or the crack opening. The terms $\bar{\xi}$ and $\bar{\bar{\xi}}$ denote the internal variables which control hardening and softening, respectively. As introduced in Eq. (3.10), the free energy upon opening of a macro-crack is decomposed into a regular part $\psi(\boldsymbol{\varepsilon},\bar{\boldsymbol{D}},\bar{\xi})$, accounting for the hardening in the fracture process zone, and the irregular part $\psi(\boldsymbol{\alpha}^c,\bar{\bar{\boldsymbol{Q}}},\bar{\bar{\xi}})$, accounting for the strain-softening at the crack localisation point which is introduced by the Dirac delta δ_{Γ_s} function. The physical nature of evolution of inelastic free energy is associated with particle rearrangement in the composite [69].

In a purely mechanical framework, where the thermal effects are ignored, dissipation of energy is governed by the evolution of internal variables employed by the inelastic constitutive models (e.g. plastic deformation, damage compliance, hardening and softening variables) [69]. Calculation of the total energy dissipation rate follows directly from the non-local form of the second law of thermodynamics, stating that the entropy production in a thermodynamic process is non-negative [175, 105]. Applying the Legendre transform [69] to represent the Helmholtz free energy in terms of its energy potential counterpart defined through stresses, the total dissipation due to damage reads

$$\begin{aligned}0 &< \dot{D}^d(\boldsymbol{\varepsilon},\bar{\boldsymbol{D}},\bar{\xi},\boldsymbol{\alpha}^c,\bar{\bar{\boldsymbol{Q}}},\bar{\bar{\xi}})\\ &= \int_{\Omega^e}\left[\boldsymbol{\sigma}\;\dot{\boldsymbol{\varepsilon}}-\dot{\psi}(\boldsymbol{\varepsilon},\bar{\boldsymbol{D}},\bar{\xi})\right]d\Omega^e\;+\int_{\Gamma_s}\left[\boldsymbol{\sigma}\;\dot{\boldsymbol{\alpha}}^c-\dot{\psi}(\boldsymbol{\alpha}^c,\bar{\bar{\boldsymbol{Q}}},\bar{\bar{\xi}})\right]d\Gamma_s\\ &= \int_{\Omega^e}\frac{1}{2}\boldsymbol{\sigma}\dot{\bar{\boldsymbol{D}}}\boldsymbol{\sigma}\;d\Omega^e+\int_{\Omega^e}\bar{q}\dot{\bar{\xi}}d\Omega^e\;+\int_{\Gamma_s}\frac{1}{2}\;\boldsymbol{t}_{\Gamma_s}\dot{\bar{\bar{\boldsymbol{Q}}}}\boldsymbol{t}_{\Gamma_s}\;d\Gamma_s+\int_{\Gamma_s}\bar{\bar{q}}\dot{\bar{\bar{\xi}}}\;d\Gamma_s\end{aligned} \tag{3.11}$$

where $\boldsymbol{t}_{\Gamma_s}=(\boldsymbol{\sigma}\boldsymbol{n})_{\Gamma_s}$ is the traction at the discontinuity defined in Eq. (3.3).

In addition to the surface dissipation, one may also define the energy needed

to break the specimen or the fracture energy as

$$G_f = \int_{\Gamma_s} \int_{t_{loc}}^{\infty} \boldsymbol{t}\dot{\boldsymbol{\alpha}}^c \; dt \; d\Gamma_s = \frac{\bar{\bar{\sigma}}_f^2 \; l_{\Gamma_s}}{\bar{\bar{\beta}}^c}, \tag{3.12}$$

where l_{Γ_s} is the length of the discontinuity and t_{loc} indicates the start of localisation. Fracture energy, along with the ultimate stress, is essential in the context of damage and cracking in concrete. While the opening of a macroscopic crack is conditioned by the value of the ultimate stress, its post-peak response is determined by the fracture energy. Hence, both of these material parameters are considered as parameters of interest which need to be inferred with the help of experimental data.

3.2.3 Bond-slip at the concrete-steel interface

Strength, durability and deformability of reinforced concrete, as well as the resulting crack patterns, are conditioned not only by the properties of concrete and steel, but by the properties of the bond as well. The principal role of the interface is to allow the redistribution of stresses between concrete and steel, where the mechanism of force transfer mainly depends on chemical adhesion, friction and mechanical interlocking produced by the reinforcement ribs embedded into concrete [24, 2]. Another important aspect of the bond is that it allows the transfer of tensile stresses from reinforcement to the surrounding concrete between the adjacent crack surfaces, which thereby contributes to the overall stiffness of the composite (tension-stiffening effect). Hence, as the bond plays a substantial role in the behaviour of reinforced concrete, a special attention needs to be payed to its modelling.

If concrete in the vicinity of the bond is well-confined with transverse reinforcement and sufficient concrete cover, the predominant type of bond failure is the pull-out of the reinforcement bar with respect to surrounding concrete. This type of bond failure is of a main concern for this work.

Due to the opening of macro-cracks, the compatibility between deformations of the reinforcement bar and surrounding concrete is no longer valid. As a result of the accumulation of strain differences, a relative displacement or bond-slip appears at the concrete-steel interface. The mechanism of bond-slip activation depends upon the energy balance condition. More precisely,

bond-slip contributes to the total strain energy of reinforced concrete and its contribution can be quantified as

$$\psi(\overline{\overline{\alpha}}^{bs}, \overline{\overline{\boldsymbol{D}}}, \overline{\overline{\xi}}) = \frac{1}{2}\overline{\overline{\alpha}}^{bs}\overline{\overline{\boldsymbol{D}}}^{-1}\overline{\overline{\alpha}}^{bs} + \overline{\overline{\Xi}}(\overline{\overline{\xi}}); \quad \overline{\overline{\Xi}}(\overline{\overline{\xi}}) = \frac{1}{2}\overline{\overline{\xi}}\,\overline{\overline{K}}\,\overline{\overline{\xi}}, \tag{3.13}$$

where $\overline{\overline{\alpha}}^{bs}$ is the approximation of bond-slip and the quantities $\overline{\overline{\boldsymbol{D}}}$, $\overline{\overline{\xi}}$ and $\overline{\overline{K}}$ denote the damage compliance, hardening displacement-like variable and hardening modulus for bond-slip, respectively.

Behaviour of the bond is commonly described through a relationship between the bond stress and corresponding relative slip of the reinforcement bar, which is formulated in terms of a suitable bond-slip law (see [68] and references thereof for an overview of recent trends in modelling of the bond). In this work, the bond is modelled by *hardening plasticity* within the thermodynamics framework, as proposed in [70] and [148]. The plastic slip is thus regarded as an accumulated inelastic deformation localised at the concrete-steel interface once the bond stress reaches the critical value denoted by τ_y. The latter is considered as uncertain and identified from the available experimental data.

The dissipation of energy due to bond-slip, induced by the fracture in concrete, takes place at the concrete-steel interface in the vicinity of macro-cracks in concrete. Its contribution to the total dissipation is quantified as

$$0 < \dot{D}^{bs}(\overline{\overline{\alpha}}^{bs}, \overline{\overline{\xi}}) = \int_{\Gamma_{bs}} \sigma^{bs}\dot{\overline{\overline{\alpha}}}^{bs}\, d\Gamma_{bs} + \int_{\Gamma_{bs}} \overline{\overline{q}}\dot{\overline{\overline{\xi}}}\, d\Gamma_{bs}, \tag{3.14}$$

where $\overline{\overline{q}}(\overline{\overline{\xi}})$ is the stress-like hardening variable for bond-slip and Γ_{bs} is the surface where bond-slip takes place.

3.2.3.1 Kinematics of a finite element with bond-slip

The inelastic slip $\overline{\overline{\xi}}$ remains as the permanent difference between concrete and steel displacements. It is represented in discrete approximation with the enhanced kinematics within the X-FEM. The core idea of applying the X-FEM method relies upon enriching the conventional finite element basis functions, $\boldsymbol{N}_a(\boldsymbol{x})$, in order to describe a function $\boldsymbol{\psi}(\boldsymbol{x})$ on a given sub-domain Ω^e as

$$\boldsymbol{\psi}(\boldsymbol{x}) = \sum_{a=1}^{n} \boldsymbol{N}_a(\boldsymbol{x})\Phi(\boldsymbol{x}), \tag{3.15}$$

where the functions $\boldsymbol{N}_a(\boldsymbol{x})$ satisfy the partition of unity, $\sum_{a=1}^{n} \boldsymbol{N}_a(\boldsymbol{x}) = 1$, the term $\boldsymbol{\Phi}(\boldsymbol{x})$ denotes a particular enrichment function and n stands for the number of nodes per element.

In X-FEM, the finite element approximation of a discontinuous displacement field can be partitioned into a sum of a standard and an enriched term as

$$\boldsymbol{u}(\boldsymbol{x})|_{\Omega^e} = \sum_{a=1}^{n} \boldsymbol{N}_a(\boldsymbol{x})\boldsymbol{d}_a^c + \sum_{b=1}^{n_{bs}} \boldsymbol{\psi}_b(\boldsymbol{x})\boldsymbol{\alpha}_b^{bs}, \tag{3.16}$$

where $\boldsymbol{d}_a^c$ are the standard nodal finite element degrees of freedom, $\boldsymbol{\alpha}_b^{bs}$ denote the newly added nodal degrees of freedom imposed at each of the n_{bs} nodes to which a particular reinforcement bar is attached and $\boldsymbol{u}(\boldsymbol{x})$ is the resulting displacement of a linear elastic reinforcement bar.

The enriched shape function basis $\boldsymbol{\psi}_b(\boldsymbol{x})$ with discontinuous features takes the following form

$$\boldsymbol{\psi}_b(\boldsymbol{x}) = \boldsymbol{N}_a(\boldsymbol{x})H(f(\boldsymbol{x})), \tag{3.17}$$

where $H(f(\boldsymbol{x}) = \boldsymbol{y})$ is the *Heaviside* step function with the following properties

$$H(\boldsymbol{y}) = \begin{cases} 1, & \boldsymbol{y} \geq \bar{\boldsymbol{y}} \\ 0, & \boldsymbol{y} < \bar{\boldsymbol{y}}, \end{cases} \tag{3.18}$$

in which $\bar{\boldsymbol{y}}$ is the location of the reinforcement bar indicating the discontinuity surface, i.e. the discontinuity line in 2D. By taking into account the properties of the Heaviside function given in Eq. (3.18), Eq. (3.16) can be rewritten as

$$\boldsymbol{u}(\boldsymbol{x})|_{\Omega^e} = \sum_{a=1}^{3} \boldsymbol{N}_a(\boldsymbol{x})\boldsymbol{d}_a^c + \sum_{a=1}^{2} \boldsymbol{N}_a(\boldsymbol{x})\boldsymbol{\alpha}_a^{bs}, \tag{3.19}$$

for the case when the reinforcement bar coincides with a finite element edge.

3.2.4 Variational formulation of the boundary value problem

Let us consider a 2D solid discretised by N_e triangular (CST) finite elements, each occupying a domain Ω^e. Its first variational equation is formulated as

$$\mathbb{A}_{e=1}^{N_e}(G^{int,e} - G^{ext,e}) = 0, \tag{3.20}$$

where $\mathbb{A}_{e=1}^{N_e}$ is the finite element assembly operator, whereas $G^{int,e}$ and $G^{ext,e}$ are the virtual work of the internal and external forces, respectively.

From Eq. (3.20), the weak from of the governing boundary value problem (BVP) can be constructed as

$$\mathbb{A}_{e=1}^{N_e}\left(\int_{\Omega^e}\nabla^s\boldsymbol{w}\boldsymbol{\sigma}d\Omega^e\right)-\mathbb{A}_{e=1}^{N_e}\left(\int_{\Omega^e}\boldsymbol{w}\boldsymbol{b}d\Omega^e+\int_{\Gamma_\sigma}\boldsymbol{w}\boldsymbol{t}_{\Gamma_\sigma}d\Gamma_\sigma\right)=0, \quad (3.21)$$

where $\boldsymbol{\sigma}$ is the stress field and vectors $\boldsymbol{b}$ and $\boldsymbol{t}_{\Gamma_\sigma}$ denote the body forces and traction acting at the specimen's boundary Γ_σ, respectively. The term $\boldsymbol{w}$ denotes the virtual displacement field, which is a sum of both standard and enhanced part as

$$\boldsymbol{w}(\boldsymbol{x})|_{\Omega^e}=\sum_{a=1}^{3}N_a(\boldsymbol{x})\boldsymbol{w}_a^c+\sum_{a=1}^{3}N_a(\boldsymbol{x})\boldsymbol{w}_a^{bs}, \quad (3.22)$$

where $\boldsymbol{w}_a^c$ and $\boldsymbol{w}_a^{bs}$ are the virtual displacements of concrete and bond-slip, respectively. By assuming that the load is applied solely through concrete, the virtual displacements composing the virtual work of external forces in Eq. (3.21) pertain to concrete displacements only. Taking this into consideration, Eq. (3.21) can be rewritten as

$$\mathbb{A}_{e=1}^{N_e}\left(\sum_{a=1}^{3}\boldsymbol{w}_a^c\ \boldsymbol{f}_a^{cs,int}+\sum_{a=1}^{3}\boldsymbol{w}_a^{bs}\ \boldsymbol{f}_a^{sbs,int}\right)-\mathbb{A}_{e=1}^{N_e}\left(\sum_{a=1}^{3}\boldsymbol{w}_a^c\ \boldsymbol{f}_a^{ext}\right)=0, \quad (3.23)$$

where $\boldsymbol{f}_a^{cs,int}$ and $\boldsymbol{f}_a^{sbs,int}$ denote vectors of element internal nodal forces, defined in the following manner

$$\begin{aligned}\boldsymbol{f}_a^{cs,int}&=\int_{\Omega^e}\nabla^s\boldsymbol{N}_a(\boldsymbol{x})\boldsymbol{\sigma}^c d\Omega^e+\int_{\Omega^e}\nabla^s\boldsymbol{N}_a(\boldsymbol{x})\boldsymbol{\sigma}^s d\Omega^e,\\ \boldsymbol{f}_a^{sbs,int}&=\int_{\Omega^e}\nabla^s\boldsymbol{N}_a^{bs}(\boldsymbol{x})\boldsymbol{\sigma}^s d\Omega^e+\int_{\Omega^e}\boldsymbol{N}_a^{bs}(\boldsymbol{x})\boldsymbol{\sigma}^{bs} d\Omega^e,\end{aligned} \quad (3.24)$$

and $\boldsymbol{f}_a^{ext}$ is the vector of the external forces defined as

$$\boldsymbol{f}_a^{ext}=\int_{\Omega^e}\boldsymbol{N}_a(\boldsymbol{x})\ \boldsymbol{b}\ d\Omega^e+\int_{\Gamma_\sigma}\boldsymbol{N}_a(\boldsymbol{x})\boldsymbol{t}d\Gamma_\sigma, \quad (3.25)$$

where $\boldsymbol{b}$ are the body forces and $\boldsymbol{t}$ is traction imposed at the boundary Γ_σ.

Considering that the components of the vector $\boldsymbol{w}_a^c$ are kinematically admissible, the terms associated with the concrete displacements in Eq. (3.23) yield the following set of equations

$$\boldsymbol{r}^{cs} = \mathbb{A}_{e=1}^{N_e} \left(\boldsymbol{f}_a^{c,int} + \boldsymbol{f}_a^{s,int} - \boldsymbol{f}_a^{ext} \right) = \boldsymbol{0}, \tag{3.26}$$

where the finite element assembly operator includes displacement boundary conditions as well. Eq. (3.26) can be regarded as a global equilibrium equation, whereas the remaining term in Eq. (3.23) forms the local equilibrium equation limited to the nodes to which the reinforcement bar is attached, accounting for the redistribution of the slip along the bar as

$$\boldsymbol{r}^{sbs} = \mathbb{A}_{e=1}^{N_e} \left(\boldsymbol{f}_a^{s,int} + \boldsymbol{f}_a^{bs,int} \right) = \boldsymbol{0}. \tag{3.27}$$

For a more thorough interpretation of the numerical implementation see [148].

3.3 Discrete lattice model for damage prediction in concrete

On finer scales, heterogeneities in the concrete mesostructure can no longer be neglected. In contrast to the coarse-scale at which the material is modelled as homogeneous, at the finer scale, or the so-called *meso-scale*, behaviour of the composite and its material properties are governed by the aggregate distributed in a cement matrix, the interface transition zone (ITZ) between them, water and the air voids. Hence, a more natural choice of modelling of such mesostructures are the discrete lattice models. The model is built of an assembly of spatial *Timoshenko* beams forming the *cohesive links* between the *Voronoi cells*, the size of which is comparable to the size of heterogeneities. The beam elements correspond to the edges of tetrahedrons generated by the *Delaunay triangulation* and their properties are assigned based on the common area between the two adjacent Voronoi cells [126].

As already pointed out, cracks in concrete are expected at the moderate load levels. Initial material imperfections, air voids and weak interfaces between aggregates and cement matrix weaken the fracture properties of the material and hence become locations of nucleation and further propagation of

macroscopic cracks leading to a brittle failure characteristic for plain concrete [50, 192]. The goal of the predictive model is thus to describe all possible mechanisms leading to localised failure with respect to inherent material heterogeneities. That is achievable by discretising the lattice in terms of Timoshenko beams, which are capable to resolve a complete set of 3D failure modes: bending failure (mode I), shear failure (modes II and III) and the mixed modes thereof (see Fig. 3.3). Kinematic enhancements are introduced in Timoshenko beams in a similar manner as shown for the solid finite elements in Section 3.2.2, here extended to 3D space. The lack of mesh objectivity and incorrect computation of the global fracture energy are alleviated by introducing the embedded strong discontinuities, which ensure that discontinuity remains localised inside a single beam element. The numerical model is based on previous works of Nikolić et al. [125, 124, 122, 88]. According to this formulation, the process of opening, coalescence and propagation of macroscopic cracks is evolving naturally and does not require implementation of tracking algorithms (see, e.g. [166] for an overview of path-following methods). The main ingredients of the 3D plasticity model with both hardening and softening are given in the following.

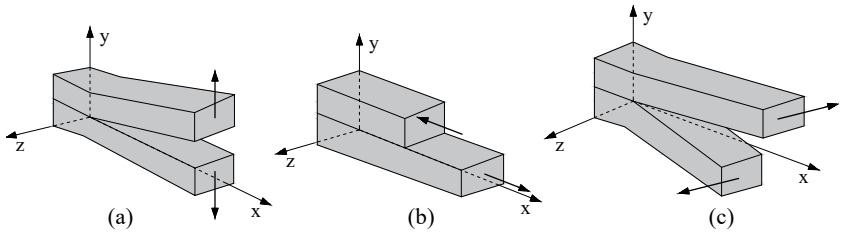

Figure 3.3: Failure modes of a Timoshenko beam: a) tensile crack-mouth opening; b) in-plane shear sliding; c) out-of-plane shear sliding

3.3.1 Enhanced kinematics of a 3D lattice model

The enhancement of kinematics for a chosen Timoshenko beam element with two nodes and a single Gauss integration point is implemented according to the procedure elaborated in Section 3.2.2. Here the formulation from Eq. (3.7) is extended to 3D space, with the beam nodal displacement vector $\boldsymbol{d} = [u \;\; v \;\; w \;\; \varphi \;\; \psi \;\; \theta]^T$ collecting the displacements and the corresponding rotations for all three coordinate directions, as shown in Fig. 3.4 (see, e.g. [106]

for the standard kinematics of Timoshenko beams). In a similar manner, the term $\boldsymbol{\alpha}^c$ in Eq. (3.7) now pertains to crack opening $\boldsymbol{\alpha} = [\alpha_u \;\; \alpha_v \;\; \alpha_w \;\; 0 \;\; 0 \;\; 0]^T$ in all three fracture modes.

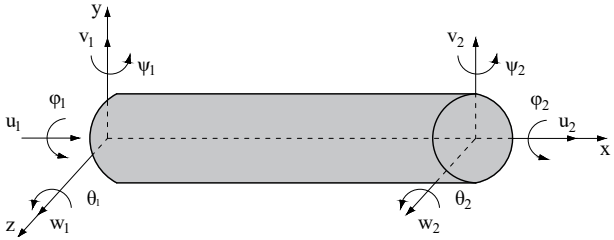

Figure 3.4: Timoshenko beam kinematics

3.3.2 Constitutive relations

Linear elasticity describes the behaviour of the material upon the initiation of the inelastic behaviour. The latter is characterised by energy dissipation due to plastification of beams upon reaching the yield stress in a particular mode, i.e. $\bar{\boldsymbol{\sigma}}_f = [\sigma_{y_c} \;\; \tau_{y_1} \;\; \tau_{y_2} \;\; 0 \;\; 0 \;\; 0]^T$, where σ_{y_c}, τ_{y_1} and τ_{y_2} denote the yield stresses in mode I, II and III, respectively. Activation of plasticity with isotropic linear hardening is defined through the yield functions expressed as

$$\bar{\phi}_u(\sigma, \bar{q}_u(\bar{\xi}_u)) = |\sigma| - (\sigma_{y_c} - \bar{q}_u(\bar{\xi}_u)) \leq 0, \tag{3.28}$$

$$\bar{\phi}_v(\tau_1, \bar{q}_v(\bar{\xi}_v)) = |\tau_1| - (\tau_{y_1} - \bar{q}_v(\bar{\xi}_v)) \leq 0, \tag{3.29}$$

$$\bar{\phi}_w(\tau_2, \bar{q}_w(\bar{\xi}_w)) = |\tau_2| - (\tau_{y_2} - \bar{q}_w(\bar{\xi}_w)) \leq 0. \tag{3.30}$$

in which the terms $\bar{q}_u$, $\bar{q}_v$ and $\bar{q}_w$ stand for the stress-like hardening variables defined according to linear isotropic hardening law as $\bar{q}_u = -K_c\bar{\xi}_u$, $\bar{q}_v = -K_{\tau_1}\bar{\xi}_v$ and $\bar{q}_w = -K_{\tau_2}\bar{\xi}_w$, where K_c, K_{τ_1} and K_{τ_2} are the hardening moduli and $\bar{\xi}_u$, $\bar{\xi}_v$ and $\bar{\xi}_w$ are the internal hardening variables.

In the work herein, modelling of concrete mesostructure is limited to three distinct material phases: aggregate and cement paste and the interface between them. In this case, fracture typically starts within the interface transition zone, being the weakest part of the composite. Upon the time instance in which the value of stress in the material reaches the value of the ultimate

stress $\bar{\bar{\boldsymbol{\sigma}}}_f$, the affected beams fail at their weakest point and subsequently activate the discontinuity embedded at the location of the Gauss integration point of the beam. The values of the ultimate stresses for each failure mode are collected in a vector $\bar{\bar{\boldsymbol{\sigma}}}_f = [\sigma_{u_t} \;\; \tau_{u_1} \;\; \tau_{u_2} \;\; 0 \;\; 0 \;\; 0]^T$, where σ_{u_t}, τ_{u_1} and τ_{u_2} denote the ultimate stresses in mode I, II and III, respectively. The typical failure modes are specified by the multi-surface criteria as

$$\bar{\bar{\phi}}_u(t_u, \bar{\bar{q}}_u(\bar{\bar{\xi}}_u)) = t_u - (\sigma_{u_t} - \bar{\bar{q}}_u(\bar{\bar{\xi}}_u)) \leq 0, \tag{3.31}$$

$$\bar{\bar{\phi}}_v(t_v, \bar{\bar{q}}_v(\bar{\bar{\xi}}_v)) = |t_v| - (\tau_{u_1} - \bar{\bar{q}}_v(\bar{\bar{\xi}}_v)) \leq 0, \tag{3.32}$$

$$\bar{\bar{\phi}}_w(t_w, \bar{\bar{q}}_w(\bar{\bar{\xi}}_w)) = |t_w| - (\tau_{u_2} - \bar{\bar{q}}_w(\bar{\bar{\xi}}_w)) \leq 0, \tag{3.33}$$

where t_u, t_v and t_w denote traction in mode I, II and III, respectively, localised at the discontinuity surface.

In practice, failure often occurs in the combination of modes rather than in a pure bending or pure shear mode. At this stage, material has entered the softening phase, characterised by the progressive opening of macroscopic cracks accompanied by unloading of the surrounding material. The terms $\bar{\bar{q}}_u(\bar{\bar{\xi}}_u)$, $\bar{\bar{q}}_v(\bar{\bar{\xi}}_v)$ and $\bar{\bar{q}}_w(\bar{\bar{\xi}}_w)$ in Eq. (3.31)-(3.33) refer to the stress-like softening variables defined as

$$\bar{\bar{q}}_u(\bar{\bar{\xi}}_u) = \sigma_{u_t}\left[1 - \exp\left(-\frac{\sigma_{u_t}}{\bar{\bar{G}}_{f_t}}\bar{\bar{\xi}}_u\right)\right], \tag{3.34}$$

$$\bar{\bar{q}}_v(\bar{\bar{\xi}}_v) = \tau_{u_1}\left[1 - \exp\left(-\frac{\tau_{u_1}}{\bar{\bar{G}}_{f_{\tau_1}}}\bar{\bar{\xi}}_v\right)\right], \tag{3.35}$$

$$\bar{\bar{q}}_w(\bar{\bar{\xi}}_w) = \tau_{u_2}\left[1 - \exp\left(-\frac{\tau_{u_2}}{\bar{\bar{G}}_{f_{\tau_2}}}\bar{\bar{\xi}}_w\right)\right], \tag{3.36}$$

where $\bar{\bar{G}}_{f_t}$, $\bar{\bar{G}}_{f_{\tau_1}}$ and $\bar{\bar{G}}_{f_{\tau_2}}$ are the characteristic unit fracture energies for softening in tension and shear directions. The amount of energy that the material absorbs during failure in particular fracture mode is computed as

$$G_{f_t} = \int_0^\infty \sigma_{u_t}\; exp\left(-\frac{\sigma_{u_t}}{\bar{\bar{G}}_{f_{\tau_1}}}\bar{\bar{\xi}}_u\right)\; d\bar{\bar{\xi}}_u, \tag{3.37}$$

$$G_{f_{\tau_1}} = \int_0^\infty \tau_{u_1}\; exp\left(-\frac{\tau_{u_1}}{\bar{\bar{G}}_{f_{\tau_1}}}\bar{\bar{\xi}}_v\right)\; d\bar{\bar{\xi}}_v, \tag{3.38}$$

$$G_{f_{\tau_2}} = \int_0^\infty \tau_{u_2}\; exp\left(-\frac{\tau_{u_2}}{\bar{\bar{G}}_{f_{\tau_2}}}\bar{\bar{\xi}}_w\right)\; d\bar{\bar{\xi}}_w. \tag{3.39}$$

3.3.3 Solution of the boundary value problem

The solution of the boundary value problem is sought by solving the following set of equations

$$\boldsymbol{r} = \mathbb{A}_{e=1}^{N_{el}} \left(\boldsymbol{f}^{(e),int} - \boldsymbol{f}^{ext} \right) = \boldsymbol{0}, \tag{3.40}$$

$$\boldsymbol{h}^e = \int_0^{l_e} \bar{\boldsymbol{G}}^T \boldsymbol{\sigma} dx + \boldsymbol{t} = 0, \quad \forall e \in [1, N_{el}^e], \tag{3.41}$$

where $\mathbb{A}_{e=1}^{N_{el}}$ is the finite element assembly over N_{el} finite elements, $\boldsymbol{f}^{(e),int} = \int_0^{l_e} \boldsymbol{B}^T \boldsymbol{\sigma} dx$ is the vector of internal forces obtained from the internal stress resultants, $\boldsymbol{\sigma} = [N \ V \ W \ M_x \ M_y \ M_z]^T$, while the enhanced part $\boldsymbol{h}^e = \boldsymbol{0}$ is added for every element with an active failure mode, which satisfies the yield condition given in Eqs. (3.31)-(3.33). From Eq. (3.41), it follows that the traction vector at the discontinuity is expressed as

$$\boldsymbol{t} = -\int_0^{l_e} \bar{\boldsymbol{G}}^T \boldsymbol{\sigma} dx, \tag{3.42}$$

where $\bar{\boldsymbol{G}}$ denotes the regular part of the G operator. For details on the model implementation and computational procedure see [125, 124, 122, 88].

Chapter 4

Investigation of identifiability of material parameters of reinforced concrete

In this chapter, Bayesian approach is employed for solving the stochastic inverse problem, as described in Chapter 2, to estimate unknown fracture and bond parameters of a damage model for reinforced concrete introduced in Section 3.2. The parameters of interest are identified with the help of observations from tensile tests on concrete tie beams with embedded reinforcement bars and virtual experiments, in the absence of available data. Moreover, the issue of identifiability of the target parameters is discussed. Namely, a particular measured response is usually not equally sensitive with respect to all target parameters. Hence, the aim is to identify the optimal experiments for estimation of a particular uncertain parameter, from the point of view of minimising the discrepancy between the computed and observed quantities of interest and the ease of implementation in a testing facility. Computationally efficient sequential Gauss-Markov-Kálmán filter based on functional approximations, described in Section 2.5.1, is adopted for solving the stochastic inverse problem. Quantities in the filtering equation are expressed in a compact manner by PCE of order 3. As the update step is equal to the loading step, which is rather small, Bayesian update is based on a linear approximation of the CE. Numerical simulations are carried out by the computer program *FEAP - Finite Element Analysis Program* [171], with a sample size of 1000.

4.1 Experimental setup

Tensile test provides information about the strength and toughness of a material as well as the final crack pattern, which makes it an obvious choice for the estimation of parameters governing fracture and bond-slip in reinforced concrete. The considered experiments were carried out by Farra [45] on concrete ties of dimensions $1150 \times 100 \times 100\ mm^3$, cast with different mixtures of concrete and different types and cross-sections of reinforcement bars embedded in the middle of the specimen.

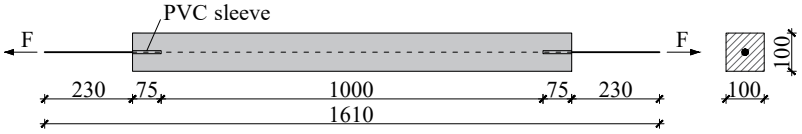

Figure 4.1: Experimental setup of a tension test and geometry of the considered specimen in $[mm]$

Fig. 4.1 shows the experimental setup of a concrete tie subjected to a tensile test. The experiment is carried out under force control. The applied force is then translated into its displacement counterpart, taken as the average of the values registered by two inductive sensors placed on the opposite sides of the specimen, 500 mm from the midspan. The traction force is introduced into the specimen at the ends of the reinforcement bar at the extension which is not covered by concrete [45]. In order to minimise the effects of stress concentration, the steel bar is unbonded and enveloped by a plastic sleeve in the length of 75 mm measured from the edge of the specimen, as shown in Fig. 4.1. For the purpose of numerical modelling, it is assumed that the whole bar is bonded with concrete, but the bond is considerably weaker at the ends to mimic the effects of the PVC sleeve.

Experiments are repeated three times for each particular configuration of materials and geometry. Here we consider the case S32-20, consisting of concrete of a class S32, where "S" indicates the sulphate-resisting cement, and the percentage of reinforcement of 3.14%, corresponding to a steel bar of diameter 20 mm. The type of steel used in the experiments is the high-adherence structural steel denoted as S500.

The global behaviour of the RC beams is captured by means of a force-displacement (or a stress-deformation) diagram. The curves obtained by experiments on the specimens of configuration S32-20 are shown in Fig. 4.2(a).

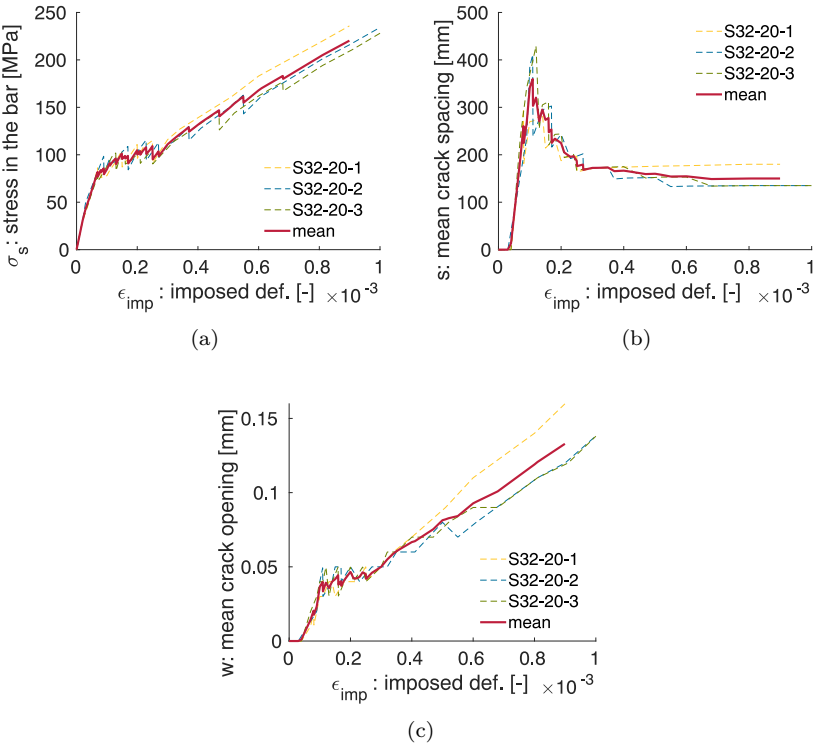

Figure 4.2: Experimental results [45]: a) steel stress-imposed deformation diagram; b) mean crack spacing; c) mean crack opening

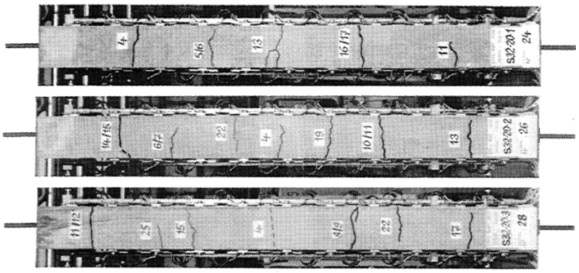

Figure 4.3: Crack patterns from three experiments on beams of class S32-20 [45]

In addition, the evolution of quantities describing the cracking of concrete, i.e. the crack spacing and opening, is analysed and reported. The average of the mean crack spacing and opening from the three tests on the RC beams of configuration S32-20 are plotted in Fig. 4.2(b)–4.2(c), whereas the particular crack patterns obtained in each of the tests are shown in Fig. 4.3.

4.2 Generalisation of the enriched finite element to account for alternative load applications

To be able to computationally reproduce the above described tensile experiment, the formulation of a finite element with embedded discontinuity and bond-slip requires certain modifications. Namely, according to the formulation of the numerical model given in Section 3.2.4, a direct application of the load onto the reinforcement bar is not feasible, as the BVP is formulated under the assumption that the load is applied solely through concrete. Hence, an utilitary truss bar element is defined. The latter is connected to a 2D solid CST element and transforms the truss bar displacements into the solid element conjugates.

Firstly, vector of truss bar displacements is defined as

$$\bar{\boldsymbol{d}} = \begin{bmatrix} d^s_{x,I} \\ d^s_{x,II} \end{bmatrix}, \tag{4.1}$$

where $d^s_{x,I}$ and $d^s_{x,II}$ denote the axial displacements of the bar at the left and right node, respectively.

Displacements of a 2D solid CST element which are conjugate to the above defined truss bar displacements are collected in a vector $\boldsymbol{d}$, which can be written as

$$\boldsymbol{d} = \begin{bmatrix} d^c_{x,I} \\ \alpha^{bs}_{x,I} \\ d^c_{x,II} \\ \alpha^{bs}_{x,II} \end{bmatrix}, \tag{4.2}$$

where superscripts c and bs refer to concrete displacements and bond-slip at the concrete-steel interface, respectively. The truss bar displacements are

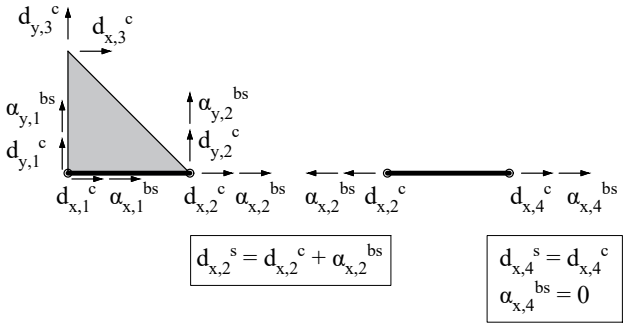

Figure 4.4: Coupling between the displacement field of a solid CST element and a truss bar element

further transformed into the CST solid ones by means of a transformation matrix $\mathbf{T}$. Taking into account Eq. (3.16), which states that the displacements of the steel bar are obtained as a sum of the displacements of concrete and bond-slip, such transformation matrix takes the form of

$$\mathbf{T} = \begin{bmatrix} 1 & 1 & 0 & 0 \\ 0 & 0 & 1 & 1 \end{bmatrix}. \tag{4.3}$$

Having defined the transformation matrix, the element stiffness matrix and internal force vector can be transformed from the truss bar quantities into their solid element conjugates in the following manner

$$\mathbf{k} = \mathbf{T}^T \bar{\mathbf{k}} \mathbf{T}, \tag{4.4}$$

$$\boldsymbol{f} = \mathbf{T}^T \bar{\boldsymbol{f}}, \tag{4.5}$$

where $\bar{\mathbf{k}} = \int_{\Omega^e} \mathbf{B}^{s,T} \mathbf{C} \mathbf{B}^s d\Omega^e$ and $\bar{\boldsymbol{f}} = \int_{\Omega^e} \mathbf{B}^{s,T} \sigma^s A_s dx$ denote the stiffness matrix and the internal force vector of the truss bar, respectively.

4.3 Prior description of the material parameters

The choice of uncertain parameters pertains to material parameters governing fracture in concrete: hardening modulus K_h and elastic limit stress $\bar{\sigma}_f$ (*hardening*); ultimate stress $\bar{\bar{\sigma}}_f$ and fracture energy $\bar{\bar{G}}_f$ (*softening*), as well as parameters governing the behaviour of the bond: critical bond stress τ_y

(*bond-slip*). All the uncertain parameters are modelled as random variables, which implies having homogenised properties within a particular composite constituent. In order to ensure that the prior values of parameters are positive-definite, they are assumed to follow the lognormal probability distribution. Moreover, the prior description results from preliminary numerical studies that provide the closest possible estimates, in the lack of experts' proposed values. The prior mean values and corresponding standard deviations are summarised in Table 4.1. Note that the standard deviation is assumed as 10% of the mean value, which implies a rather narrow prior. Due to the fact that the mechanical model is highly nonlinear and sensitive with respect to its input parameters, which are modelled as uncorrelated random variables, a significant variability in inputs can lead to convergence issues.

Table 4.1: Prior probabilistic description: mean value and standard deviation of uncertain material parameters

Property	Mean	Standard deviation
$\bar{\sigma}_f$	1.100 (MPa)	0.110 (MPa)
K_h	45000.000 (MPa)	4500.000 (MPa)
$\bar{\bar{\sigma}}_f$	2.200 (MPa)	0.220 (MPa)
$\bar{\bar{G}}_f$	0.220 (N/mm)	0.022 (N/mm)
τ_y	3.000 (MPa)	0.300 (MPa)

Samples of the above defined prior distributions are drawn by a Monte Carlo simulation. A total of 1000 samples are generated and employed to carry out the numerical predictions.

Parameters which do not influence fracture in concrete and bond-slip, e.g. the elastic properties of concrete and steel: bulk K and shear G moduli of concrete and elastic modulus E_s of steel, are considered as known. The elastic bond modulus K_{bs} is introduced as a parameter which influences stability and convergence of the solution and thus it is of no particular interest for identification. In the regions where the steel bar in enveloped by a plastic sleeve, the bond modulus K_{bs} is replaced by the modulus K_{PVC}, the value of which is smaller compared to the value of K_{bs} in order to reflect the weakened bond. The reinforcement bar has a constant cross-section A_s, with bonded area defined as A_{bs}. The areas are here expressed per unit length of the beam thickness. Values of the remaining, deterministic parameters are given in Table 4.2.

Table 4.2: Values of deterministic parameters

Property	Value
K	19111.110 (MPa)
G	14333.330 (MPa)
E_s	200000.000 (MPa)
A_s	3.142 (mm^2/mm')
K_{bs}	100.000 (MPa/mm')
K_{PVC}	80.000 (MPa/mm')
A_{bs}	0.628 (mm/mm')

4.4 Uncertainty quantification

Repeated numerical simulations with different combinations of input parameters result in an ensemble of response curves. For each particular response, prior statistics can be extracted, i.e. the mean curve and confidence bounds (95% quantiles). It should be noted that numerical simulations are not performed until complete fracture of the specimen due to the fact that the estimates of target parameters can be obtained with satisfactory accuracy even after registering only two successive macro-cracks. Fig. 4.5 depicts the 95% confidence bounds of the stress distribution along the specimen, computed with prior description of uncertain material parameters. In the same figure, one can also observe curves of some selected realisations.

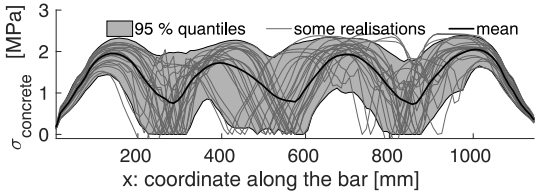

(a)

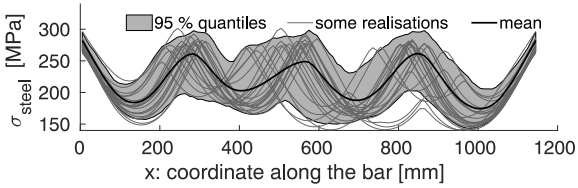

(b)

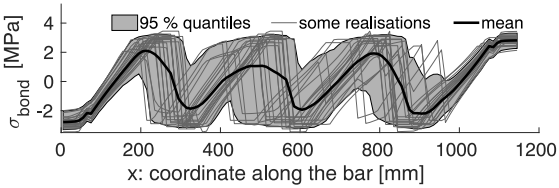

(c)

Figure 4.5: Prior quantiles and mean of stresses in: a) concrete; b) steel; c) bond

From Fig. 4.3, it can be observed that repeated experiments with the same material configuration and geometry can lead to significantly different crack patterns. Due to the mechanism of stress transfer in a tensile test, the first crack usually appears approximately in the middle of the beam and successive cracks follow at the midspan of the cracked sections. Fig. 4.6 shows the distribution of both plastic and total bond-slip in terms of 95% quantiles as well as some selected realisations. The largest values of bond-slip coincide with the locations of macroscopic cracks.

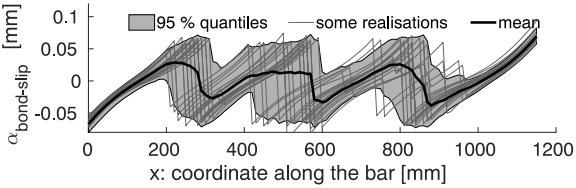

(a)

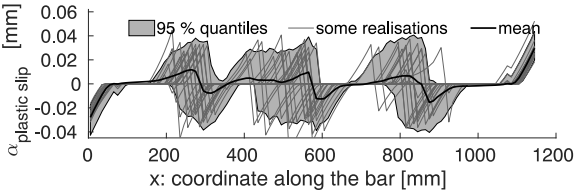

(b)

Figure 4.6: Prior quantiles and mean of: a) bond-slip; b) plastic slip

The experimental stress-deformation curves plotted in Fig. 4.2(a) are em-

ployed for parameter estimation. From the latter, one can observe that the measured curves significantly vary with every successive crack. In order to incorporate the scattering of the results within the population of beams, the discrete points on the mean stress-deformation curve in Fig. 4.2(a) are considered as observations. The prior statistics within the considered range is plotted in Fig. 4.7.

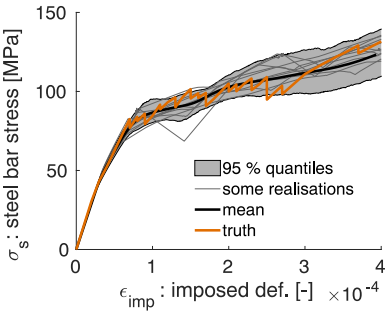

Figure 4.7: Prior statistics of the global stress-deformation curve and its experimental (true) curve

4.5 Estimation of target parameters from the stress-deformation curve

Upon reaching the elasticity limit, $\bar{\sigma}_f$, behaviour of the specimen enters the inelastic regime. The influence of the parameters governing hardening and softening thereby becomes more prominent. In total, there are four parameters that need to be identified, namely the hardening modulus K_h, limit stress $\bar{\sigma}_f$, ultimate stress $\bar{\bar{\sigma}}_f$ and fracture energy $\bar{\bar{G}}_f$. According to global sensitivity analysis, the results of which are plotted in Fig. 4.8 in terms of partial variances and first order Sobol indices, it can be observed that these parameters have a significant impact on the selected response.

The magnitude of the influence of a particular parameter changes over time, as the material undergoes different stages of its behaviour: elasticity, hardening and softening.

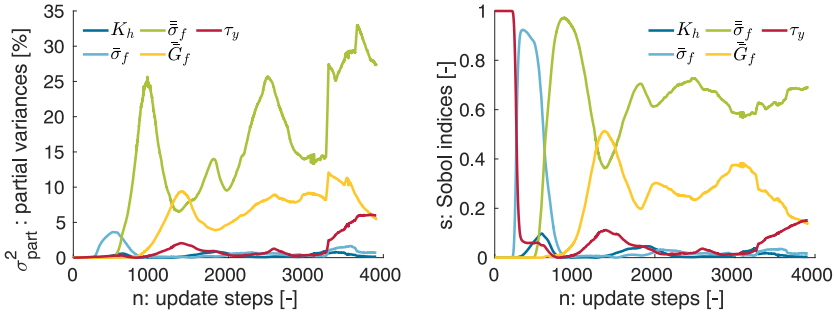

Figure 4.8: Global sensitivity with respect to stress-deformation evolution: a) partial variances; b) first order Sobol indices

4.5.1 Parameters related to hardening of concrete

The first parameter to be identified is the concrete limit stress, which implies the beginning of the hardening phase. Update is initiated immediately upon gathering the first portion of data. The estimation is performed sequentially using the PCE-based GMKF and after each discrete update step a new posterior is obtained. The measurement error is assumed to be independent at each update step and modelled with the Gaussian distribution, i.e. $\varepsilon(\eta) \sim \mathcal{N}(0, C_\varepsilon)$, with zero-mean and covariance C_ε. Its standard deviations are defined as 1% of the corresponding observed values. Modelling errors are not considered in this study.

Recalling the evolution of partial variances and first order Sobol indices shown in Fig. 4.8, one can deduce that the hardening phase takes place after about 100 loading steps, when the limit stress starts contributing to the variability of the output. Around 300th step, the information gain from the data starts to significantly alter the prior probability density of the limit stress, which soon reaches its converged posterior at update step 350. While the update is performed at each update step coinciding with a particular loading step, only a selected few, at which the most significant changes in posterior PDF are observed, are plotted in Fig. 4.9(a). As shown in Fig. 4.9(b), uncertainty is visibly reduced, reflecting the improved confidence in the actual value of the limit stress.

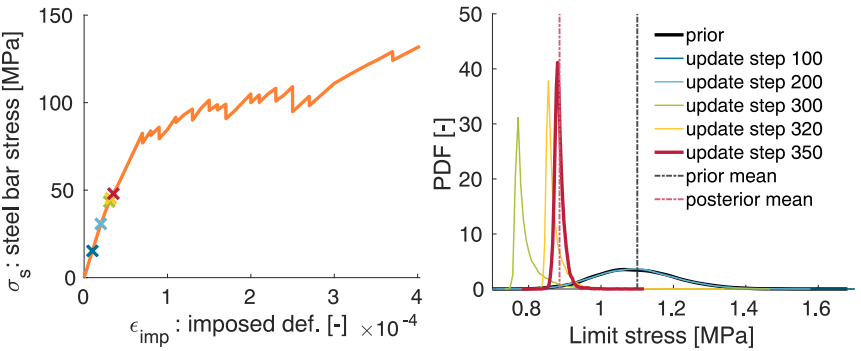

Figure 4.9: Sequential update of the limit stress: a) update steps imposed on stress-deformation ($\sigma_s - \bar{\epsilon}$) curve; b) prior and posterior probability density functions

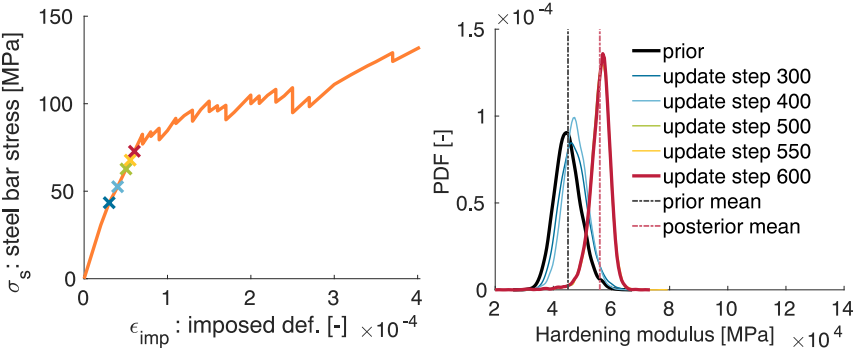

Figure 4.10: Sequential update of the hardening modulus: a) update steps imposed on stress-deformation ($\sigma_s - \bar{\epsilon}$) curve; b) prior and posterior probability density functions

The hardening modulus starts contributing to the mechanical response of concrete around the update step 300, which coincides with an increase in its partial variance and first order Sobol index depicted in Fig. 4.8. Its posterior densities obtained at update steps plotted in Fig. 4.10(a) are shown in

Fig. 4.10(b). From the latter, one can observe that by gaining new information from the data, the posterior PDF continues to change until it finally settles into a stationary distribution around 600th update step.

4.5.2 Parameters related to softening of concrete

A further increase in loading leads to more significant damage in concrete. After around 600 update steps, the posterior PDF of the ultimate stress starts to look significantly narrower, as shown in Fig. 4.11(b), which implies the initiation of crack propagation accompanied by strain-softening. Observations registered in this phase of the experiment provide the most relevant information for identifying the ultimate stress. The converged form of the PDF is reached after 800 update steps and its shape is plotted in Fig. 4.11(b).

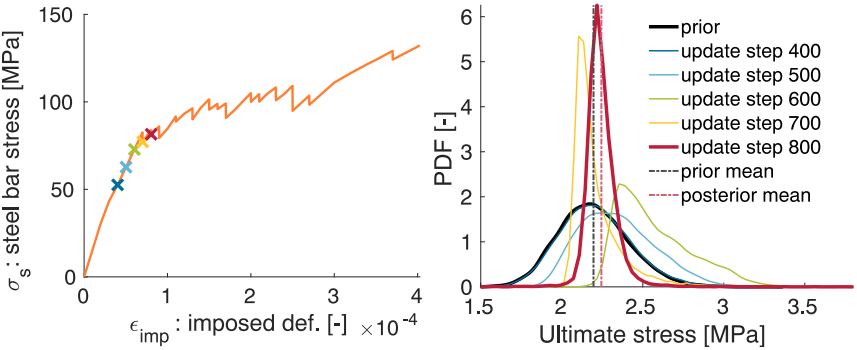

Figure 4.11: Sequential update of the ultimate stress: a) update steps imposed on stress-deformation ($\sigma_s - \bar{\epsilon}$) curve; b) prior and posterior probability density functions

As shown in Fig. 4.8, the influence of the fracture energy becomes more significant around 900th update step, which indicates the presence of softening in particular regions of the specimen. The stationary posterior PDF of the fracture energy is plotted in Fig. 4.12(b). The effect of shrinking of the variance is not as evident as for some previously discussed parameters, the reason being that the chosen quantity of interest does not contain enough

information about this parameter. This issue and possible improvements are addressed in Section 4.6.

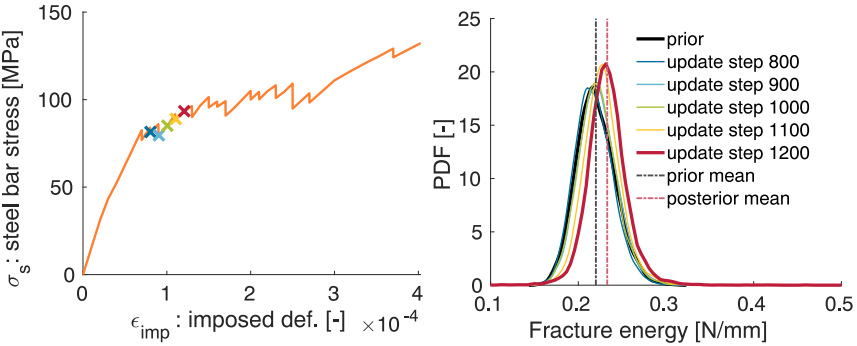

Figure 4.12: Sequential update of the fracture energy: a) update steps imposed on stress-deformation ($\sigma_s - \bar{\epsilon}$) curve; b) prior and posterior probability density functions

4.5.3 Bond properties

The main parameter governing the behaviour at the concrete-steel interface is the critical bond stress τ_y, the significance of which is related to cracking in concrete. Namely, upon appearance of a macro-crack in concrete, the bond governs the stress redistribution between concrete and steel, which subsequently induces the bond-slip at the concrete-steel interface. When bond stress reaches the critical value, τ_y, the relative sliding of the reinforcement bar with respect to surrounding concrete can no longer be considered elastic, but rather an irreversible process, quantified in terms of a permanent (plastic) slip α_{bs}^{pl}. According to Fig. 4.8, critical bond stress has the greatest influence on the response in the first 200 steps. Hence, its estimation is initiated immediately upon gathering a first portion of observational data. However, in theory, the behaviour of the composite in this phase should be purely elastic and the reinforcement bar should still be perfectly bonded to the surrounding concrete.

By inspecting the sequential update of the critical bond stress shown in Fig. 4.13, one can conclude that the posterior sample set is not a subset of prior and the posterior mean value is unusually small in comparison to

the values from the literature [45]. That could indicate that the critical bond stress is not identifiable from the chosen QoI and subsequently, the experiment is not optimal for the estimation of this parameter.

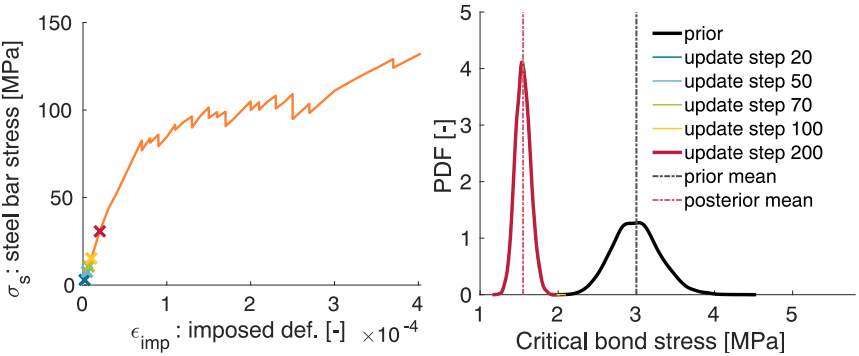

Figure 4.13: Sequential update of the critical bond stress: a) update steps imposed on stress-deformation ($\sigma_s - \bar{\epsilon}$) curve; b) prior and posterior probability density functions

Bond-slip is taking place in the vicinity of macro-cracks in concrete and hence, in order to accurately infer the related mechanical properties, one needs to consider not only global observations (e.g. the global stress-deformation curve), but the local effects as well (e.g. crack opening of a particular crack). This idea is further elaborated in the successive section, which investigates whether the addition of observations reflecting the local effects can improve the estimates of the critical bond stress.

Posterior estimates of the uncertain material parameters are validated by comparing the experimental stress-deformation curve with the 95% quantiles of the posterior predictive obtained by propagating the estimated material parameters through the polynomial surrogate model. Fig. 4.14 illustrates these quantities within the range of deformation considered for the estimation, i.e. $0 < \bar{\epsilon} \leq 1.2 \times 10^{-4}$. As shown in Fig. 4.14, the mean stress-deformation curve coincides with the experimental one, which further means that the estimated parameters are reliable. The 95% confidence region is considerably narrower compared to the one plotted in Fig. 4.7, obtained by propagating the prior uncertainty. Note that the model can predict well the

behaviour up to opening of the first two macroscopic cracks, whereas the predictions of the further cracks are considerably less accurate.

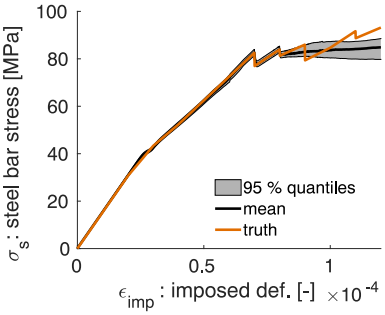

Figure 4.14: Posterior statistics of the global stress-deformation curve and its experimental (true) curve

4.6 Improved estimates of target parameters by including additional quantities of interest

This section explores whether the parameter identifiability can be improved and discrepancies between the actual observations and model output reduced by combining several quantities of interest which are significant for the concerned problem. For that purpose, the inclusion of the following QoIs is proposed: the total dissipation, number of cracks and crack opening. Note that all considered QoIs have different units. In the context of the Kálmán filter, this implies that QoIs of higher magnitudes are given preference when calculating the posterior estimates. To alleviate this issue and ensure that all observation are given the same weight, everything is expressed in terms of energy-like quantities, i.e. instead of stress σ_s, the term σ_s/E_s, instead of number of cracks N_c, the term $N_c G_f/l_{\Gamma_s}$ and instead the crack opening α_c, the term $E_s\alpha_c^2 l_b/V_b$, where l_b and V_b denote the length and volume of the beam, respectively. In this manner, all QoIs have the unit of energy density, i.e. N/mm^2, and their magnitudes are of the same order.

The criteria for choosing the relevant observations are twofold. Firstly, the observations should be easily generated in testing facilities and secondly, they should be meaningful considering the nature of the target parameters (e.g. local and global properties). In the following sections, the choice of

a particular QoI is discussed and its influence on the parameter inference is investigated.

4.6.1 Inclusion of the total dissipation

The concept of stored and dissipated energy is essential for the accurate representation of the inelastic material behaviour. It is closely related to the irreversible deformation taking place in concrete and at the concrete-steel interface, ultimately leading to material failure. As already described in Section 3.2, inelastic behaviour of concrete is accompanied by the volume and surface dissipation due to nucleation and propagation of the cracks in the fracture process zone. In addition to dissipative mechanisms in concrete, at the locations of the macroscopic cracks, the dissipation of energy due to bond-slip takes place. Computation of their contributions is straightforward by employing Eq. (3.11) and Eq. (3.14). This task, however, becomes infeasible in practice, where typically only the total dissipation can be attained.

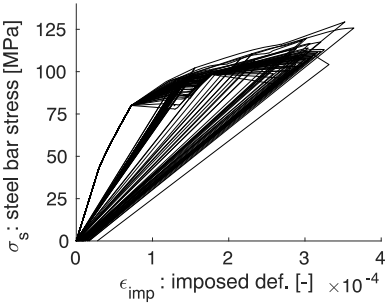

Figure 4.15: Loading-unloading cycles of the repeated virtual experiments

The easiest approach to measure the total dissipation in a system is to design an experiment which consists of loading the specimen under the displacement control up to the opening of the first macroscopic crack and unloading it immediately afterwards. The total dissipation is thereby regarded as the area between the loading and unloading slopes. In the virtual experiment introduced herein, the loading-unloading cycle is repeated once more upon appearance of the second macroscopic crack. Subsequent cracks are distinctive property of each individual beam and as such are not relevant for identification of the properties characteristic for the whole population of beams. The

criteria employed for detection of a macroscopic crack in numerical simulations is the amount of dissipated energy due to damage in concrete taking the value larger than or equal to 95 % of the fracture energy. The resulting loading-unloading cycles for a particular realisation are given in Fig. 4.15.

The virtual simulations are computed by perturbing the value of fracture energy, whereas the values of the remaining parameters are fixed at their mean values, as given in Table 4.1.

Bayesian inference of the uncertain parameters is performed separately for each of the 50 realisations of the virtual experiment. Afterwards, the posterior distributions resulting from the update using a particular virtual experiment are summed up and divided by the number of samples in a Monte Carlo fashion [71]. In this manner, the final posteriror PDFs, shown in Fig. 4.16, have a larger variance and thereby capture not only the epistemic uncertainty due to lack of knowledge about the uncertain properties, but the aleatoric uncertainty inherent to the material as well.

Note that, as it is essentially a Monte Carlo method, it is meaningful only if there are enough repetitions of the experiment. Otherwise, it is more suitable to use the mean response, as it has been done in Section 4.5, where only 3 stress-deformation curves were available. The observed value of dissipation is introduced into the update once the sequential update using the observations of the stress-deformation curve is completed. Hence, the last registered posteriors from Section 4.5 are further altered by taking into account the observations of dissipation. For the sake of simplicity and consistency with the rest of the results, only the mean curve will be considered for the identification shown below.

Dissipation is closely related to the fracture energy of concrete and subsequently, to its ultimate stress. These two parameters are here considered uncorrelated, but they are indeed dependent through Eq. (3.12). As shown in Figs. 4.17(a)–4.17(c), parameters that are not activated during the softening regime, i.e. the hardening modulus, limit stress and critical bond stress, show no significant alteration of the posterior PDFs after the addition of the observed dissipation.

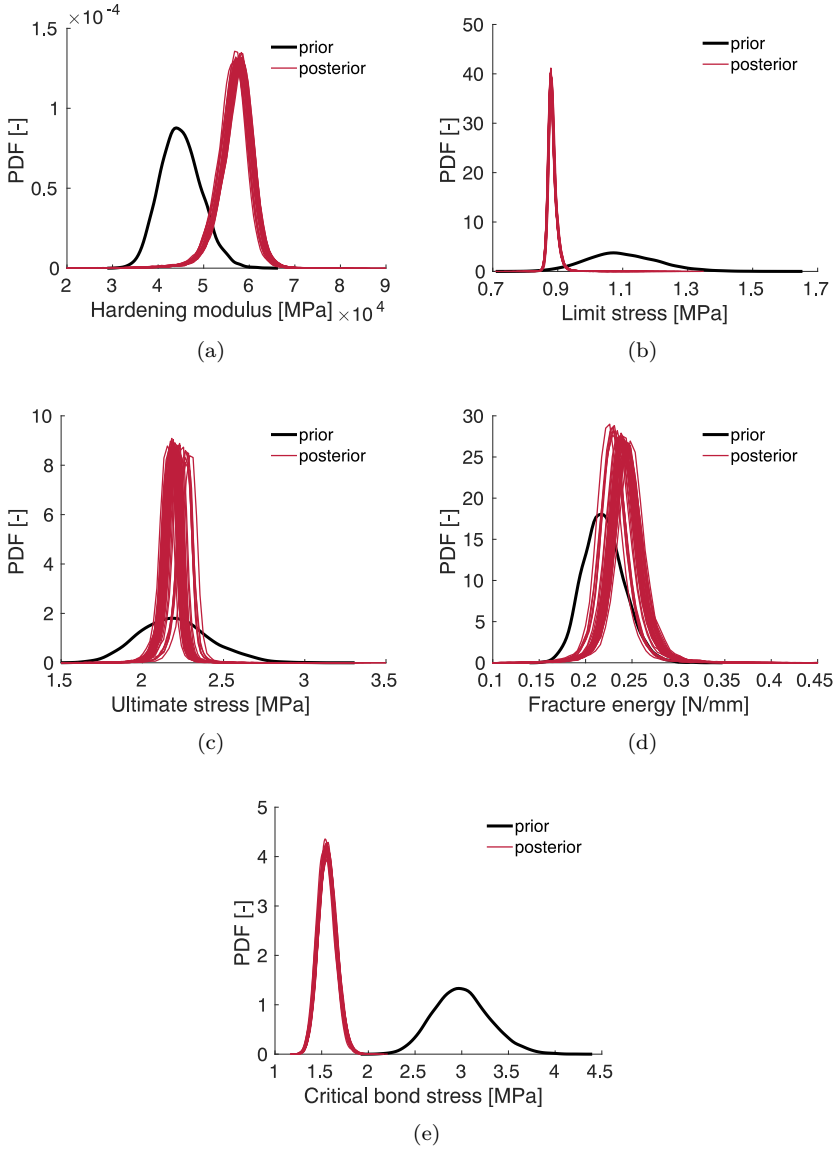

Figure 4.16: Prior and posterior (Monte Carlo) probability density functions after inclusion of the observed dissipation (D) for the: a) hardening modulus; b) limit stress; c) ultimate stress; d) fracture energy; e) critical bond stress

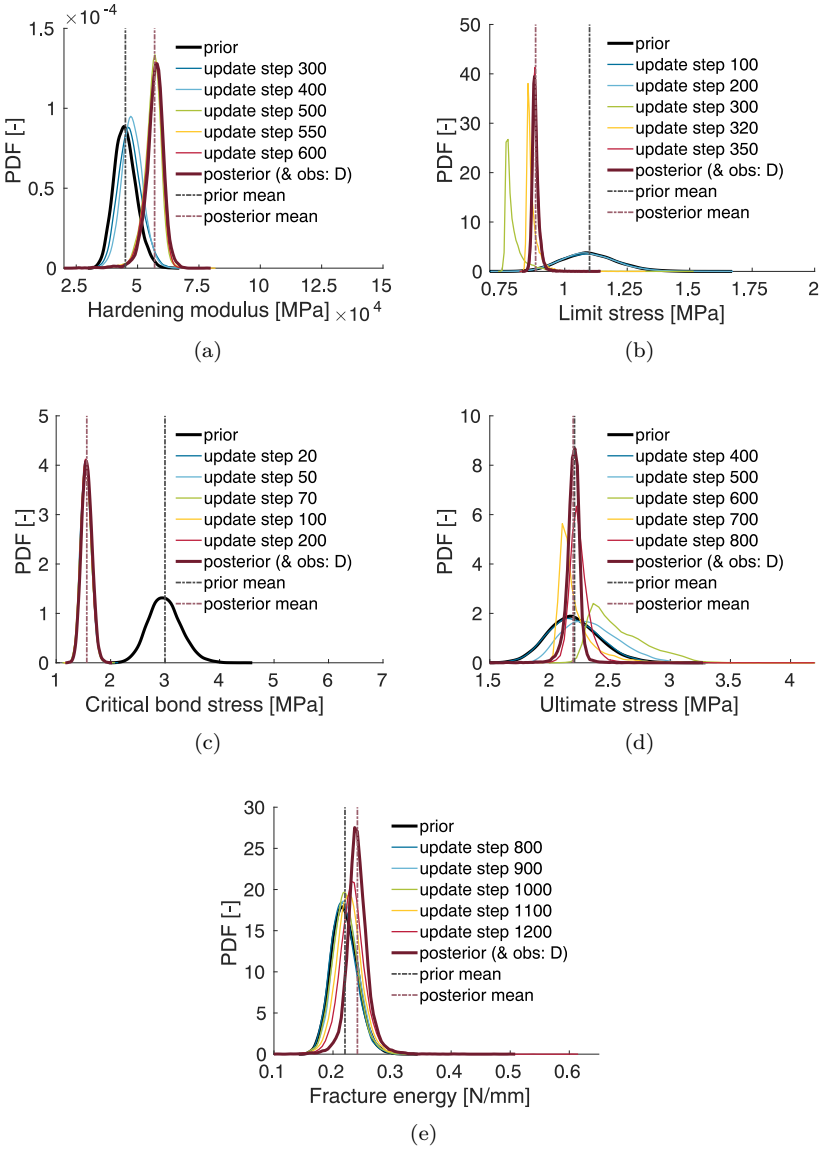

Figure 4.17: Prior and posterior probability density functions after inclusion of the observed dissipation (D) for the: a) hardening modulus; b) limit stress; c) critical bond stress; d) ultimate stress; e) fracture energy

On the other hand, the posterior PDFs of the fracture energy and ultimate stress, plotted in Figs. 4.17(d)–4.17(e), are visibly altered. The latter leads to significantly reduced discrepancies between the model and experimental results (see Table 4.3 for the summary of the model outputs), while the stress-deformation curve is still well approximated (see Fig. 4.24). Nevertheless, the cracking quantities related to bond, e.g. the total number of cracks and crack opening, still quite differ from the measured values and hence, for the reliable estimation of the bond properties one needs to include additional QoIs.

4.6.2 Inclusion of the total dissipation & number of cracks

The number of cracks is directly related to the strength of the bond, with stronger bond leading to a more favourable crack pattern in terms of a larger number of fine, narrow cracks. Thus, this section explores whether the addition of the observed number of cracks can bring more information about the target parameter related to bond.

During tensile test introduced in Section 4.1, an average of 5 cracks opens up to deformation of 4×10^{-4}, which is the range considered in the numerical simulations. Similarly to the previous case, when dissipation was included as an additional QoI, the addition of the number of cracks causes no obvious changes in the posterior PDFs of the hardening modulus and limit stress, see Figs. 4.18(a)–4.18(b).

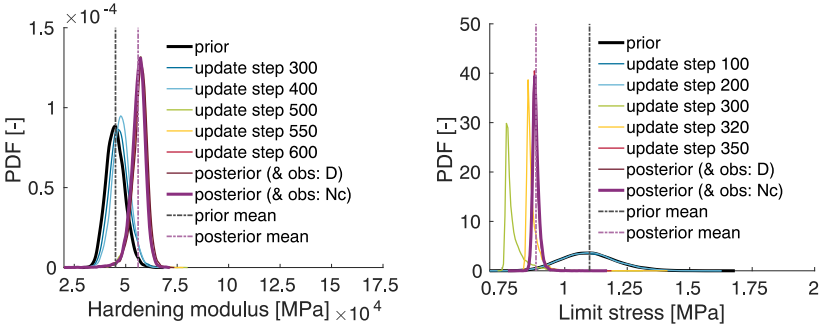

(a) (b)

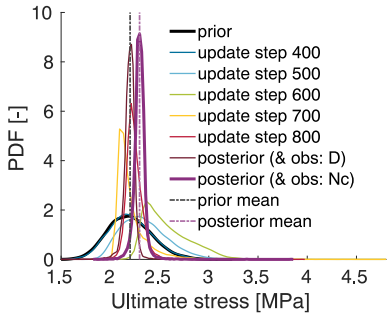

(c)

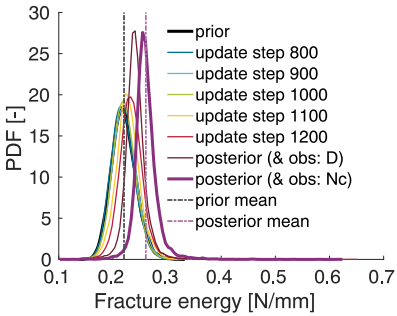

(d)

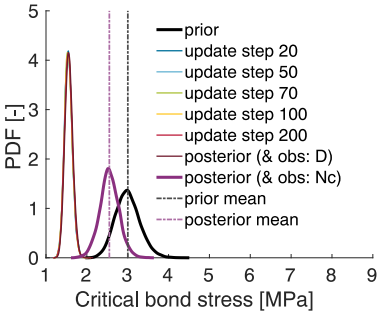

(e)

Figure 4.18: Prior and posterior probability density functions after inclusion of the observed number of cracks (N_c) for the: a) hardening modulus; b) limit stress; c) ultimate stress; d) fracture energy; e) critical bond stress

On the other hand, changes in the posterior PDFs of the ultimate stress, fracture energy and critical bond stress, shown in Figs. 4.18(c)–4.18(e), are significant. From the summary in Table 4.3 and Fig. 4.24, one can deduce the following: stress-deformation curve is still well approximated, as well as dissipation, although the discrepancy between its computed and observed value is slightly higher. The number of cracks, in spite of expectations, cannot be well approximated, but the number is closer to the observed value in comparison to the case when just the stress-deformation curve is considered as a QoI.

4.6.3 Inclusion of the total dissipation & crack opening

Crack opening of a particular crack is a local property and as such, it is related to the bond-slip taking place in the vicinity of the macroscopic cracks. This section explores whether the inclusion of the observed crack opening as an additional QoI may be more suitable for estimation of the target properties of the bond compared to previously considered cases. For that purpose, the observed value of the opening of the first macro-crack at the time instance corresponding to the opening of the successive macro-crack, taken from [45], is considered. The latter is added as an additional observation that changes the probabilistic description given in Section 4.6.1 and Fig. 4.19.

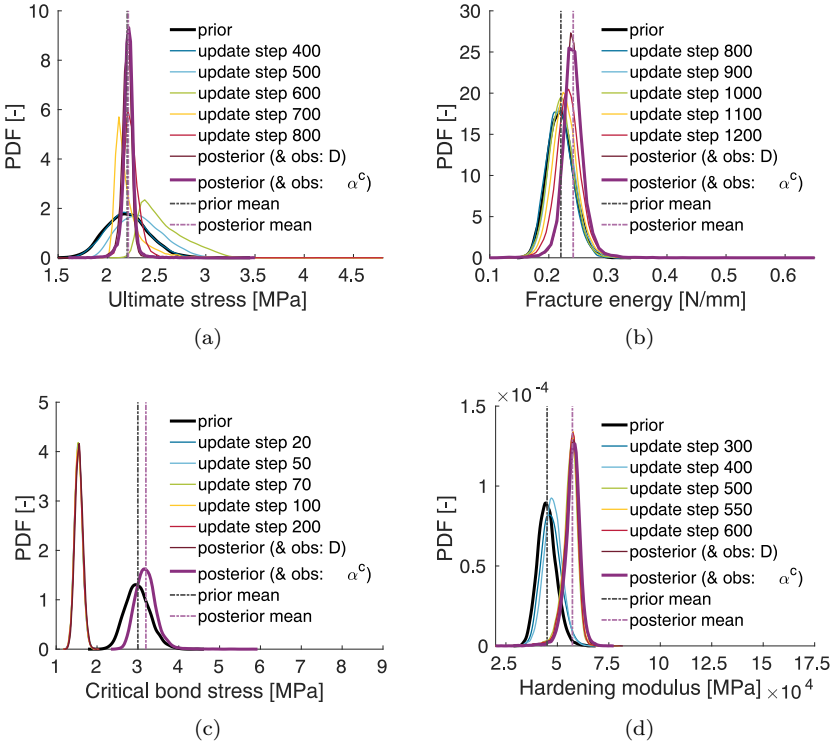

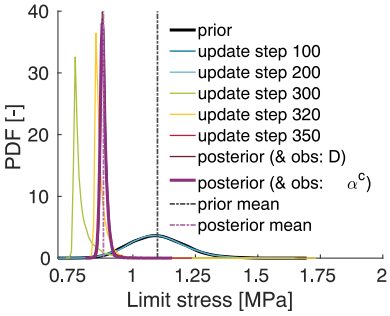

(e)

Figure 4.19: Prior and posterior probability density functions after inclusion of the observed crack opening (α^c) for the: a) ultimate stress; b) fracture energy; c) critical bond stress; d) hardening modulus; e) limit stress

From the results reported in Table 4.3, it is evident that by including the crack opening as a QoI, the discrepancy between its computed and observed value is significantly decreased. On contrary, the estimate of dissipation is the most unfavourable considering all the cases investigated so far. Furthermore, the number of cracks is now much closer to the experimental value and much higher than in any other considered case, which also holds for the value of the critical bond stress. This result affirms the fact that stronger bond leads to higher number of cracks with smaller crack openings.

4.6.4 Inclusion of the total dissipation & number of cracks & crack opening

In this case, all of the above considered QoIs, i.e. the stress-deformation curve, total dissipation, number of cracks and crack opening of a particular macro-crack, are employed together in an attempt to further improve the posterior estimates. The new observations are added consecutively, which is reflected in the final posterior PDFs, the shape of which differs based on the order of the inclusion. The following subcases are considered: 1) $\sigma_s - \bar{\epsilon}$ & D & N_c & α^c; 2) $\sigma_s - \bar{\epsilon}$ & D & α^c & N_c, where the QoIs are listed in the order of inclusion.

The resulting posterior PDFs are given in Fig. 4.20 and Fig. 4.21 for the subcases 1) and 2), respectively. The posterior PDFs of the hardening mod-

ulus and limit stress are here excluded, as it is already proved in the sections above that they are not sensitive with respect to the newly added QoIs.

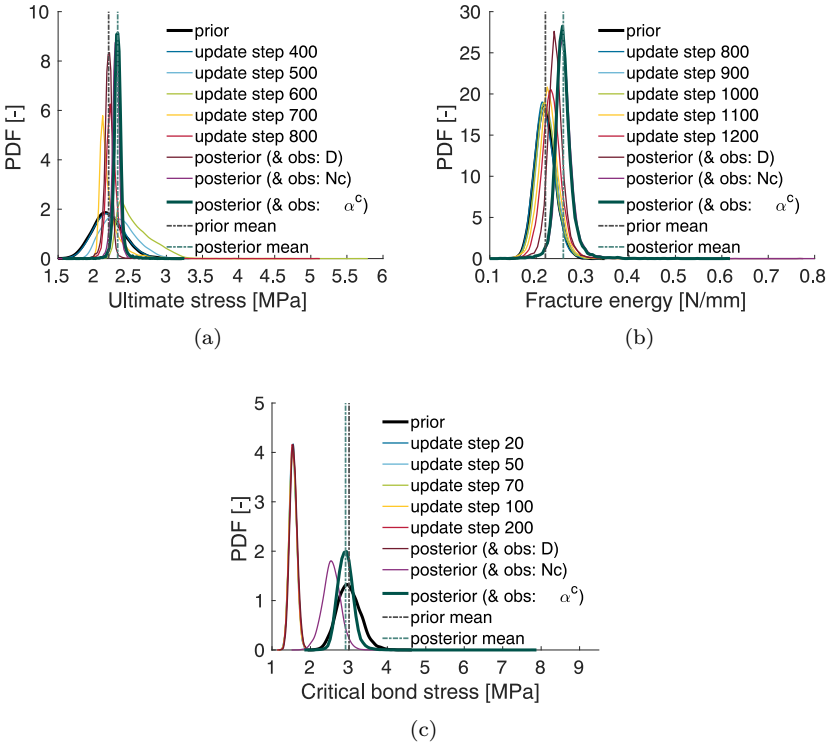

Figure 4.20: Prior and posterior probability density functions obtained by considering all QoIs ($\sigma_s - \bar{\epsilon}$ & D & N_c & α^c) for the: a) ultimate stress; b) fracture energy; c) critical bond stress

The assumption that the inclusion of all above considered QoIs yields the best possible estimates of the target parameters is proved to be wrong. Namely, from Table 4.3, one can deduce that both of the considered subcases fail to successfully approximate the crack opening. Its value is the closest to the observed value when the number of cracks is excluded from the list of QoIs. On the other hand, the value of dissipation is the best approximated when only the stress-deformation curve and the total dissipation are considered as QoIs.

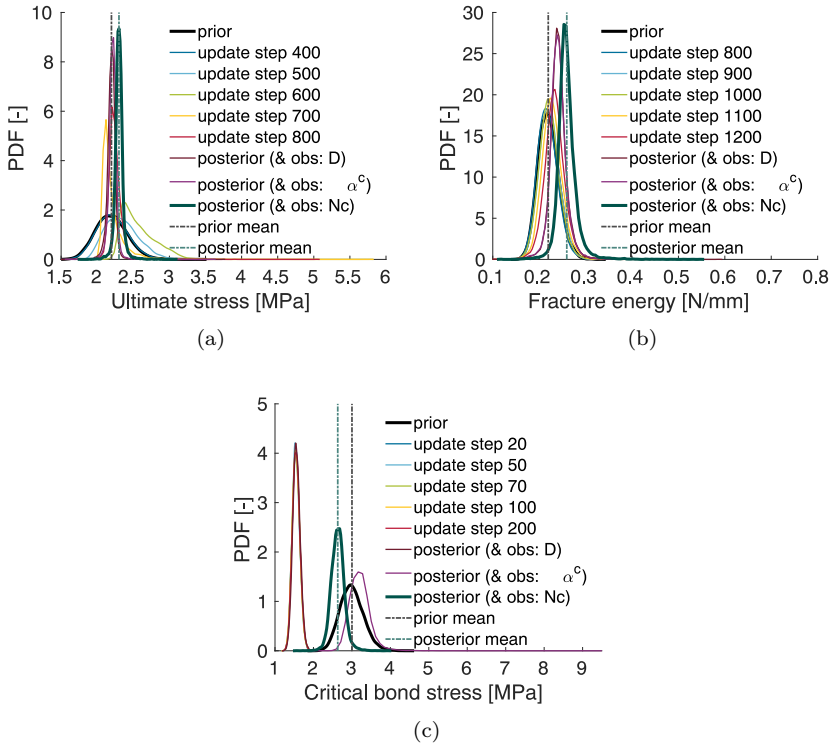

Figure 4.21: Prior and posterior probability density functions obtained by considering all QoIs ($\sigma_s - \bar{\epsilon}$ & D & α^c & N_c) for the: a) ultimate stress; b) fracture energy; c) critical bond stress

4.7 Validation of the results

The investigation of the influence of different quantities of interest to the outcome of Bayesian identification, results in the following conclusions:

- Stress-deformation curve shows sensitivity with respect to all target parameters. All the posterior PDFs show a considerable reduction in the uncertainty, with an exception of the fracture energy. Samples of the posterior PDF of the critical bond stress are not a subset of the prior and its posterior mean value is considerably smaller compared to

the values from the literature. This further leads to a smaller number of relatively wide cracks, which differs from the experiment. Thus, the posterior estimate of the critical bond stress is deemed as unreliable.

- Inclusion of the total dissipation does not change the posterior estimates of the hardening modulus, elasticity limit and critical bond stress, but improves the estimates of the ultimate stress and fracture energy. Discrepancy between the computed and observed value of dissipation is highly reduced and is the smallest overall.
- Inclusion of both the total dissipation and number of cracks does not significantly change the posterior estimates of the hardening modulus and elasticity limit, but has an influence on the estimates of parameters related to cracking: the ultimate stress, fracture energy and critical bond stress. The most significant is the change in the PDF of the critical bond stress, the posterior mean of which is now much larger.
- Inclusion of both the total dissipation and crack opening has no influence on the posterior of the hardening modulus and elasticity limit, but changes the posterior estimates of the ultimate stress, fracture energy and, in particular, critical bond stress. Addition of this QoI provides the best match in both the value of crack opening and number of cracks.
- Inclusion of all the considered QoIs, i.e. the total dissipation, number of cracks and crack opening, simultaneously, brings no meaningful improvement in the posterior estimates.

A summary of the resulting posterior densities of the target parameters (the hardening modulus, limit stress, ultimate stress, fracture energy and critical bond stress) obtained from the above considered cases is given in Fig. 4.22.

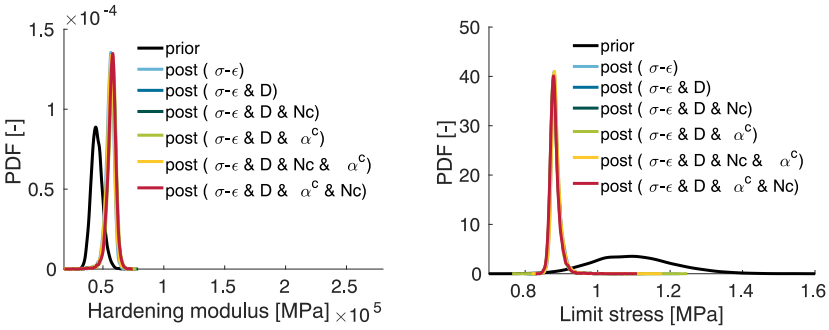

(a) (b)

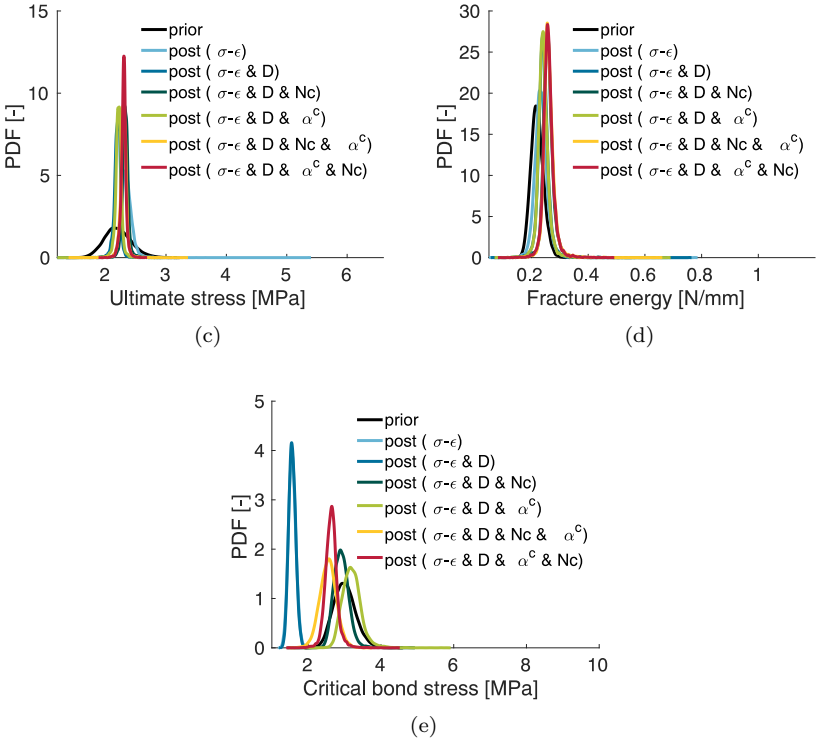

Figure 4.22: Overview of posterior probability density functions for the: a) hardening modulus; b) limit stress; c) ultimate stress; d) fracture energy; e) critical bond stress

In summary, one can visualise the inferred PDFs in a grid of plots shown in Fig. 4.23, where the univariate marginal distributions are plotted along the diagonal, whereas the off-diagonal plots correspond to bi-variate scatter plots, from which one can deduce the correlations between the pairs of parameters.

For validation purposes, realisations of the finite element solver are computed with the posterior mean values of target parameters obtained in each of the considered cases. The corresponding stress-deformation curves are plotted in Fig. 4.24, whereas the computed values of the remaining QoIs are reported in Table 4.3 and compared with their observed counterparts.

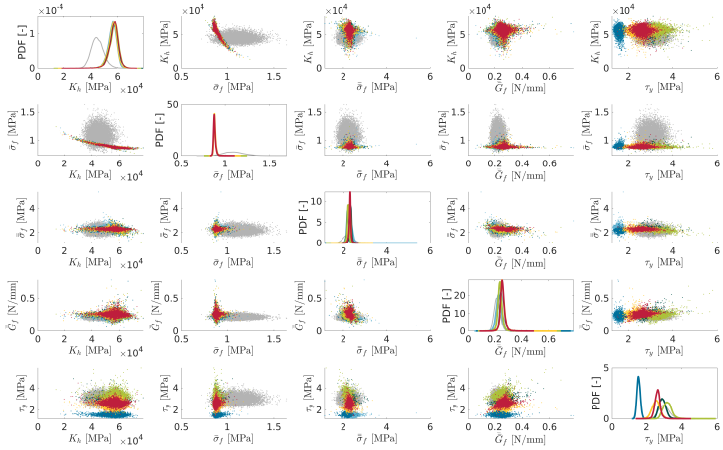

Figure 4.23: Marginal distributions and correlations for the considered QoIs: $(\sigma - \epsilon)$ shown in light blue, $(\sigma - \epsilon$ & $D)$ shown in dark blue, $(\sigma - \epsilon$ & D & $N_c)$ shown in dark green, $(\sigma - \epsilon$ & D & $\alpha^c)$ shown in light green, $(\sigma - \epsilon$ & D & N_c & $\alpha^c)$ shown in yellow, $(\sigma - \epsilon$ & D & α^c & $N_c)$ shown in red. Prior PDF and samples are shown in grey.

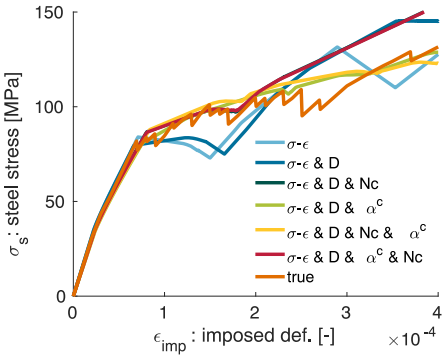

Figure 4.24: Stress-deformation curve with posteriror description of parameters

Table 4.3: Comparison of quantities computed with posterior values of parameters and the observed counterparts for given QoIs

Observations	Num. of cracks		Crack opening		Dissipation	
	Computed (−)	True (−)	Computed (mm)	True (mm)	Computed (Nmm)	True (Nmm)
$\sigma_s - \bar{\epsilon}$	2	5	0.2069	0.0420	0.01630	0.0120
$\sigma_s - \bar{\epsilon}$ & D	3	5	0.1857	0.0420	0.01196	0.0120
$\sigma_s - \bar{\epsilon}$ & D & N_c	3	5	0.1261	0.0420	0.01170	0.0120
$\sigma_s - \bar{\epsilon}$ & D & α^c	6	5	0.0376	0.0420	0.00440	0.0120
$\sigma_s - \bar{\epsilon}$ & D & N_c & α^c	3	5	0.1087	0.0420	0.01070	0.0120
$\sigma_s - \bar{\epsilon}$ & D & α^c & N_c	3	5	0.1224	0.0420	0.01140	0.0120

4.8 Concluding remarks

In this chapter, the following issues have been discussed:

- identifiability of material parameters of reinforced concrete given different quantities of interest,
- alternative experimental designs which show a greater sensitivity with respect to parameters of interest,
- accommodating the nonlinearities of the finite element solver,
- computational efficiency in solving the stochastic inverse problems.

In this chapter, observational data from the actual tensile tests on RC tie beams have been used to update the fracture and bond parameters of a damage model for reinforced concrete. Experimental data reported in [45] and used in the context of parameter estimation comprise the stress-deformation curves, values of crack opening of each individual crack and number of cracks obtained in three repeated experiments with the same geometry and material composition. Additionally, an experiment with loading and unloading cycles, which is very suitable for measuring the total dissipation, is proposed.

From the discussion above, one can conclude that combining different quantities of interest can improve the identifiability of the target parameters and reduce the discrepancy between the computed and measured responses. Some combinations are particularly favourable, such as the stress-deformation curve and dissipation for the estimation of the fracture properties of concrete ($\bar{\sigma}_f$, K_h, $\bar{\bar{\sigma}}_f$, $\bar{\bar{G}}_f$). On the other hand, properties governing the behaviour

at the interface (τ_y) are well estimated when the cracking-related quantities, such as the crack opening of a particular crack, are included. The combination of QoIs consisting of the stress-deformation curve, total dissipation and crack opening leads to reduced discrepancy between the computed and observed values of the number of cracks and the individual crack opening. The latter affirms the fact that stronger bond leads to higher number of cracks with smaller crack openings. From the results presented above, it is evident that it is not possible to obtain the best possible match in stress-deformation curve, dissipation, crack opening and number of cracks all at once. In some cases the addition of a successive QoI results in an increase in difference between the computed and measured value of some other QoI. Hence, material parameters need to be calibrated with respect to QoIs which are the most relevant for the considered problem. More precisely, in the study of the seismic safety, it is essential to obtain a good match in dissipation. Likewise, a good fit in stress-deformation curve is required for the analysis of the material strength. For the serviceability limit state design of structures, on the other hand, it is important to accurately compute the crack opening.

In general, there are two distinct approaches to parameter estimation via filtering: parameter smoothing and sequential update. The former, also known as the offline update, first carries out the prediction of the whole history and afterwards updates the target parameters in a single update step by taking into account the complete data history. The latter, referred to as the online update, is more suitable for the time dependent problems as it estimates the target parameters sequentially. In contrast to the offline update, the online update is directly influenced by the size of the time increment chosen for updating, with the update step close to zero yielding more accurate estimation results. In this chapter, target parameters are identified by the sequential GMKF enhanced with the PCE approximations. This approach is found to perform well even for highly nonlinear problems such as the one considered herein, as long as the size of the update step is kept quite small. For sufficiently small update step, there is no need to build a nonlinear map for the conditional expectation, as the problem becomes linear or quasi-linear within a particular update step. This is especially important as the Kálmán filter approaches are originally built for problems where both the observation operator and the CE map are considered to be linear. Moreover, instead of growing in time, the uncertainty is reduced as each successive loading step is computed with the last known posterior of the uncertain parameters.

The online update can be quite expensive when performed directly on the high fidelity model quantities. Thus, in the work herein the GMKF method

is enhanced with functional approximations. Namely, all the quantities in the filtering equation are expressed in terms of PCEs, which makes the computation of the posterior purely algebraic and straightforward, as it is only required to calculate the posterior polynomial coefficients. Although it greatly accelerates the GMKF update process, PCE based surrogate model has its drawbacks as well, the main one being that its applicability is limited to the problems with smaller number of uncertain parameters. If dimensionality of the stochastic problem is fairly large, one requires a large number of predictions to accurately build the surrogate model.

Chapter 5

Investigation of identifiability of material parameters of mortar

This chapter [1] focuses on estimation of the material parameters of the mortar mesostructure, i.e. hardened cement paste, aggregates and interface transition zone (ITZ). Geometry and the material mesostructure are based on the *micro computed tomography* (μCT) scans of the actual mortar specimen reinforced with externally bonded carbon fiber reinforced polymer (CFRP) plates. Mortar is modelled through a discrete lattice model, introduced in Section 3.3, consisting of spatial Timoshenko beams with embedded discontinuities. For parameter estimation, once again a Bayesian approach is employed and uncertain parameters are estimated given observations of the displacement field stemming either from *digital image correlation* (DIC) or numerical simulations. Due to high dimensionality of the stochastic problem,

[1] The work in this chapter has been completed in collaboration with Matteo Lunardelli (*Institute of Building Materials, Concrete Construction and Fire Safety* (iBMB), TU Braunschweig), Dr. Mijo Nikolić (*Faculty of Civil Engineering, Architecture and Geodesy*, University of Split, Croatia) and Prof. Dr.-Ing. Bojana Rosić (*Applied Mechanics and Data Analysis*, University of Twente, The Netherlands). Matteo Lunardelli has conducted the experimental investigation, the results of which are used for parameter estimation in Section 5.2.7 and contributed to modelling. Dr. Mijo Nikolić has provided the lattice model with embedded discontinuities, which is utilised to reproduce the experiment and generate predictions of observations. Prof. Dr.-Ing. Bojana Rosić has provided the concept of the research and guidance.

a sampling variant of the Kálmán filter, the ensemble generalised Kálmán filter (EnGKF), is adopted as a method for parameter identification. To cope with the nonlinearity of the concerned problem and technical requirements, a novel sequential approach which does not require coupling between the finite element solver and software for the stochastic analysis is proposed. Parameter identifiability is studied on two different shear experiments: actual double shear test and virtual shear test.

5.1 A novel approach to sequential Bayesian inference

Bearing in mind that the numerical lattice model is highly nonlinear, a fully sequential update of the uncertain parameters is preferred to smoothing over a certain time period. Sequential, or the so-called *online* update, consists of gathering the observational data at discrete time instances t_k and using the recorded data $\hat{\boldsymbol{Z}}^{(k)}$ to alter the probability description accordingly. For the sake of simplicity, the update procedure is illustrated only for the linear map of the conditional expectation. The ensemble generalised Kálmán filter Eq. (2.34) is rewritten as

$$\forall k: \ \boldsymbol{Q}_a^{(k)} = \boldsymbol{Q}_f^{(k)} + \boldsymbol{K}^{(k)} \left(\hat{\boldsymbol{Z}}^{(k)} - \left(\boldsymbol{Y}_f^{(k)} + \boldsymbol{E}^{(k)} \right) \right), \tag{5.1}$$

to indicate the sequential nature of the update. At any update step $t_{k>0}$, the prior ensemble $\boldsymbol{Q}_f^{(k)}$ in Eq. (5.1) equals the posterior ensemble from the last update step, i.e. $\boldsymbol{Q}_f^{(k)} = \boldsymbol{Q}_a^{(k-1)}$ holds. The predicted observations are a result of propagating the predicted values of the uncertain model parameters given as a prior ensemble $\boldsymbol{Q}_f^{(k)}$ from previous t_{k-1} to the current t_k update step by means of the observation operator, i.e. $\boldsymbol{Y}_f^{(k)} = Y_Q^{(k)}(\boldsymbol{Q}_f^{(k)})$. After each update step, the state (e.g. internal variables of the plasticity model) needs to be recomputed using the posterior ensemble $\boldsymbol{Q}_a^{(k)}$ of the uncertain input parameters at the current update step t_k. It is evident that such procedure requires coupling between the finite element solver and software for the stochastic analysis, in this case between *FEAP* and *Matlab*. Often, however, the coupling between the involved computer programs is not straightforward, or even feasible, or they are not located at the same computer (e.g. costly numerical simulations are often carried out on supercomputers or clusters). Hence, the aim is to give an alternative perspective on the problem. Instead

of recomputing the state with posterior description of the parameters directly through the FE solver, the problem is treated as a Bayesian inference problem. The predictions, i.e. realisations of the forward FE solver computed with the ensemble of prior samples $\boldsymbol{Q}_f^{(0)}$, are computed in an *offline* manner over the complete update interval of consideration, $k = 0, ..., N_t$, where N_t is the number of update steps, such that

$$\boldsymbol{Z}_{fe}^{(k)} = \boldsymbol{Y}_{fe}^{(k)} + \boldsymbol{\varepsilon}_f^{(k)}, \quad \boldsymbol{Y}_{fe}^{(k)} := Y_Q(\boldsymbol{Q}_f^{(0)}, t_0, t_k), \tag{5.2}$$

in which the subscript fe stands for the forecast of evolution.

The update, however, is performed *online* in three distinct stages:

1. correction of the prediction

$$\boldsymbol{Y}_f^{(k)} = \boldsymbol{Y}_{fe}^{(k)} + \boldsymbol{G}^{(k)} \left(\boldsymbol{Q}_a^{(k-1)} - \left(\boldsymbol{Q}_f^{(0)} + \boldsymbol{E}_r^{(k)} \right) \right), \tag{5.3}$$

   where $\boldsymbol{Y}_f^{(k)}$ is the ensemble of the corrected observation predictions, whereas $\boldsymbol{Y}_{fe}^{(k)}$ refers to the ensemble obtained from the FE predictions computed with prior samples $\boldsymbol{Q}_f^{(0)}$. The term $\boldsymbol{G}^{(k)}$ in Eq. (5.3) denotes the pseudo-Kálmán gain for the state update relating $\boldsymbol{Q}_f^{(0)}$ to $\boldsymbol{Y}_{fe}^{(k)}$ at the current update step t_k. The ensemble of the posterior random parameters from the previous update step, $\boldsymbol{Q}_a^{(k-1)}$, is considered as prior in the current step, i.e. $\boldsymbol{Q}_a(t_{k-1}) = \boldsymbol{Q}_f(t_k)$. The ensemble of the uncertain input parameters $\boldsymbol{Q}_f^{(0)}$ corresponds to Monte Carlo samples with which the FE observation predictions $\boldsymbol{Y}_{fe}^{(k)}$ are calculated. The term $\boldsymbol{E}_r^{(k)}$ denotes the pseudo-measurement error introduced for regularisation purpose.

2. parameter update

$$\boldsymbol{Q}_a^{(k)} = \boldsymbol{Q}_f^{(k)} + \boldsymbol{K}^{(k)} \left(\hat{\boldsymbol{Z}}^{(k)} - \left(\boldsymbol{Y}_f^{(k)} + \boldsymbol{E}^{(k)} \right) \right), \tag{5.4}$$

   in which $\boldsymbol{Q}_a^{(k)}$ is the ensemble of the updated uncertain input parameters, $\boldsymbol{K}^{(k)}$ is the Kálmán gain for parameter update, $\hat{\boldsymbol{Z}}^{(k)}$ are the actual (true) observations at the current step and $\boldsymbol{Y}_f^{(k)}$ is the ensemble of the corrected observation predictions obtained from Eq. (5.3).

3. state update

$$\boldsymbol{Y}_a^{(k)} = \boldsymbol{Y}_f^{(k)} + \boldsymbol{W}^{(k)} \left(\boldsymbol{Q}_a^{(k)} - \left(\boldsymbol{Q}_f^{(k)} + \boldsymbol{E}_r^{(k)} \right) \right), \tag{5.5}$$

with $\boldsymbol{Y}_a^{(k)} = \boldsymbol{Y}_f^{(k+1)}$ being the ensemble of the updated observation predictions. The pseudo-Kálmán gain $\boldsymbol{W}^{(k)}$ in this context relates $\boldsymbol{Q}_f^{(k)}$ to $\boldsymbol{Y}_f^{(k)}$.

Note that the algorithm above is only valid for the linear approximation of the conditional expectation. It can, however, be further generalised in order to take into account the higher order maps by employing the formulation derived in Section 2.5.3.

5.1.1 Method validation

The proposed approach is validated on an ordinary differential equation (ODE) example with a single uncertain parameter A. Evolution equation of such system can be defined as

$$y' = At; \quad y_0 = 0. \tag{5.6}$$

For validation purpose, uncertain parameter A is first estimated by a classical sequential EnGKF. In the classical approach, prediction of the state at update step t_k is computed by propagating the uncertainty through the high fidelity model given in Eq. (5.6) from t_{k-1} to t_k. In such a case, the uncertain model parameter A takes values from the last known posterior, which acts as prior in the current step. Its probabilistic description is updated by considering the discrete points on the response evolution curve depicted in Fig. 5.1(b) and denoted by "truth" as observations. The state update is computed in an analogous manner as its prediction, by considering the samples of A drawn from the posterior in the current step. This approach results in posterior mean of parameter A which equals 2.0499.

Afterwards, the update is repeated by employing the novel approach, in which the state prediction and state update are no longer computed by the high fidelity model given in Eq. (5.6) itself, but rather by the expressions given in Eq. (5.3) and Eq. (5.5), respectively. The resulting posterior mean of A slightly differs from the value obtained by the classical approach and equals 2.0406, whereas the assumed true value is equal to 2.0500.

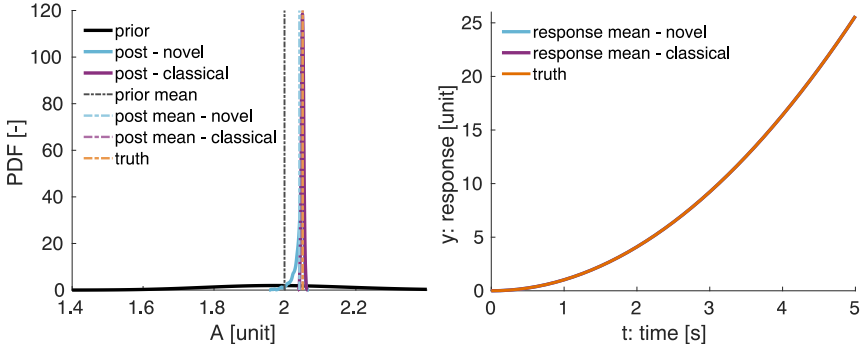

(a) (b)

Figure 5.1: Comparison of the classical and novel Bayesian update: a) posterior probability density functions of A; b) updated state

Although the classical approach yields more accurate posterior estimate, the difference between the posterior mean values is only 0.4537%, which is considered negligible. Fig. 5.1 compares the two different approaches described above in terms of the resulting posterior densities and quantity of interest computed with the corresponding posterior samples. Although the novel approach is somewhat less accurate compared to the classical one, the difference between the QoI computed with the obtained posterior mean values are negligible, see the overlapping resulting curves in Fig. 5.1(b).

5.2 Estimation of loading conditions and material parameters of mortar given data from a double shear test

This section introduces double shear experiment performed on a mortar specimen with externally bonded CFRP plates, discusses the peculiarities of the experimental setup and collected experimental data and presents the results of Bayesian parameter inference obtained by considering the observational data acquired by the optical measurement system and digital image correlation algorithms. A total of 5000 Monte Carlo samples of uncertain material parameters and load curves are generated and used for computing realisations of the stochastic forward problem. The latter are carried out in an

offline manner by the discrete lattice model with embedded discontinuities using the computer program *FEAP*. Target parameters are updated sequentially using the sampling based EnGKF, as described in Section 5.1. Elastic properties are updated by a linear approximation of the conditional expectation, whereas a nonlinear (quadratic) map is applied for the estimation of parameters governing the inelastic behaviour of the composite.

In the previous study on cracking of the RC beams, elaborated in Chapter 4, the loading increment is quite small, only 0.0002 mm. That means that the originally nonlinear problem can be treated as linear or quasi-linear within a single update step, which is equal to the loading step. In the example herein, however, the size of the load increment is at least twice as large. Hence, approximating the conditional expectation with a nonlinear map makes a significant difference in the accuracy of the posterior estimates.

5.2.1 Experimental setup

Observational data stems from the *far end supported* (FES) double shear test [193] performed on a specimen made of a crushed aggregate mortar prism of dimensions $28 \times 35 \times 16$ mm^3. The substrate is cast by cementitious mortar mixture and basalt aggregates of considerably smaller size (up to 4 mm) compared to aggregate in common concrete mixtures in order to fit the specimen dimensions, while providing the same performance (and same cement-to-aggregate ratio) as classical concrete of lower mechanical properties. On each side of the mortar prism, a CFRP plate of width $b = 7$ mm and thickness $t = 1.4$ mm is bonded to mortar using a two component epoxy resin. Fig. 5.2 depicts the specimen used in the experiment.

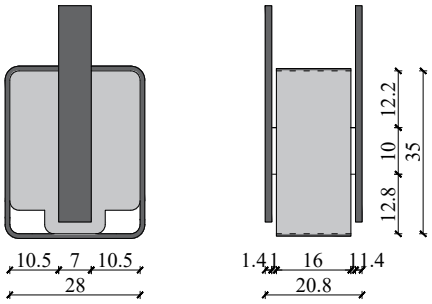

Figure 5.2: Sketch of the specimen with dimensions in $[mm]$

Note that the dimensions of the specimen are oddly small considering that the test should simulate fracture and debonding in concrete. This is a direct consequence of a limitation of the machine utilised for producing the tomographic scans of the material mesostructure. Due to small dimensions of the specimen, the typical experimental procedure consisting of fixing the specimen within the positioning frame and applying the tensile load simultaneously on both CFRP plates is ruled out. Instead, the mortar specimen is enveloped by a CFRP sheet, as shown in Fig. 5.2. Such adjustment facilitates the application of the load. The middle third of the specimen has somewhat greater height, which results in two hollow spaces at the outer bottom thirds of the specimen. For the sake of simplicity, in numerical simulations these holes are considered occupied by the cement paste.

Specimen is placed into a testing machine DEBEN CT5000, such that the free ends of the CFRP plates are clamped at the upper crosshead of the testing machine and steel stems are placed into the empty slots at the bottom of the specimen, as shown in Fig. 5.3. The test takes place under the displacement control, with imposed displacement of a magnitude 0.5 mm/min being applied directly on the stems and transferred accordingly to the CFRP sheet and mortar substrate until debonding failure of one of the CFRP plates.

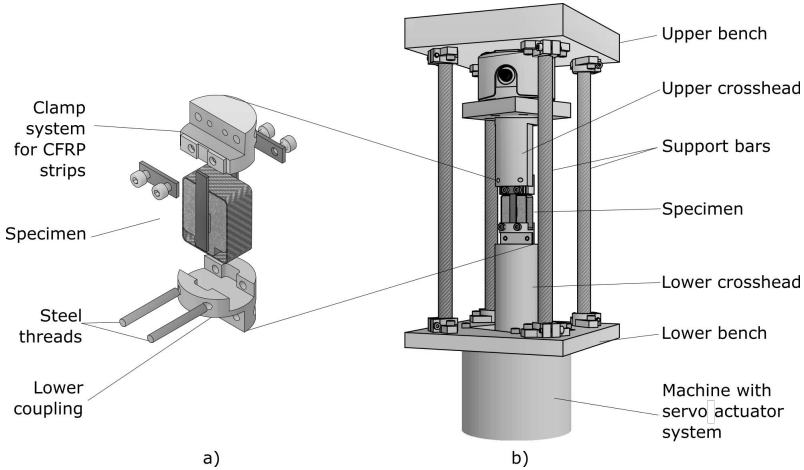

Figure 5.3: Experimental setup and boundary conditions *(courtesy of Matteo Lunardelli; iBMB, TU Braunschweig)*

The optical measurement system consists of high resolution cameras placed on both sides of the specimen, which aim to capture the surface displacements

on the front and back face of the specimen where the CFRP plates are placed and subsequently, their debonding and accompanying fracture in mortar. The measured displacements are expressed with respect to displacements obtained by averaging the measured values over the upper third surface (see the blue region in Fig. 5.5) of the specimen faces. The latter are considered as the reference surfaces in order to exclude the effect of the rigid body motion.

The primary goal of the experiment was to investigate the quality of the bond between concrete and CFRP as well as possible debonding failure modes. The behaviour of the bond is a key aspect for the assessment of the efficacy of the strengthening of existing concrete structures with externally bonded CFRP plates (see, e.g. [193, 30, 194]). Furthermore, the studies show that fracture in such an experiment typically occurs in concrete underneath the adhesive layer [26], which makes it highly dependent on the properties of concrete as well. The research presented herein investigates whether the information gain from the described double shear test is sufficient to update the knowledge about the uncertain material parameters of mortar.

5.2.2 Experimental data

Data acquired from the above described double shear experiment consist of the global force-slip curve (see Fig. 5.4(d)) and the surface displacements measured both at the front and back face of the specimen as shown in Figs. 5.4(a)–5.4(c).

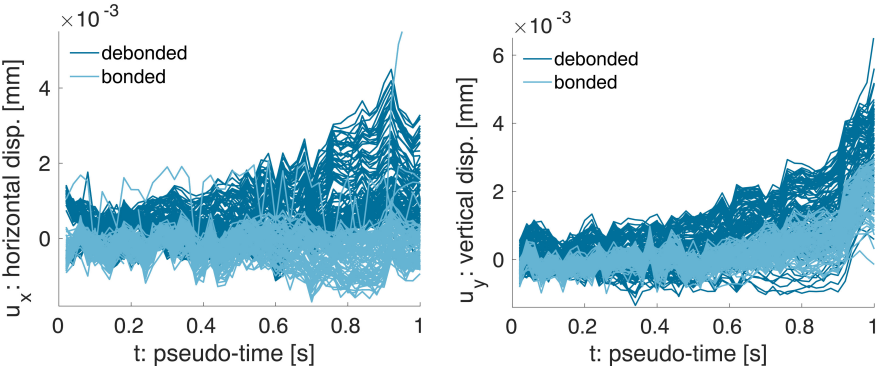

(a) (b)

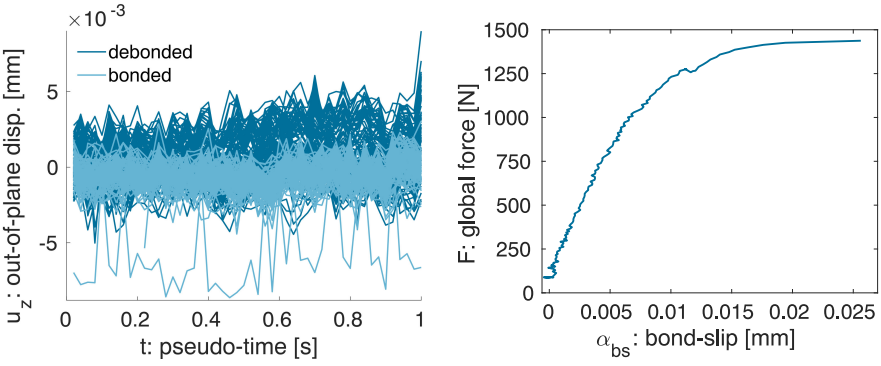

(c) (d)

Figure 5.4: Experimental results: a) horizontal displacements; b) vertical displacements; c) out-of-plane displacements; d) force-slip diagram

In the course of the experiment, one of the CFRP plates experiences debonding, which is characterised by displacements of a larger magnitude, as shown in Fig. 5.4. The specimen's faces are thus denoted by "debonded" and "not-debonded" ("bonded") to distinguish between the surface which experiences debonding of the CFRP plate and the surface at which the CFRP plate is still attached even after cracking takes place.

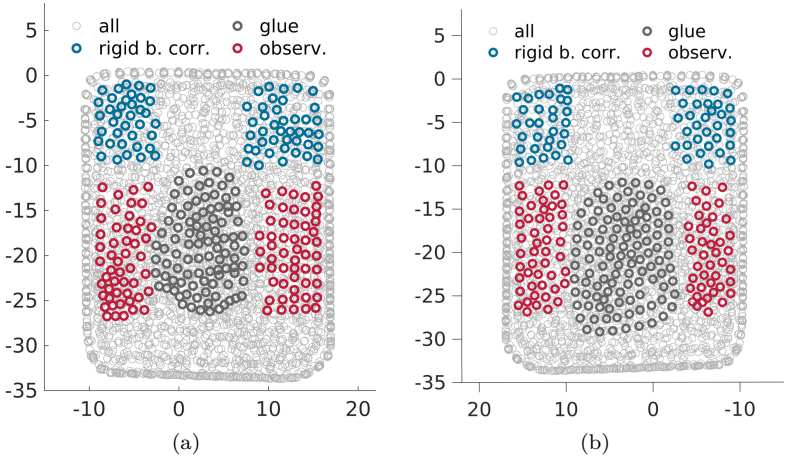

(a) (b)

Figure 5.5: Observation points: a) debonded side; b) not-debonded side

Depicted surface displacements are measured in the observation points (marked in red) at specimen's faces plotted in Fig. 5.5. They are chosen such that there is no overlap with respect to nodes corresponding to the contact area between the CFRP plates and mortar (dark grey points in Fig. 5.5) or with respect to nodes which are used for the rigid body motion correction (blue points in Fig. 5.5).

From Fig. 5.4, it is evident that all the displacement curves acquired by DIC contain a significant amount of measurement noise, the presence of which is inevitable, as reported in numerous works (see, e.g. [112, 49, 80]). Among sources of uncertainty causing the noise in data, the most significant is the camera noise resulting from temporal fluctuations of the grey levels perceived by each pixel of the camera sensor, incorrect camera calibration or unintended camera movements during the experiment, light conditions, quality of the speckle pattern etc. Magnitude of the measurement error is closely tied to a specific experimental setup and environmental conditions and thus, the error bounds need to be assessed independently for each DIC application. To statistically study the measurement noise, authors in [49] propose taking a series of static images of a specimen under the actual test conditions prior to application of any load. Amplitude of the measurement noise can then be determined by calculating the standard deviation at each measurement point. Ideally, a perfect measurement would give a zero-displacement at all measurement points and for all static images. In practice, however, that is usually not the case. Authors in [49] show the recorded DIC measurement error for a single static image and how averaging the results over more images leads to smaller error bounds. As reported in [1], measurement noise-strain ratio is particularly unfavourable for small-magnitude strains. This is directly observable from the displacement curves in Fig. 5.4(c), in which the out-of plane (z-direction) displacements having the smallest magnitude exhibit the largest measurement noise.

Bayesian inference is able to provide posterior estimates using noisy measurements. However, when the magnitude of the measurement noise is very large with respect to the actual values of quantities of interest, as in the case herein, it fails to produce precise estimates. Namely, as measurements are deemed as unreliable and given a little weight via the Kálmán gain, there is no significant information gain from data and the posterior uncertainty mostly reflects the prior one. Moreover, if one uses the sequential approach, large differences in the values of two successive measurements may impair the convergence of the posterior. Hence, the noise in the raw data has to be quantified and reduced by suitable filters prior to its use in parameter

estimation. In the absence of pre-assessment of the measurement noise, the results acquired by the DIC are assumed to describe the experiment only qualitatively. For the purpose of parameter estimation, though, a single realisation of the numerical model which closely resembles the noisy DIC data is selected and the resulting displacement curves are approximated by piecewise linear functions and treated as measurements. The comparison between the DIC true displacements and their virtual counterparts is given in Figs. 5.6(a)–5.6(f) and the true and virtual force-slip curves in Fig. 5.6(g). Only the displacements in y-direction, which contain the least amount of noise, are considered as measurements.

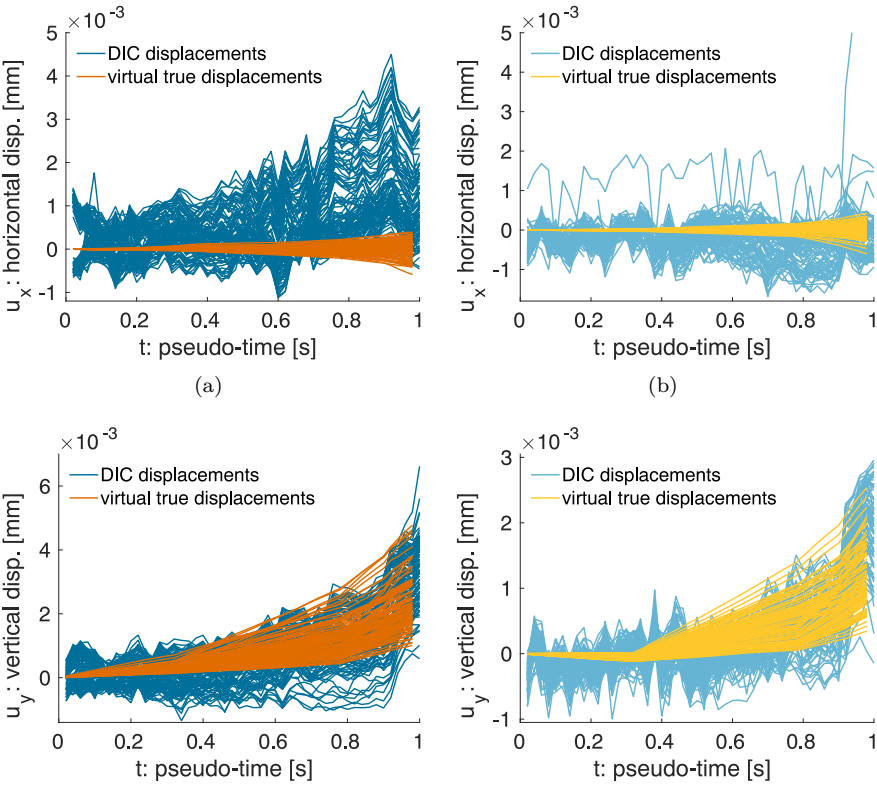

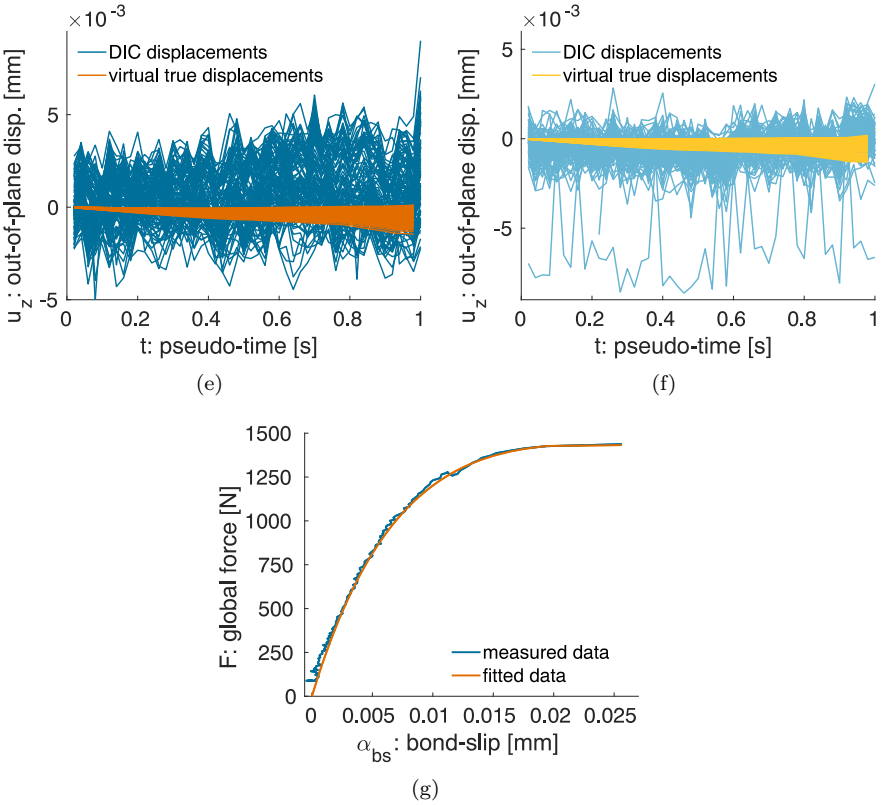

Figure 5.6: Experimental results: a) x-displacements at debonded side; b) x-displacements at not-debonded side; c) y-displacements at debonded side; d) y-displacements at not-debonded side; e) z-displacements at debonded side; f) z-displacements at not-debonded side; g) actual and virtual true force-slip curve

As a single realisation of a finite element solver which most closely resembles the noisy DIC displacements is taken as truth, there is no measurement error, but only a modelling one. Taking into account that the finite element model is a sophisticated 3D lattice model able to appropriately describe different stages in the material behaviour and their peculiarities and the finite element mesh is relatively fine, the magnitude of the error is taken as rather small ($\sim 1\%$ of the observed values of y-displacements), which reflects the confidence in the accuracy of the numerical model.

5.2.3 Finite element mesh and boundary conditions

The internal mesostructure of the composite is obtained from the computed tomography scans. The distinct phases of the composite, i.e. the cement matrix, aggregates and interface transition zone are extracted in the process of segmentation, the aim of which is to partition the greyscale μCT image into regions of a common brightness. The latter indicate regions of a common density. Each beam in the finite element mesh is thus assigned the appropriate material phase according to the value contained in the segmented matrix, reflecting the density of a particular phase. Beams for which one node is located within the aggregate and another within cement paste are assigned the interface properties. Fig. 5.7 depicts the segmented image of the real geometry and the corresponding finite element mesh. In Fig. 5.7, beams marked with red represent the aggregate, the ones marked with blue the interface transition zone and the remaining (grey) beams refer to cement paste.

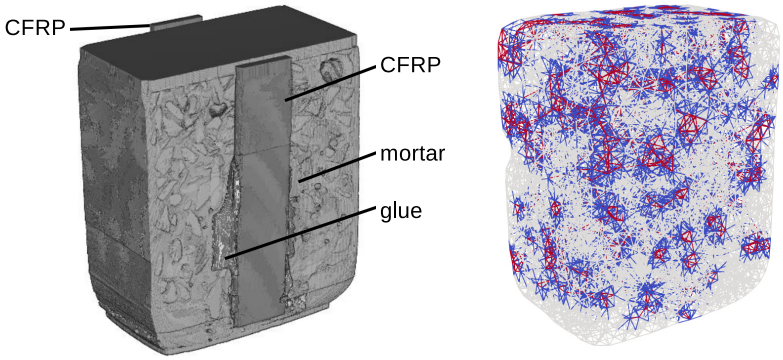

Figure 5.7: Specimen geometry and mesostructure: a) segmented image *(courtesy of Matteo Lunardelli; iBMB, TU Braunschweig)*; b) finite element mesh

Cross-sections of Timoshenko beams are calculated according to the Voronoi tessellation. As observed in the work herein, the distribution of cross-sections plays an important role in the quality of the results of numerical simulations. The most favourable cases have a negligible portion of cross-sections being very close to zero and the distribution of the values resembles a Gaussian

distribution centred around 1.0 mm^2. In that case, values of the material properties of each individual beam are closer to values of the global properties of the specimen. The actual distribution of the cross-sections used in numerical simulations is given in Fig. 5.8.

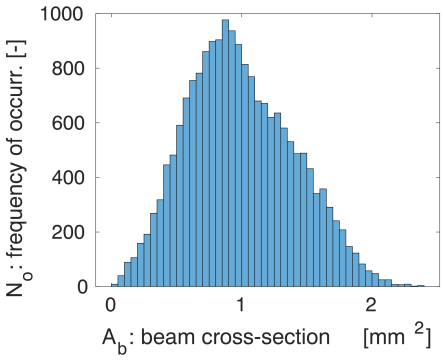

Figure 5.8: Distribution of the beam cross-sections

To reproduce the results of double shear experiment sketched in Fig. 5.3, the boundary conditions are imposed such that they take into account the positioning of the specimen inside the testing machine, the effects of the CFRP sheet enveloping mortar and of the CFRP plates glued to the specimen's faces.

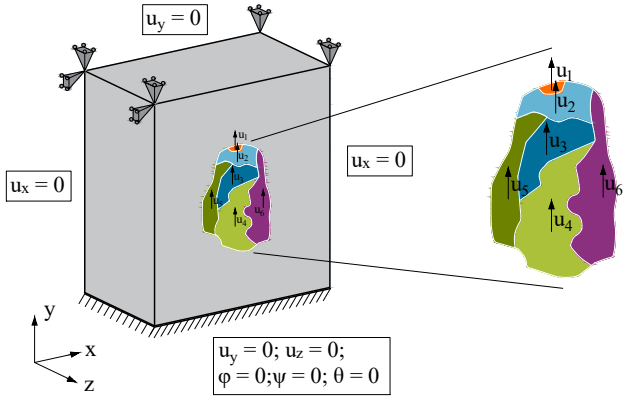

Figure 5.9: Double shear test: boundary and loading conditions

Fig. 5.9 summarises the imposed boundary conditions. The CFRP sheet is not explicitly modelled, however, as it prevents the movements in the directions orthogonal with respect to the CFRP sheet, the displacements in the y-direction at both upper and bottom surface and displacements in x-direction at the sides of the specimen are fixed. The bottom of the specimen is fixed inside the jaws of the testing machine, hence both the vertical y- and out-of-plane z-displacements, as well as rotations are restricted. Specimen is subjected to imposed displacements of a varying magnitude, assigned to the corresponding subdomains within the contact area, see Fig. 5.10.

5.2.4 Generation of imposed load curves with random coefficients

Due to peculiarities of the experimental setup, the boundary conditions are hard to reproduce. Namely, the load is applied through the steel stems which are pulling the CFRP sheet and subsequently, the mortar specimen. This attributes to the complexity of computational modelling of the experiment. However, as the epoxy resin which binds the CFRP plates to mortar is found to be fairly stiff, one can assume a perfect bond and refrain from modelling of the CFRP plates and CFRP-mortar interface. Instead, the load is applied in the form of imposed displacements directly onto the contact area.

The initial guess about the magnitude and shape of the imposed displacement curves is adopted from the DIC measurements by considering the surface displacements registered at the contact area as the imposed load. However, displacements measured at these points are not the exact displacements of mortar, but of the CFRP plates, as the DIC system can only measure the surface displacements. The latter indicates that, in reality, the bond is not perfect and magnitudes of the imposed load are indeed uncertain and require a proper probabilistic interpretation.

Firstly, it is investigated whether the measured displacements share some similarities in regards to magnitude and shape of the displacement evolution curves in certain regions within the contact area. Accordingly, the contact area is divided in several subdomains, the displacement history of each point in a particular subdomain exhibiting a similar trend. The reason behind that is twofold: the aim is to reduce the number of variables as the dimension of the considered stochastic problem is already quite large and the other reason being the improved convergence of the numerical simulations, as opposed

to the case in which all the nodes within the contact area have the same imposed load. The side of the specimen which experiences debonding and the one at which the CFRP plate remains bonded to the mortar specimen are considered separately and a set of imposed load curves is defined for each of them. Fig. 5.10 illustrates both areas and their division into subdomains. These areas preserve their shape throughout the entire experiment, as the utilised epoxy resin is rather stiff.

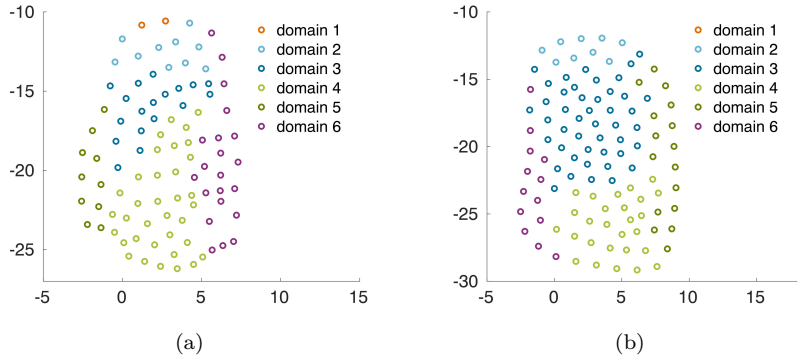

Figure 5.10: Imposed load domains: a) debonded side; b) not-debonded side

In the next step, the noisy displacement curves registered at the contact area, which now play the role of imposed loading, are fitted using piecewise linear functions. The experimental curves are divided into seven linear segments based on recognised trend lines. For each fitted piecewise linear curve, the interpolation coefficients by the piecewise linear regression can be calculated as

$$\bar{u} = \beta_0 + \beta_1 x + \sum_{j=1}^{n-1} \beta_{j+1}(x - \Delta_j) I(x - \Delta_j), \tag{5.7}$$

where n is the number of linear segments, β_0 is the y-intercept, β_j is the slope of a particular segment, Δ_j denotes the location of the slope change between two successive segments and $I(x-\Delta_j) = 1$ if $x \geq \Delta_j$ and 0 otherwise. For each curve, the locations of the slope changes Δ_j are considered to be equal. In order to enforce the fact that no pre-stressing is taking place in the specimen, the y-intercepts are set to be zero. Figs. 5.11–5.12 give an overview of imposed load curves per domain (see Fig. 5.10) for the debonded and not-debonded side of the specimen, respectively.

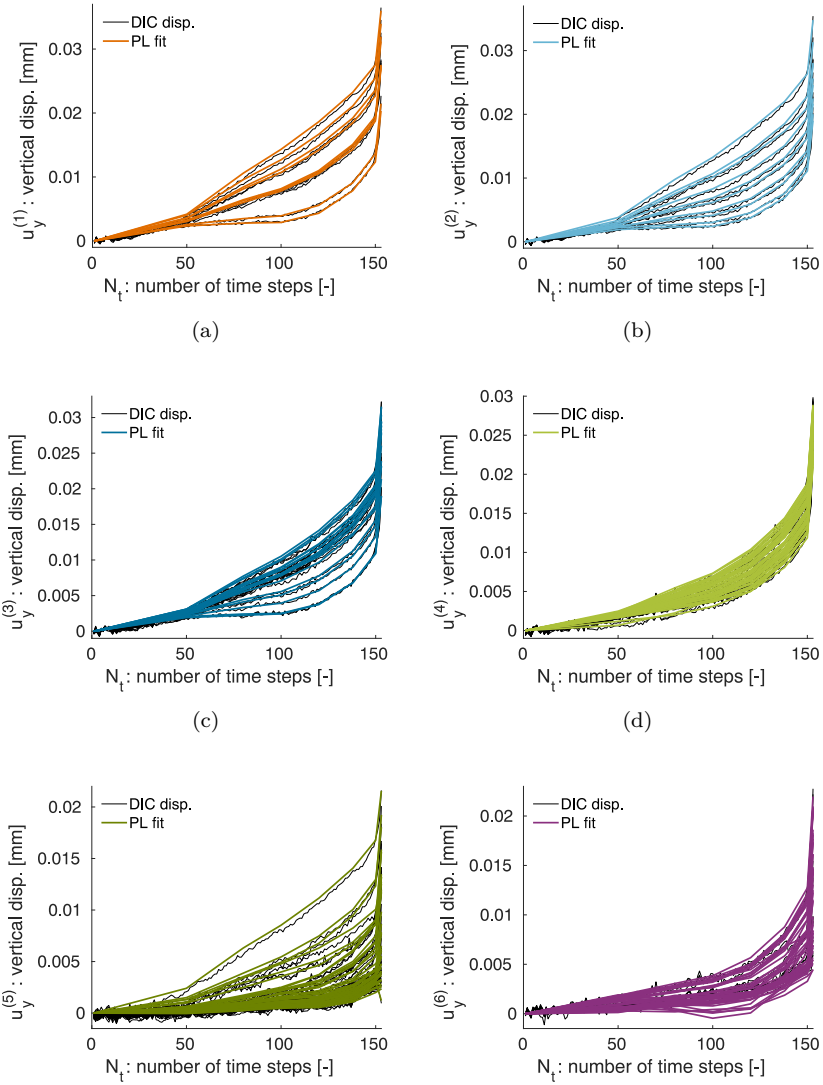

Figure 5.11: Deterministic imposed load curves at debonded side per domain: a) domain 1; b) domain 2; c) domain 3; d) domain 4; e) domain 5; f) domain 6

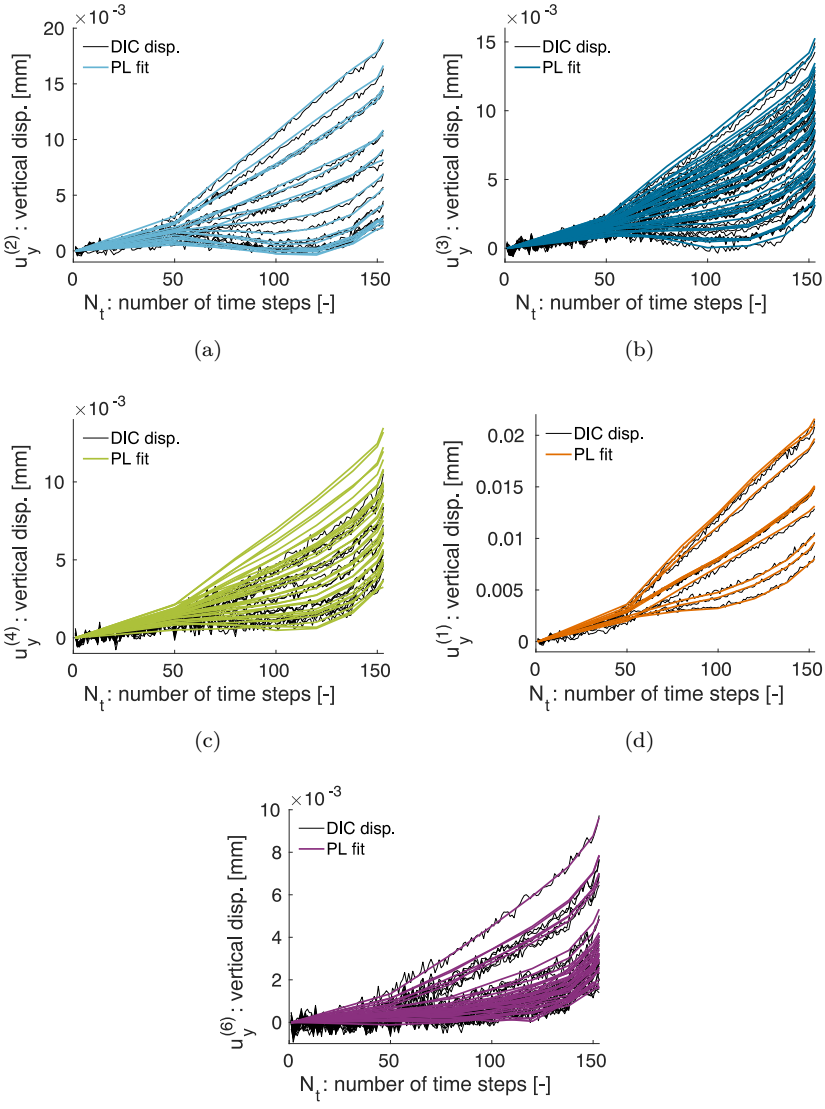

Figure 5.12: Deterministic imposed load curves at not-debonded side per domain: a) domain 2; b) domain 3; c) domain 4; d) domain 5; e) domain 6

As the magnitude of the imposed displacements is uncertain, coefficients of the deterministic piecewise linear curves are modelled as random variables. They are first normalised such that each individual interpolation coefficient is divided by the mean value. The resulting scaling factors are then utilised for calculation of the bounds $[a, b]$ of the uniform distribution $\mathcal{U}(a, b)$, the samples of which are used for defining realisations of the interpolation coefficients, i.e. $c(\omega) = (a + (b - a)u(\omega))\bar{\beta}$, where $u(\omega) \sim \mathcal{U}(0, 1)$ are samples from the standard uniform distribution and $\bar{\beta}$ is the mean of the deterministic interpolation coefficients, applied for removing the normalisation. Different seeds are used for the debonded and not-debonded side, making the load curves at both specimen's faces uncorrelated. With the newly obtained samples of interpolation coefficients c, one can generate an arbitrary number of imposed displacement curves.

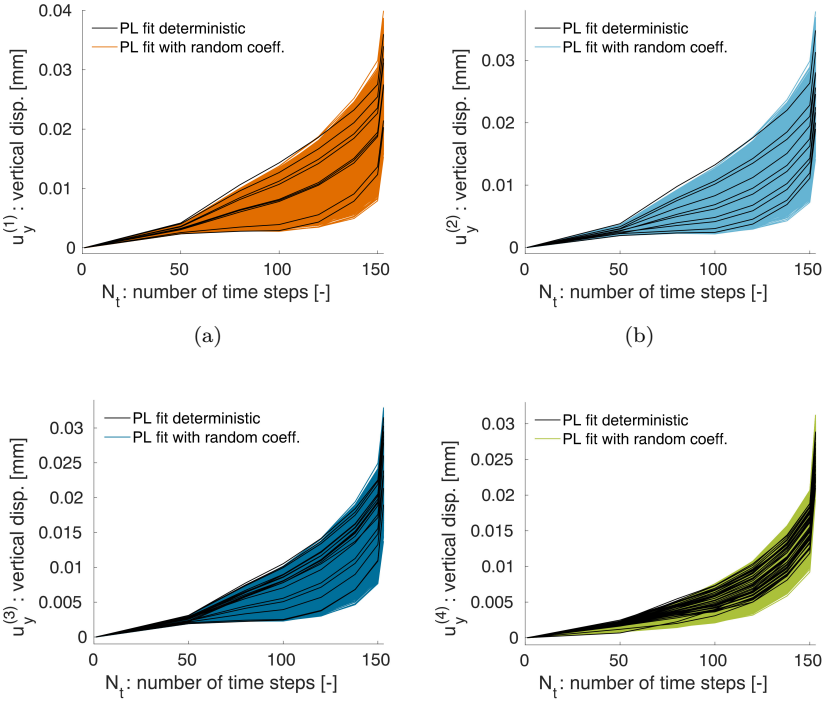

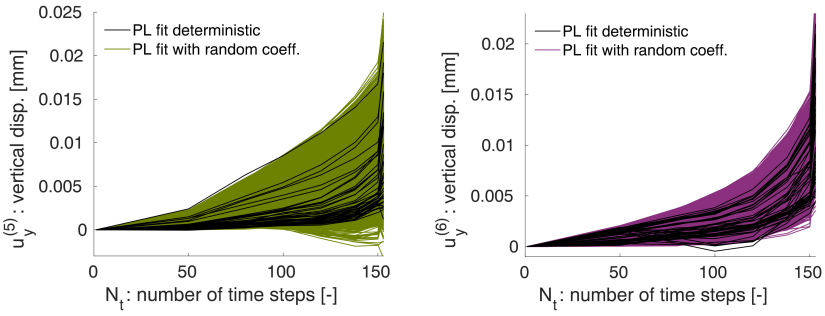

(e) (f)

Figure 5.13: Random realisations of imposed load curves at debonded side per domain: a) domain 1; b) domain 2; c) domain 3; d) domain 4; e) domain 5; f) domain 6

Fig. 5.13 and Fig. 5.14 depict the deterministic piecewise linear curves and 5000 realisations with the random interpolation coefficients, used in the numerical simulations, for both debonded and not-debonded side of the specimen.

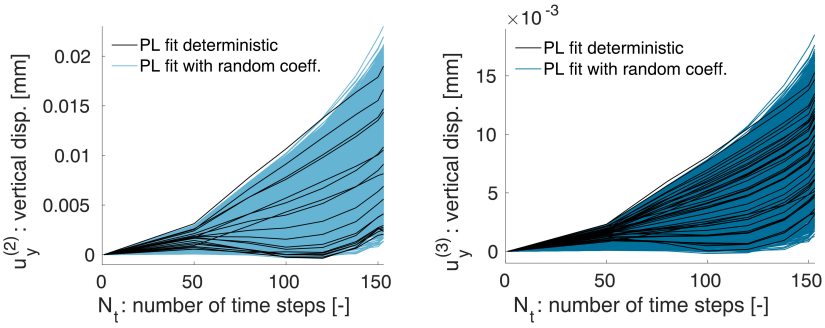

(a) (b)

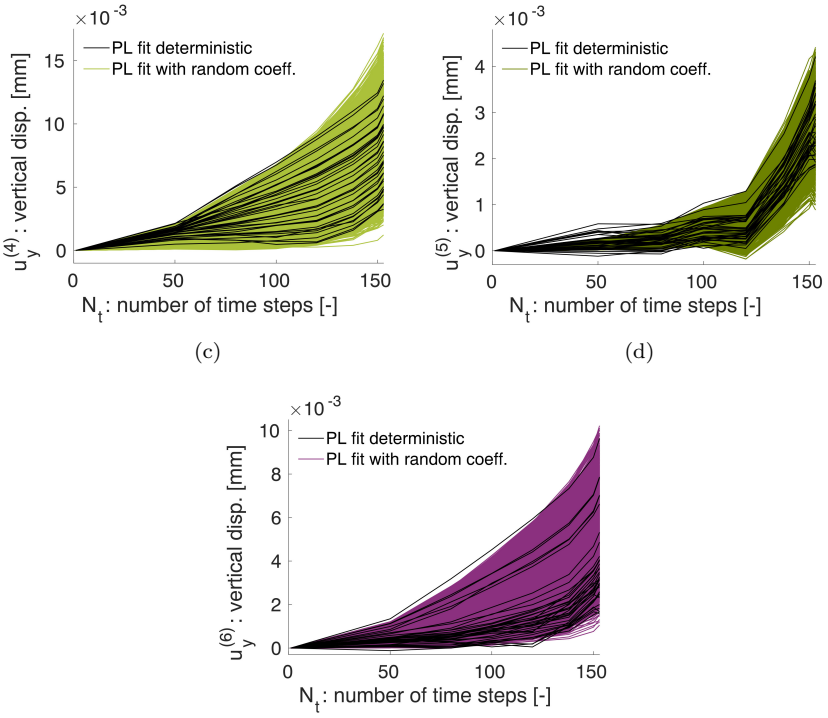

Figure 5.14: Random realisations of imposed load curves at not-debonded side per domain: a) domain 2; b) domain 3; c) domain 4; d) domain 5; e) domain 6

5.2.5 Identification of the uncertain load curves

The aim is to identify 11 imposed displacement curves (6 at the debonded and 5 at the not-debonded side), for each subdomain within the contact area between the CFRP and mortar (see Fig. 5.10). Bayesian inference is carried out as described in Section 5.1. The stochastic problem now contains 11 random variables corresponding to uncertain interpolation coefficients c introduced in Section 5.2.4, which are identified given DIC observations of the displacement field, or rather a realisation of the finite element solver which resembles the DIC observations, in the observation points shown in Fig. 5.5.

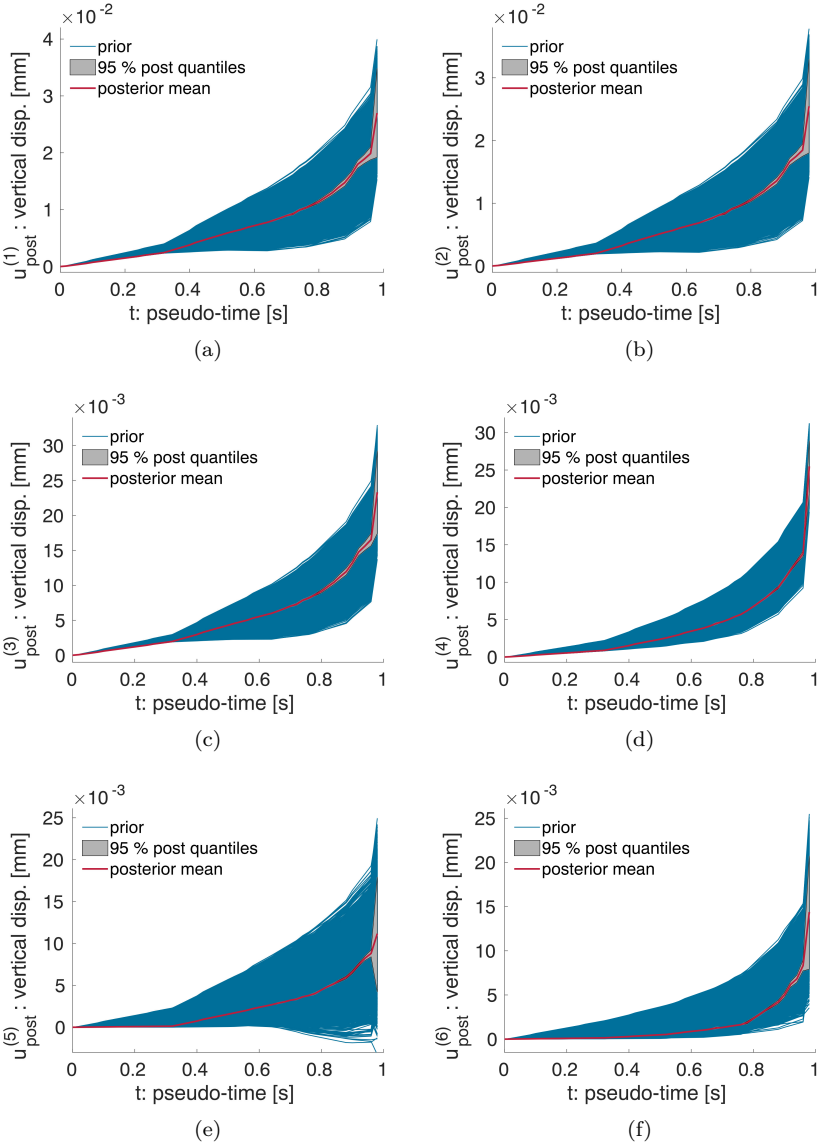

Figure 5.15: Prior realisations and posterior mean and quantiles of imposed load curves at debonded side per domain: a) domain 1; b) domain 2; c) domain 3; d) domain 4; e) domain 5; f) domain 6

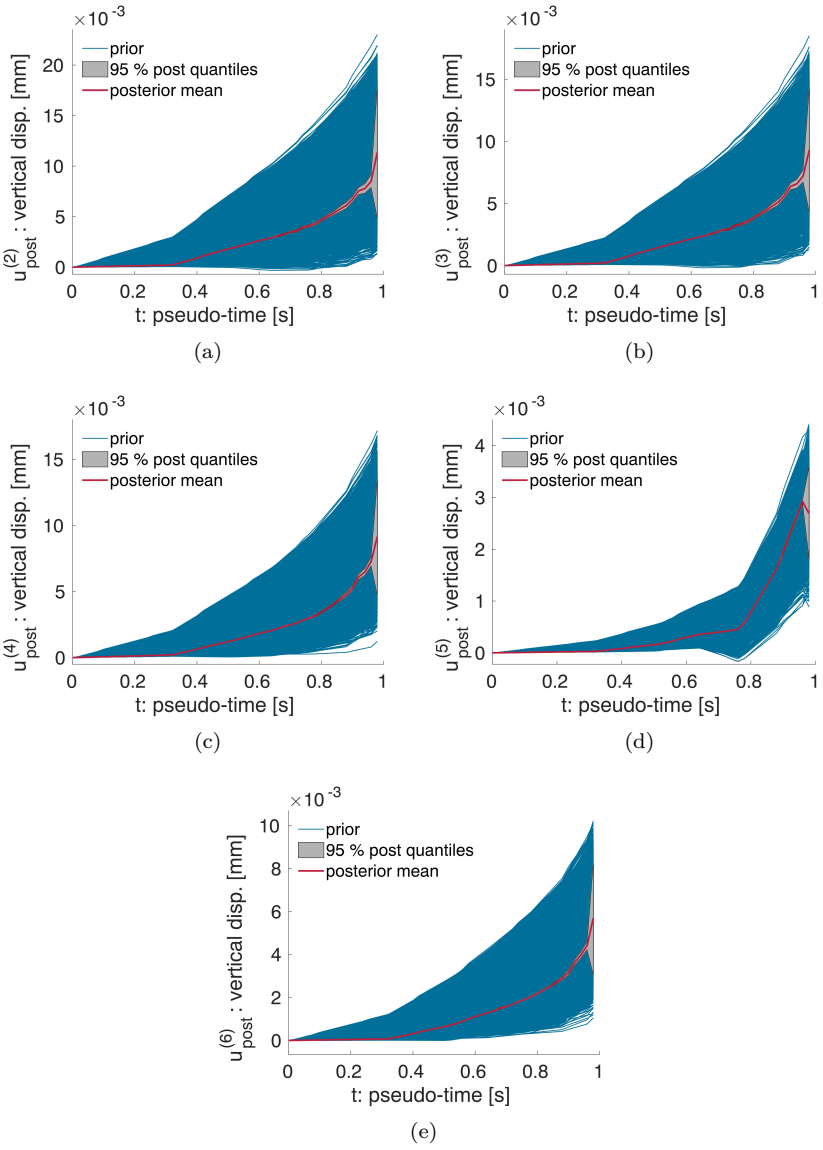

Figure 5.16: Prior realisations and posterior mean and quantiles of imposed load curves at not-debonded side per domain: a) domain 2; b) domain 3; c) domain 4; d) domain 5; e) domain 6

Bayesian inference results in posterior load curves given per each load subdomain, the mean and posterior quantiles of which are plotted in Fig. 5.15 for the debonded side of the specimen and in Fig. 5.16 for the not-debonded side. All of the resulting posterior curves lie within the region of sampled load curves. The 95% quantiles of the posterior load curves shown in Figs. 5.15–5.16 are considerably narrow, which implies a significant reduction of uncertainty in the loading conditions. For a comparison, realisations of the prior loading curves, plotted in colour in Figs. 5.13–5.14, are marked in blue and denoted as "prior" in Figs. 5.15–5.16.

5.2.6 Prior description of material parameters

In addition to 11 load curves defined per each subdomain of the contact area, the aim is to estimate a total of 34 material parameters pertaining to different stages in the behaviour of the composite: elasticity, material hardening and the post-peak softening behaviour. Mortar is modelled as a heterogeneous material consisting of three distinct phases: the cement matrix, aggregate and interface transition zone between them. Thus, the posterior of the following material properties modelled as random variables is sought: bulk K and shear G moduli (*elasticity*); yield stresses in compression σ_{y_c}, shear direction I or mode II τ_{y_1} and shear direction II or mode III τ_{y_2}, hardening moduli in compression K_c, shear direction I K_{τ_1} and II K_{τ_2} (*hardening*); ultimate stresses in mode I (tension) σ_{u_t}, compression σ_{u_c}, mode II (shear) τ_{u_1} and III (shear) τ_{u_2}, fracture energy in mode I (tension) G_{f_t}, compression G_{f_c}, mode II (shear) $G_{f_{\tau_1}}$ and mode III (shear) $G_{f_{\tau_2}}$ (*softening*). Elastic properties are sought for all three constituting materials, whereas the fracture properties only for cement matrix and interface, as aggregate almost never breaks.

Table 5.1: Prior probabilistic description: mean value and standard deviation of the uncertain elastic parameters of mortar

Property	Mean	Standard deviation
K_{cm}	10666.67 (MPa)	853.33 (MPa)
G_{cm}	6400.00 (MPa)	512.00 (MPa)
K_{itz}	4000.00 (MPa)	320.67 (MPa)
G_{itz}	2400.00 (MPa)	192.00 (MPa)
K_a	33333.33 (MPa)	2666.67 (MPa)
G_a	20000.00 (MPa)	1600.00 (MPa)

Table 5.2: Prior probabilistic description: mean value and standard deviation of the uncertain hardening parameters of mortar

Property	Mean	Standard deviation
$\sigma_{y_c,cm}$	4.00 (MPa)	0.40 (MPa)
$\tau_{y_1,cm}$	1.80 (MPa)	0.18 (MPa)
$\tau_{y_2,cm}$	1.80 (MPa)	0.18 (MPa)
$K_{c,cm}$	0.60 (MPa)	0.06 (MPa)
$K_{\tau_1,cm}$	0.60 (MPa)	0.06 (MPa)
$K_{\tau_2,cm}$	0.60 (MPa)	0.06 (MPa)
$\sigma_{y_c,itz}$	1.70 (MPa)	0.17 (MPa)
$\tau_{y_1,itz}$	0.90 (MPa)	0.09 (MPa)
$\tau_{y_2,itz}$	0.90 (MPa)	0.09 (MPa)
$K_{c,itz}$	0.50 (MPa)	0.05 (MPa)
$K_{\tau_1,itz}$	0.50 (MPa)	0.05 (MPa)
$K_{\tau_2,itz}$	0.50 (MPa)	0.05 (MPa)

Table 5.3: Prior probabilistic description: mean value and standard deviation of the uncertain softening parameters of mortar

Property	Mean	Standard deviation
$\sigma_{u_t,cm}$	7.80 (MPa)	0.78 (MPa)
$\sigma_{u_c,cm}$	16.80 (MPa)	1.68 (MPa)
$\tau_{u_1,cm}$	6.30 (MPa)	0.63 (MPa)
$\tau_{u_2,cm}$	6.30 (MPa)	0.63 (MPa)
$\bar{\bar{G}}_{f_t,cm}$	0.80 (N/mm)	0.08 (N/mm)
$\bar{\bar{G}}_{f_c,cm}$	1.20 (N/mm)	0.12 (N/mm)
$\bar{\bar{G}}_{f_{\tau_1},cm}$	0.80 (N/mm)	0.08 (N/mm)
$\bar{\bar{G}}_{f_{\tau_2},cm}$	0.80 (N/mm)	0.08 (N/mm)
$\sigma_{u_t,itz}$	3.10 (MPa)	0.31 (MPa)
$\sigma_{u_c,itz}$	7.30 (MPa)	0.73 (MPa)
$\tau_{u_1,itz}$	2.60 (MPa)	0.26 (MPa)
$\tau_{u_2,itz}$	2.60 (MPa)	0.26 (MPa)
$\bar{\bar{G}}_{f_t,itz}$	0.50 (N/mm)	0.05 (N/mm)
$\bar{\bar{G}}_{f_c,itz}$	0.90 (N/mm)	0.09 (N/mm)
$\bar{\bar{G}}_{f_{\tau_1},itz}$	0.50 (N/mm)	0.05 (N/mm)
$\bar{\bar{G}}_{f_{\tau_2},itz}$	0.50 (N/mm)	0.05 (N/mm)

Material properties described above are positive definite, hence they can only take positive values. That is reflected in the choice of the prior distribution.

Accordingly, it is assumed that all random variables follow the lognormal distribution, $\boldsymbol{q} \sim l\mathcal{N}(\mu_q, C_q)$, where μ_q and C_q denote mean and covariance, respectively. The prior mean values are selected based on the available experimental data on material property testing and preliminary numerical simulations. A standard deviation of 8% of the mean value μ_q is imposed on elastic uncertain parameters and a slightly higher value, $10\%\mu_q$ is assumed for the parameters governing the inelastic behaviour. Moreover, all random variables pertaining to material properties are considered as uncorrelated. Summary of prior description of the properties of individual Timoshenko beams (mean value and standard deviation) is given in Tables 5.1–5.3, in which index *cm* denotes cement matrix properties, *itz* interface transition zone and *a* aggregate.

5.2.7 Estimation of material parameters of mortar

In this section, the results of Bayesian inference of material parameters of mortar given DIC observations of the displacement field is presented. Numerical simulations are computed by assuming the imposed load curves described in Section 5.2.4. Bayesian inference is carried out in the same manner as the inference of the uncertain load curves, according to the procedure outlined in Section 5.1.

5.2.7.1 Estimation of elastic parameters

Immediately upon gathering a first portion of observations, parameters to be identified are the bulk K and shear G moduli. Namely, in the first few update steps mechanical behaviour of the composite is governed merely by its elastic constants and the remaining material parameters contribute to the response only later, when the elastic behaviour of the material is substituted by the inelastic phase.

Fig. 5.17 shows both prior and posterior PDFs of elastic constants of cement paste, interface transition zone and aggregate, respectively. Posterior is plotted in terms of several update steps to show that with every new observation, the posterior PDF becomes more narrow and converges towards the parameter true value.

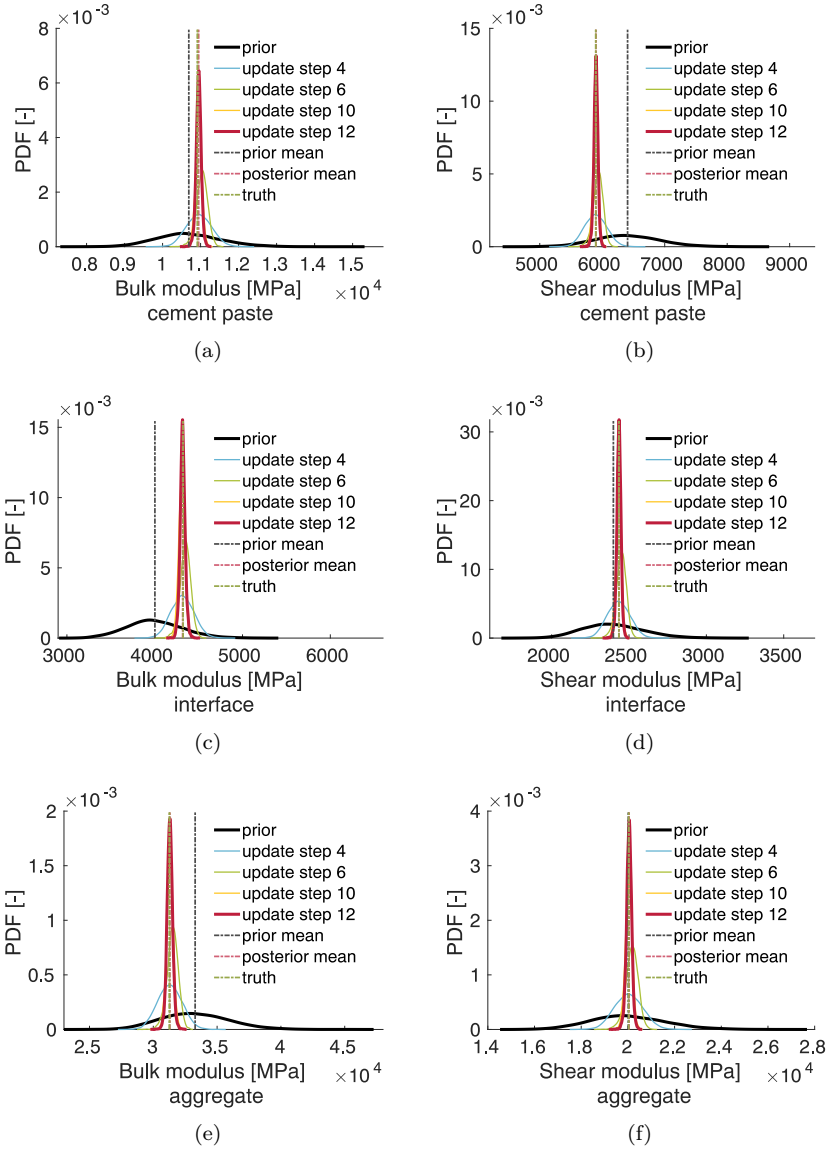

Figure 5.17: Prior and posterior PDFs of the elastic parameters: a) bulk modulus of cement paste; b) shear modulus of cement paste; c) bulk modulus of ITZ; d) shear modulus of ITZ; e) bulk modulus of aggregate; f) shear modulus of aggregate

In the elastic regime, only around 12 steps are needed to achieve an almost perfect match between the posterior mean and true value, with visibly decreased variance and subsequently, notably reduced uncertainty. In the later update steps, the PDFs of bulk and shear moduli remain centered around the converged value, exhibiting no further reduction in variance.

Table 5.4 gives an overview of prior and posterior values of elastic parameters and a comparison with regards to their true values. Comparing the standard deviation of prior and posterior, one can observe a slightly greater (around 2%) reduction of uncertainty in the posterior description of shear moduli compared to bulk moduli. The latter is in agreement with the shear nature of the experiment and confirms that the considered double shear experiment brings a higher information gain about the shear parameters.

Table 5.4: Prior and posterior probabilistic description of local properties: mean value and standard deviation of the uncertain elastic parameters estimated from double shear experiment

Property	Prior		Posterior		True
	Mean	Std. dev.	Mean	Std. dev.	
K_{cm} [MPa]	10666.67	853.33	10949.50	68.19	10918.90
G_{cm} [MPa]	6400.00	512.00	5898.53	33.84	5896.70
K_{itz} [MPa]	4000.00	320.67	4318.05	29.71	4323.47
G_{itz} [MPa]	2400.00	192.00	2434.67	13.97	2434.32
K_a [MPa]	33333.33	2666.67	31293.82	222.03	31267.35
G_a [MPa]	20000.00	1600.00	20049.55	114.97	20036.39

5.2.7.2 Estimation of parameters related to hardening

After few initial update steps, the influence of inelastic parameters governing the hardening behaviour becomes apparent. While PDFs of elastic properties remain stationary, PDFs of the yield stresses σ_{y_c}, τ_{y_1}, τ_{y_2} are visibly changing. In Figs. 5.18(a)–5.18(c) for properties of the cement paste and Figs. 5.18(d)–5.18(f) for the properties of the interface transition zone, one can notice a shift in the posterior mean towards the true value, accompanied by a reduction in variance. Information gain from the newly attained data causes further reduction in the uncertainty and around the update step 20, PDFs of yield stresses reach their final shape. The resulting posterior PDFs have a slightly higher variance compared to the posterior of the elastic properties, implying lower confidence about their actual values.

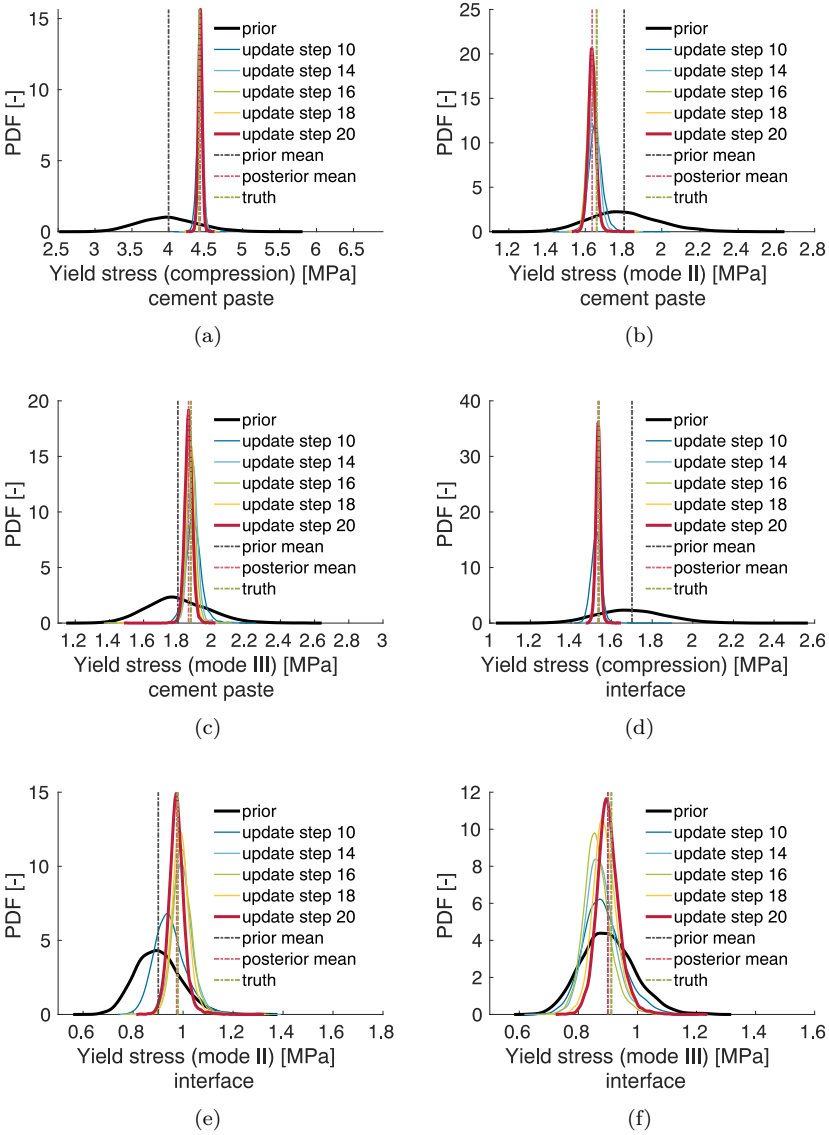

Figure 5.18: Prior and posterior PDFs of the yield stresses in: a) compression (cement); b) mode II (cement); c) mode III (cement); d) compression (ITZ); e) mode II (ITZ); f) mode III (ITZ)

As nonlinearities become more prominent, the reduction of variance is not as drastic as in the case of elastic parameters and yield stresses. That is directly observable in the posterior PDFs of the hardening moduli K_c, K_{τ_1}, K_{τ_2}, shown in Fig. 5.19. As soon as the initial linear response is replaced by the inelastic one, PDFs of the hardening moduli start fluctuating, with more prominent changes visible around update step 20. Thereafter, around 20 update steps are needed for the posterior mean and variance to reach their stationary values. From Fig. 5.19, one can note that all the posterior mean values of the hardening moduli are converging towards the true value, except the mean value of the hardening modulus for the interface in mode II, $K_{\tau_1,itz}$. This can be either due to lack of sensitivity of $K_{\tau_1,itz}$ with respect to the displacement field or the fact that the experiment does not bring enough information about this particular parameter (e.g. fracture is not realised in mode II).

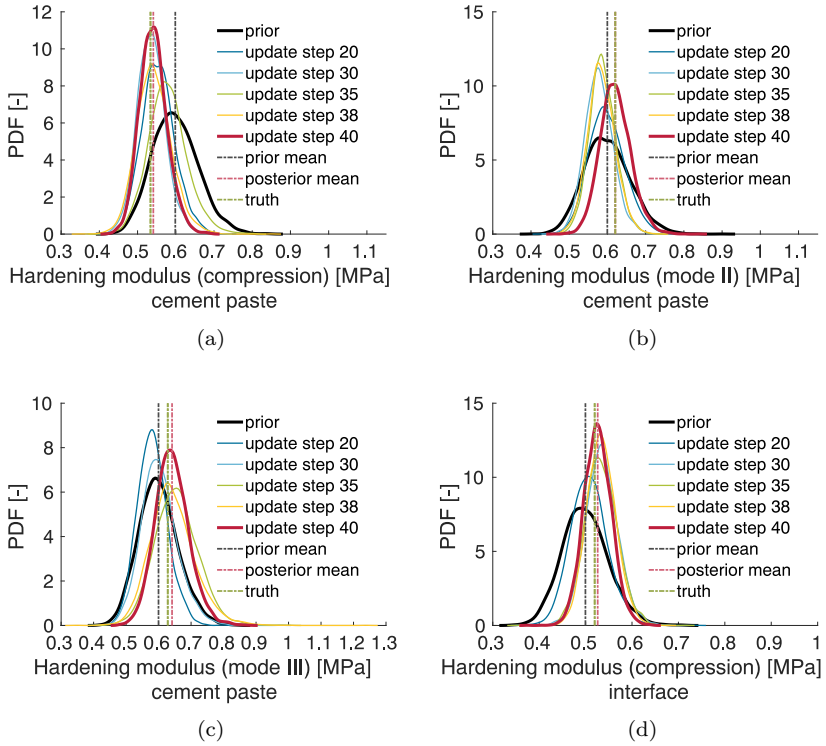

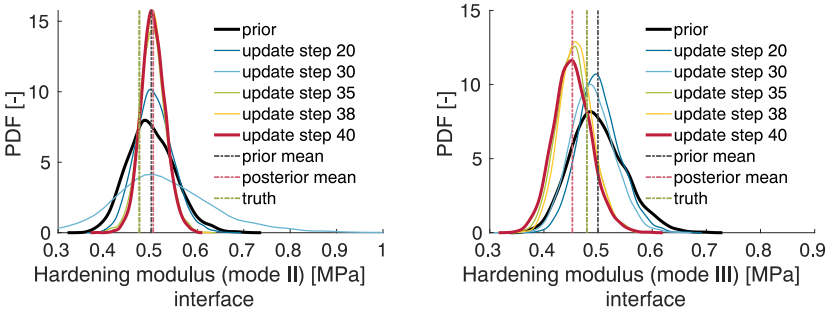

Figure 5.19: Prior and posterior PDFs of the hardening moduli in: a) compression (cement); b) mode II (cement); c) mode III (cement); d) compression (ITZ); e) mode II (ITZ); f) mode III (ITZ)

Table 5.5 summarises the prior and posterior description (i.e. the mean value and standard deviation) of the parameters related to hardening in comparison to their true values.

Table 5.5: Prior and posterior probabilistic description of local properties: mean value and standard deviation of the uncertain hardening parameters estimated from double shear experiment

Property	Prior		Posterior		True
	Mean	Std. dev.	Mean	Std. dev.	
$\sigma_{y_c,cm}$ [MPa]	4.00	0.40	4.42	0.028	4.41
$\tau_{y_1,cm}$ [MPa]	1.80	0.18	1.64	0.022	1.66
$\tau_{y_2,cm}$ [MPa]	1.80	0.18	1.86	0.024	1.88
$K_{c,cm}$ [MPa]	0.60	0.06	0.54	0.036	0.53
$K_{\tau_1,cm}$ [MPa]	0.60	0.06	0.62	0.040	0.62
$K_{\tau_2,cm}$ [MPa]	0.60	0.06	0.64	0.052	0.63
$\sigma_{y_c,itz}$ [MPa]	1.70	0.17	1.53	0.012	1.54
$\tau_{y_1,itz}$ [MPa]	0.90	0.09	0.98	0.033	0.98
$\tau_{y_2,itz}$ [MPa]	0.90	0.09	0.90	0.040	0.91
$K_{c,itz}$ [MPa]	0.50	0.05	0.53	0.030	0.52
$K_{\tau_1,itz}$ [MPa]	0.50	0.05	0.51	0.026	0.48
$K_{\tau_2,itz}$ [MPa]	0.50	0.05	0.45	0.035	0.48

5.2.7.3 Estimation of parameters related to softening

In the last stage of the parameter estimation, the goal is to identify parameters related to the softening part of the response, i.e. the ultimate stresses σ_{u_t}, σ_{u_c}, τ_{u_1}, τ_{u_2} and fracture energies $\bar{\bar{G}}_{f_t}$, $\bar{\bar{G}}_{f_c}$, $\bar{\bar{G}}_{f_{\tau_1}}$, $\bar{\bar{G}}_{f_{\tau_2}}$ in tension, compression and both shear modes, respectively. Both of these quantities are essential for the description of fracture in the material. Principal stress in specimen reaching the value of ultimate stress implies the appearance of a macroscopic crack, which can either represent a mode I, mode II or mode III fracture. The accompanying energy release in terms of fracture energies is also defined for each fracture mode independently. The results of Bayesian inference of these parameters are given in Figs. 5.20–5.21 for both cement paste and the interface transition zone.

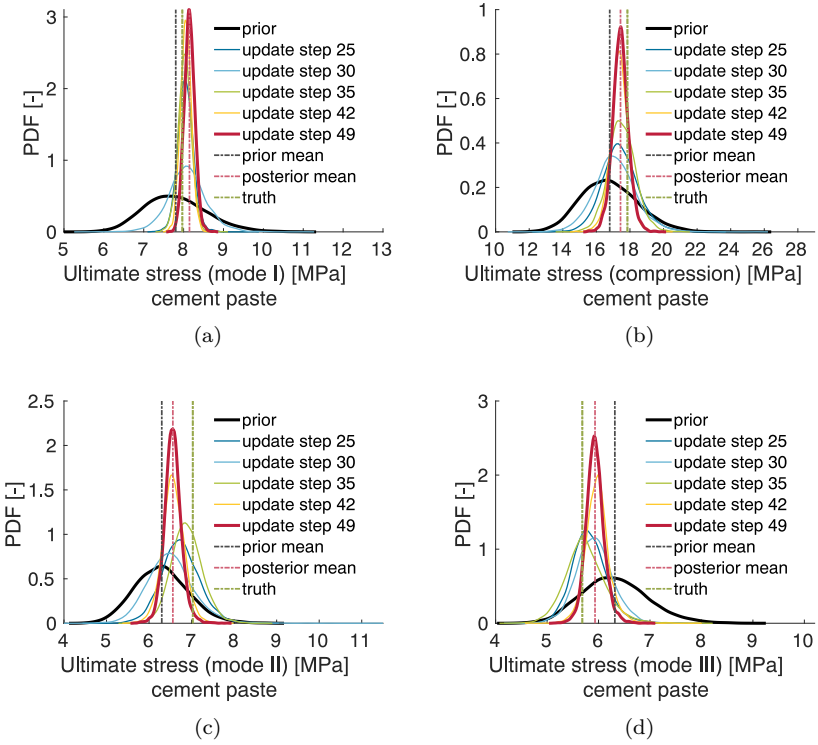

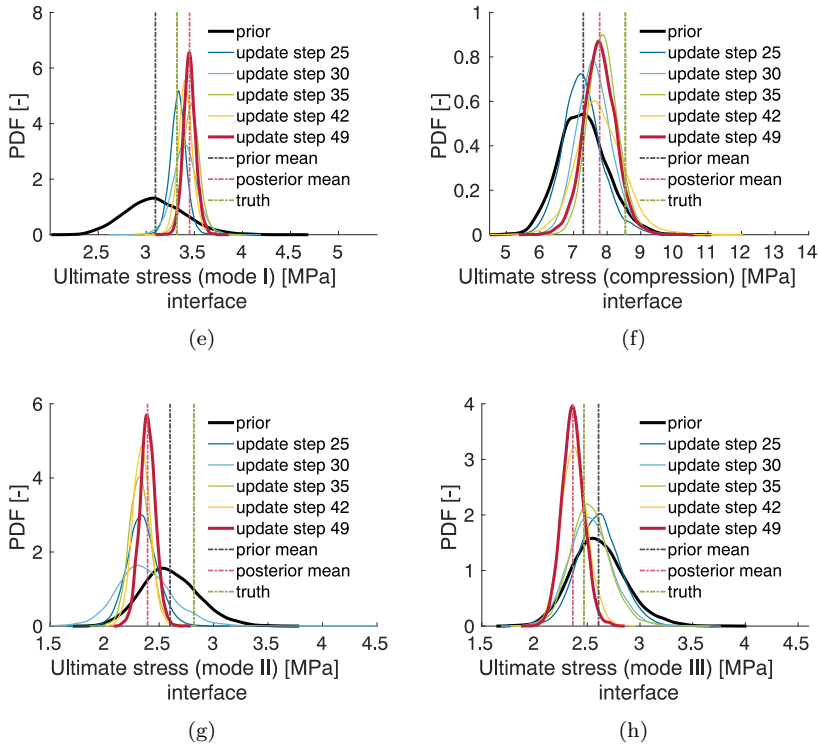

Figure 5.20: Prior and posterior PDFs of the ultimate stresses in: a) tension (cement); b) compression (cement); c) mode II (cement); d) mode III (cement); e) tension (ITZ); f) compression (ITZ); g) mode II (ITZ); h) mode III (ITZ)

In this phase, behaviour of the composite is quite nonlinear and the discrepancy between the computed and observed response is more significant compared to discrepancies in elastic and hardening phase. This is directly reflected in the quality of the updates, resulting in larger variance of the posterior or the posterior failing to converge towards the true value. Comparing the estimation of the cement paste and interface properties, there is a visible difference in the quality of the updates. Namely, while all posterior PDFs of the cement paste properties, with larger or smaller variance reduction, are shifted in the direction of their true values, the same does not hold for all the values of the interface properties (see Fig. 5.20(g) for which the posterior

is shifted in the opposite direction with respect to the true value).

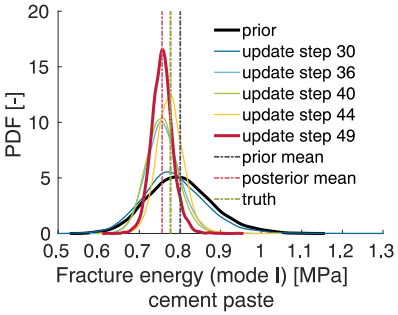

(a)

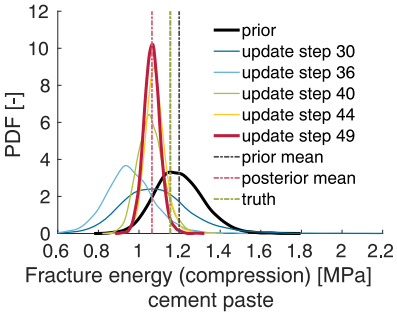

(b)

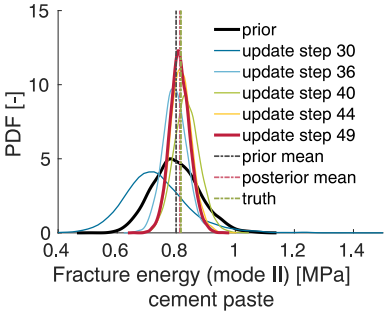

(c)

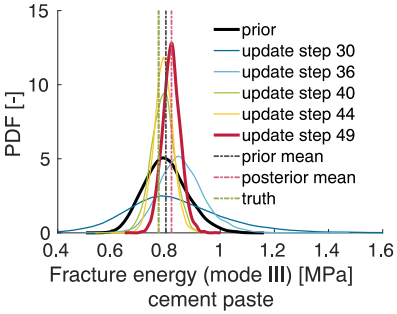

(d)

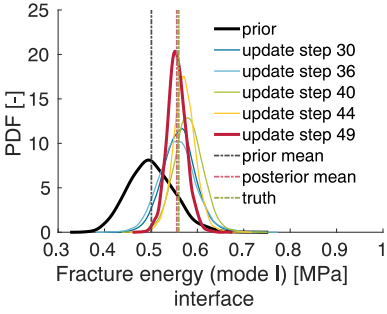

(e)

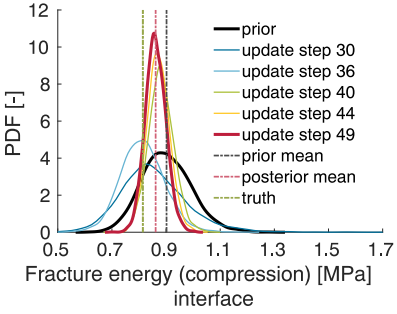

(f)

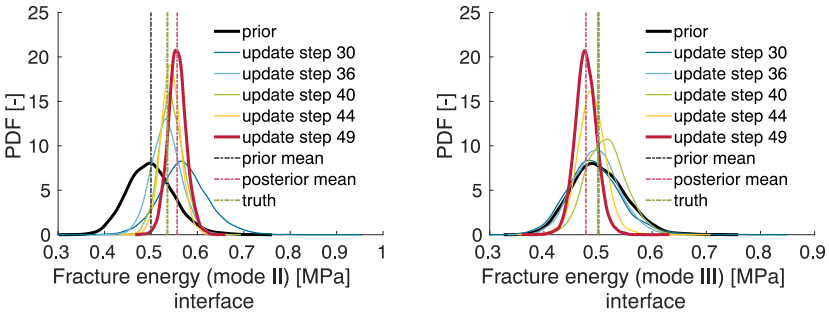

(g) (h)

Figure 5.21: Prior and posterior PDFs of fracture energies in: a) tension (cement); b) compression (cement); c) mode II (cement); d) mode III (cement); e) tension (ITZ); f) compression (ITZ); g) mode II (ITZ); h) mode III (ITZ)

Table 5.6: Prior and posterior probabilistic description of local properties: mean value and standard deviation of the uncertain softening parameters estimated from double shear experiment

Property	Prior		Posterior		True
	Mean	Std. dev.	Mean	Std. dev.	
$\sigma_{u_t,cm}$ [MPa]	7.80	0.78	8.15	0.135	7.968
$\sigma_{u_c,cm}$ [MPa]	16.80	1.68	17.44	0.479	17.850
$\tau_{u_1,cm}$ [MPa]	6.30	0.63	6.56	0.203	7.028
$\tau_{u_2,cm}$ [MPa]	6.30	0.63	5.93	0.179	5.685
$\bar{\bar{G}}_{f_t,cm}$ [N/mm]	0.80	0.08	0.76	0.027	0.777
$\bar{\bar{G}}_{f_c,cm}$ [N/mm]	1.20	0.12	1.06	0.041	1.154
$\bar{\bar{G}}_{f_{\tau_1},cm}$ [N/mm]	0.80	0.08	0.81	0.034	0.815
$\bar{\bar{G}}_{f_{\tau_2},cm}$ [N/mm]	0.80	0.08	0.82	0.034	0.772
$\sigma_{u_t,itz}$ [MPa]	3.10	0.31	3.45	0.066	3.319
$\sigma_{u_c,itz}$ [MPa]	7.30	0.73	7.78	0.488	8.543
$\tau_{u_1,itz}$ [MPa]	2.60	0.26	2.39	0.073	2.819
$\tau_{u_2,itz}$ [MPa]	2.60	0.26	2.36	0.106	2.469
$\bar{\bar{G}}_{f_t,itz}$ [N/mm]	0.50	0.05	0.56	0.021	0.560
$\bar{\bar{G}}_{f_c,itz}$ [N/mm]	0.90	0.09	0.86	0.038	0.814
$\bar{\bar{G}}_{f_{\tau_1},itz}$ [N/mm]	0.50	0.05	0.56	0.020	0.535
$\bar{\bar{G}}_{f_{\tau_2},itz}$ [N/mm]	0.50	0.05	0.48	0.021	0.500

Considering the results of Bayesian update shown in Figs. 5.20–5.21, one can conclude that no fracture mode stands out, which indicates that fracture is not purely a shear one, but rather a mixed-type fracture combining several modes. The latter is a result of the experimental design, which assumes that the mortar specimen is enveloped with a CFRP sheet (see Section 5.2.1). Such setup influences the fracture pattern of mortar. Detailed description of the prior and posterior for the parameters related to softening is given in Table 5.6.

5.2.8 Validation of the results

Results of Bayesian inference are validated by computing realisations of the finite element solver with the posterior mean values of parameters and imposed load curves and comparing them against the displacement field obtained by the piecewise linear approximation of the actual displacement curves registered by the optical measuring system. Inference can be deemed as successful if measured quantities are accurately reproduced with the posterior description of parameters. Fig. 5.22 shows a good agreement between the observed surface displacements and the ones computed with the posterior mean of the uncertain parameters.

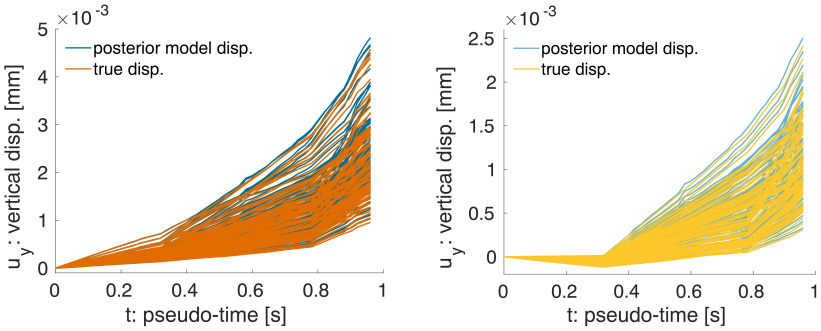

Figure 5.22: Comparison between the true virtual y-displacements and model displacements computed with the posterior mean values of parameters in observation points at: a) debonded side; b) not-debonded side

Although posterior of some of the parameters has not converged, i.e. $K_{\tau_1,itz}$ and $\tau_{u_1,itz}$, computed displacements still closely follow the true displacement curves, which implies that the displacement field is not sensitive to these particular parameters.

In addition, it is explored whether the fracture pattern from a double shear experiment can be reproduced by the lattice model. In the actual experiment, macroscopic cracks are located around the area where CFRP plates are glued to the mortar specimen, as shown in Fig. 5.23(a). The side view of a μCT scan of the cracked specimen, depicted in Fig. 5.23(b), gives a better insight into the crack pattern. CFRP plate at the left side of the specimen is still bonded despite fracture taking place within mortar, whereas the one at the right side (front side in Fig. 5.23(a)) is completely debonded from the mortar specimen.

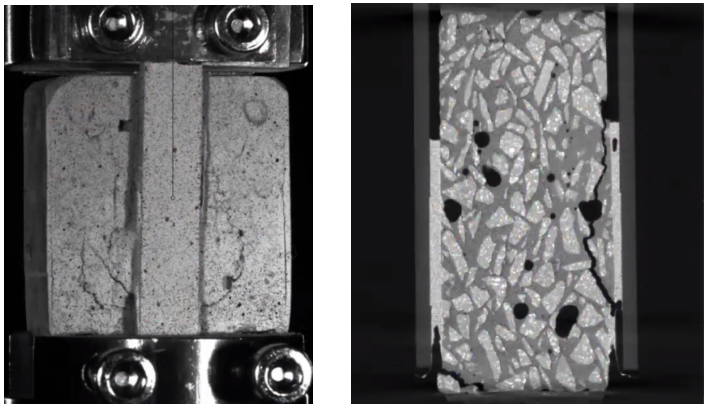

(a) (b)

Figure 5.23: Fracture in far end supported double shear experiment: a) front view; b) side view *(courtesy of Matteo Lunardelli; iBMB, TU Braunschweig)*

Fig. 5.24 illustrates the fracture pattern obtained by the finite element simulation with posterior description of the identified parameters in all three fracture modes. Only the debonded side of the specimen is plotted, where the cracks are the most prominent. Both the experimental and numerical analysis results in similar fracture pattern, with macroscopic cracks located around the glue area and largest crack opening in the bottom portion of

cracked beams.

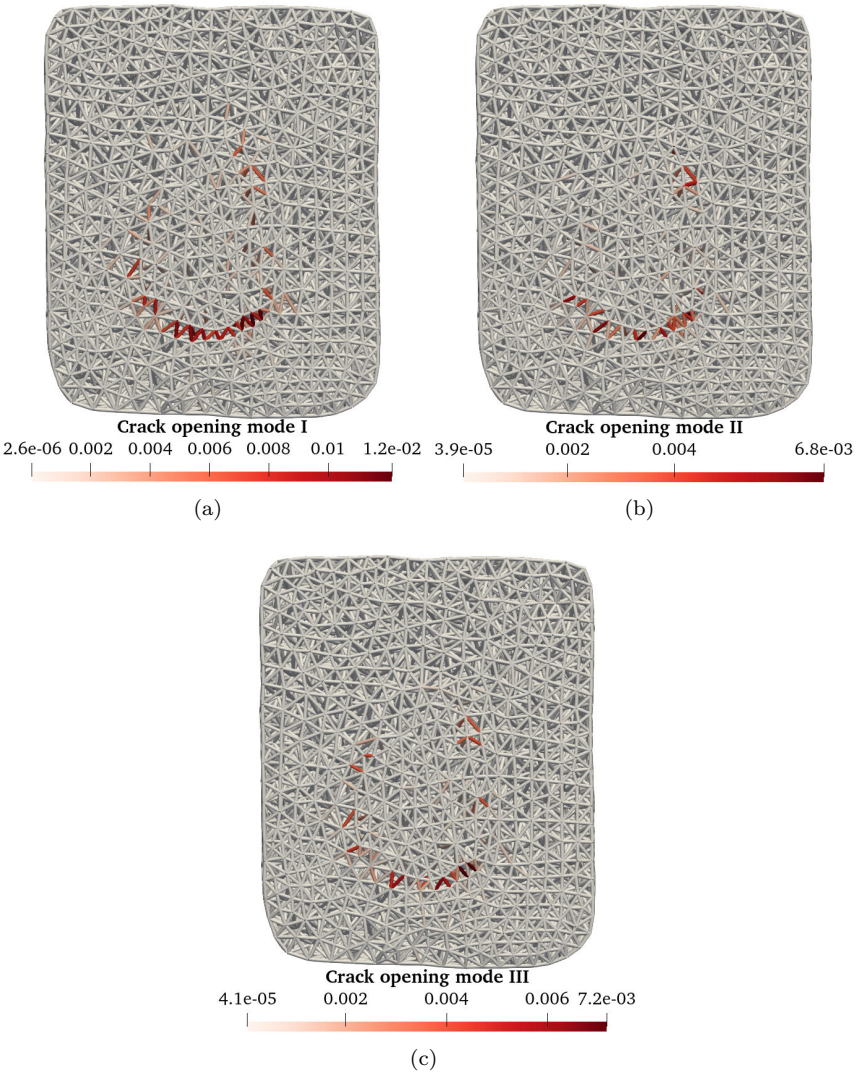

Figure 5.24: Crack opening in the last loading step in: a) mode I; b) mode II; c) mode III

Moreover, from Fig. 5.24 one can observe a portion of cracked beams located within the glue area, which is in good agreement with the experiment as the debonding takes place at this side of the specimen (see Fig. 5.23(b) for comparison).

5.3 Estimation of material parameters of mortar given data from a virtual shear test

In Section 5.2, the results of Bayesian inference of uncertain material parameters of mortar given experimental data from a far end double shear test are presented. Although the experiment was initially designed for the purpose of investigating the bond behaviour of the externally bonded CFRP plates, the posterior values are in good agreement with the virtual truth and only a handful of parameters are not converging. However, the previously described experiment is not ideal for investigation of fracture in mortar, as the CFRP sheet prevents any movements at the enveloped surfaces, thus influencing the composite's fracture pattern. This is reflected in the posterior PDFs of fracture parameters exhibiting a relatively high variance. Hence, this section explores whether the identifiability of the parameters of interest can be improved by an alternative experimental setup.

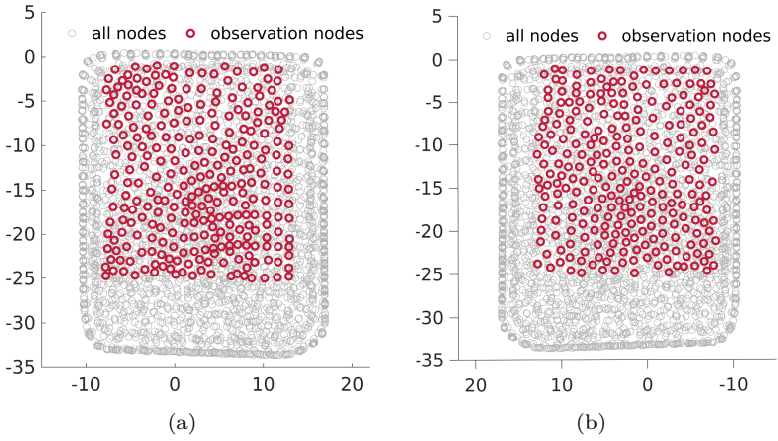

Figure 5.25: Observation points: a) front side; b) back side

Target material parameters of mortar are estimated in the same manner as in Section 5.2, by a sequential version of EnGKF combining the offline prediction and online update. Numerical simulations are computed using the computer program *FEAP* with a sample size of 1000. Prior description of uncertain model parameters is given in Tables 5.1–5.3. Observational data stems from the virtual shear experiment described in Section 5.3.1 and consists of displacements measured at discrete points at both front and back faces of the specimen, as shown in Fig. 5.25. Observation points are located at the shear failure planes, where shear fracture takes place, to maximise the information gain about the fracture parameters.

5.3.1 Experimental setup

Geometry of the mortar specimen introduced in Section 5.2.1 is retained, i.e. the substrate is cast by cementitious mortar mixture and basalt aggregates in the form of a prism of dimensions $28 \times 35 \times 16\ mm^3$. The CPRF plates and CFRP sheet are excluded in the present example, as only the properties of mortar are interesting in this context.

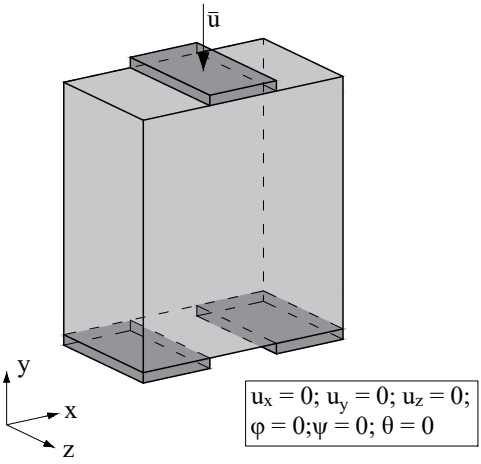

Figure 5.26: Virtual shear test: boundary and loading conditions

Boundary and loading conditions resemble the ones in a direct shear test [85], i.e. similar as in [20, 195]. Specimen is supported on two rigid blocks placed at the outer thirds of the span, whereas the load is applied uniformly at the

middle third of the upper surface, as shown in Fig. 5.26. The test is carried out under controlled displacement at the rate of $\Delta\bar{u} = 0.0004\ mm/s$.

5.3.2 Estimation of elastic parameters

Fig. 5.27 illustrates the posterior PDFs of the elastic material properties, i.e. the bulk and shear moduli, whereas the detailed posterior descriprion and comparison with respect to the virtual truth is given in Table 5.7. Note that, although the target parameters are estimated using a sequential EnGKF, only the final posterior PDFs are plotted in Fig. 5.27 along with the final PDFs obtained in Section 5.2.7.1 by exploiting the data from a double shear test. This allows a direct comparison between the posterior estimates resulting from Bayesian inference using data from two different shear experiments and thus facilitates drawing conclusions about the parameter identifiability.

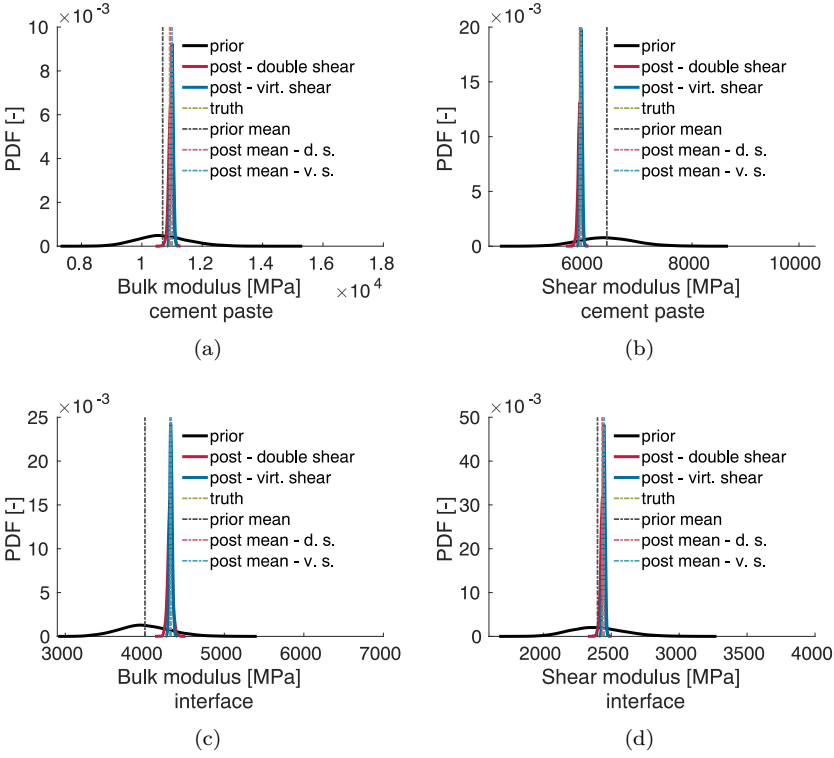

(a) (b)

(c) (d)

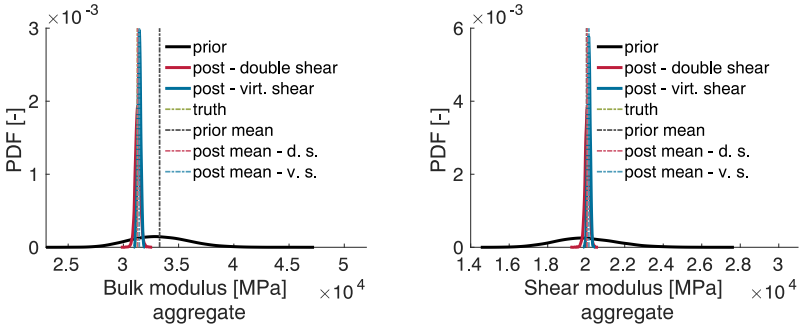

(e) (f)

Figure 5.27: Comparison of posterior PDFs estimated from double shear test and virtual shear test. Prior and posterior PDFs of the elastic properties: a) bulk modulus of cement paste; b) shear modulus of cement paste; c) bulk modulus of ITZ; d) shear modulus of ITZ; e) bulk modulus of aggregate; f) shear modulus of aggregate

Table 5.7: Prior and posterior probabilistic description of local properties: mean value and standard deviation of the uncertain elastic parameters estimated from virtual shear experiment

Property	Prior		Posterior		True
	Mean	Std. dev.	Mean	Std. dev.	
K_{cm} [MPa]	10666.67	853.33	10962.56	50.53	10918.90
G_{cm} [MPa]	6400.00	512.00	5908.64	23.46	5896.70
K_{itz} [MPa]	4000.00	320.67	4316.39	18.71	4323.47
G_{itz} [MPa]	2400.00	192.00	2439.90	9.69	2434.32
K_a [MPa]	33333.33	2666.67	31448.20	156.67	31267.35
G_a [MPa]	20000.00	1600.00	20072.63	79.59	20036.39

Results of Bayesian inference of parameters in the elastic regime are very similar to the ones reported in Section 5.2.7.1. In both cases, the resulting posterior PDFs are very narrow, reflecting the improved confidence in the parameters' actual values. There are slight differences, though, when comparing values from the Tables 5.4 and 5.7. The posterior PDFs are closer to the true value when observations are taken from double shear test, but the difference in the posterior mean values is up to 0.4%, which can be deemed as

negligible. The displacement field from the virtual shear experiment shows greater sensitivity with respect to elastic parameters, as the variance reduction is more apparent. In conclusion, both double shear experiment and virtual shear experiment can bring enough information in order to identify the elastic parameters with satisfactory accuracy.

5.3.3 Estimation of parameters related to hardening

Figs. 5.28–5.29 depict the posterior PDFs of the yield stresses and hardening moduli obtained from a virtual shear test. The posterior PDFs in Figs. 5.28–5.29 stem from the final update step and are plotted together with the final PDFs obtained in Section 5.2.7.2. A comparison between the posterior estimates and corresponding true values is given in Table 5.8.

When the material starts exhibiting nonlinear behaviour, the differences between the updates obtained from double shear test and virtual shear test become more obvious. Comparing the posterior PDFs of the hardening quantities given in Tables 5.5 and 5.8, one can notice a much greater reduction in variance when using the data from the virtual shear experiment.

Observations from the virtual shear test show a significant sensitivity with respect to yield stresses in all three fracture modes. The respective posterior PDFs become so narrow that the results are almost deterministic, as shown in Figs. 5.28 and 5.29. Posterior estimates pertaining to properties of the interface transition zone, see Figs. 5.28(d)–5.28(f), turn out to be more exact and converge faster, compared to estimates pertaining to properties of the cement paste, see Figs. 5.28(a)–5.28(c).

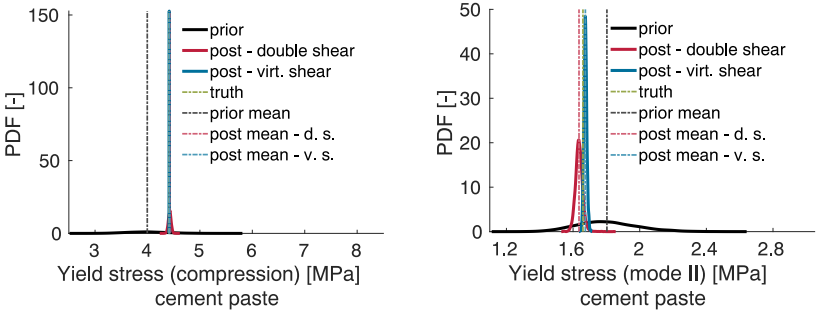

(a) (b)

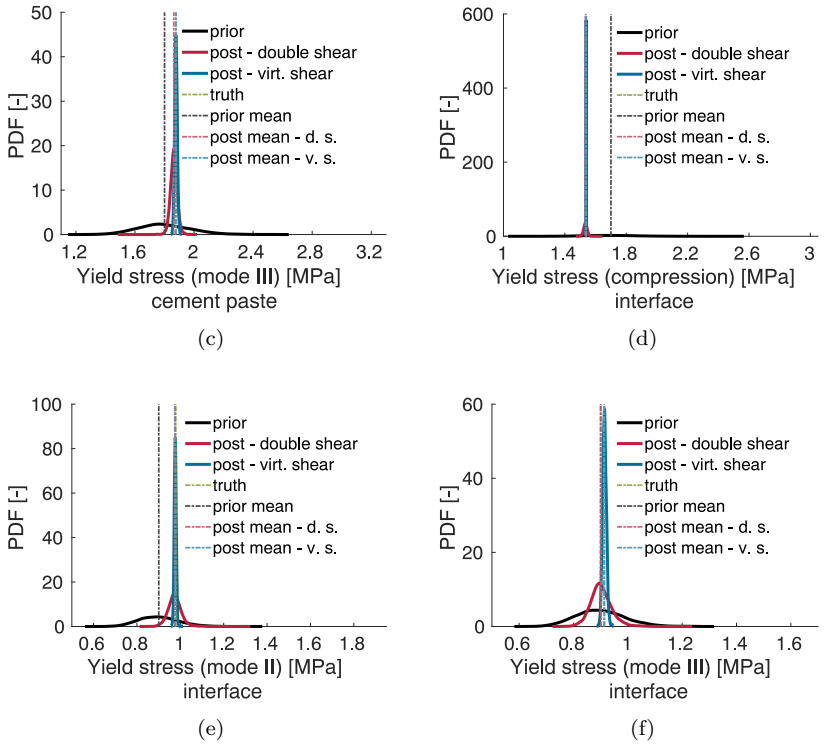

Figure 5.28: Comparison of posterior PDFs estimated from double shear test and virtual shear test. Prior and posterior PDFs of the yield stresses in: a) compression (cement); b) mode II (cement); c) mode III (cement); d) compression (ITZ); e) mode II (ITZ); f) mode III (ITZ)

Estimation of the hardening moduli, governing the hardening behaviour of the composite, shows significant improvements with respect to results presented in Section 5.2.7.2. Namely, the variance of the posterior PDFs is visibly reduced and posterior mean values are closer to the true values, see Tables 5.5 and 5.8. This holds for all hardening moduli, except for the hardening modulus in compression for cement paste (see the blue curve in Fig. 5.29(a)), which is better estimated in the previous case (see the red curve in Fig. 5.29(a)). The hardening modulus in mode III for the interface, which was previously not converging towards the true value, is now more accurately estimated (see Fig. 5.29(f)).

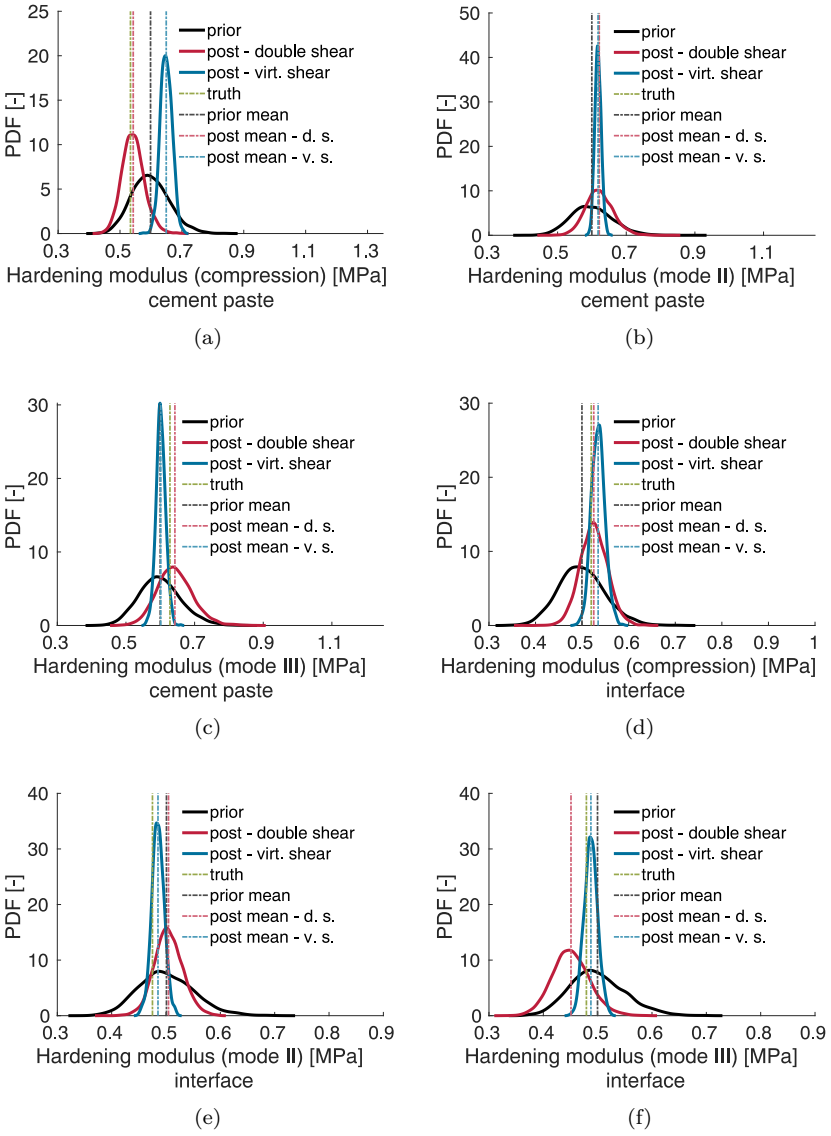

Figure 5.29: Comparison of posterior PDFs estimated from double shear test and virtual shear test. Prior and posterior PDFs of the hardening moduli in: a) compression (cement); b) mode II (cement); c) mode III (cement); d) compression (ITZ); e) mode II (ITZ); f) mode III (ITZ)

Overall, the estimates in hardening regime are more accurate when one considers observations from the virtual shear test. The latter particularly holds for the parameters describing the shear properties of the composite.

Table 5.8: Prior and posterior probabilistic description of local properties: mean value and standard deviation of the uncertain hardening parameters estimated from virtual shear experiment

Property	Prior		Posterior		True
	Mean	Std. dev.	Mean	Std. dev.	
$\sigma_{y_c,cm}$ [MPa]	4.00	0.40	4.42	0.003	4.41
$\tau_{y_1,cm}$ [MPa]	1.80	0.18	1.67	0.011	1.66
$\tau_{y_2,cm}$ [MPa]	1.80	0.18	1.89	0.011	1.88
$K_{c,cm}$ [MPa]	0.60	0.06	0.65	0.019	0.53
$K_{\tau_1,cm}$ [MPa]	0.60	0.06	0.62	0.010	0.62
$K_{\tau_2,cm}$ [MPa]	0.60	0.06	0.60	0.014	0.63
$\sigma_{y_c,itz}$ [MPa]	1.70	0.17	1.54	0.001	1.54
$\tau_{y_1,itz}$ [MPa]	0.90	0.09	0.97	0.006	0.98
$\tau_{y_2,itz}$ [MPa]	0.90	0.09	0.92	0.010	0.91
$K_{c,itz}$ [MPa]	0.50	0.05	0.52	0.016	0.52
$K_{\tau_1,itz}$ [MPa]	0.50	0.05	0.48	0.012	0.48
$K_{\tau_2,itz}$ [MPa]	0.50	0.05	0.49	0.012	0.48

5.3.4 Estimation of parameters related to softening

As nonlinearities become more prominent and the material experiences strain-softening behaviour, differences in the posterior estimates become even more evident. Examining the final posterior PDFs of the ultimate stresses plotted in Fig. 5.30, one can immediately notice a significant improvement in the accuracy of the estimates, compared to the PDFs from Section 5.2.7.3 plotted in Fig. 5.20. Namely, the posterior mean values are closer to the true values and variance is significantly smaller when data stems from the virtual shear experiment. Moreover, in the case of double shear test all target parameters are updated equally well, which does not hold for the case of a virtual shear test. The latter results in very good estimates of the parameters related to shear, while the ultimate stresses in tension cannot be updated, as the posterior PDFs advance in the opposite direction with respect to the true values, see Fig. 5.30(a) and Fig. 5.30(e). This can be explained by the fact that fracture in double shear experiment is not purely in shear, but rather

of a mixed type, whereas in virtual shear experiment fracture predominantly occurs in mode II.

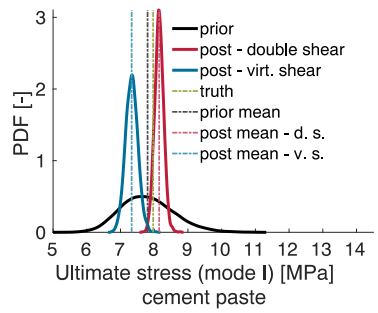

(a)

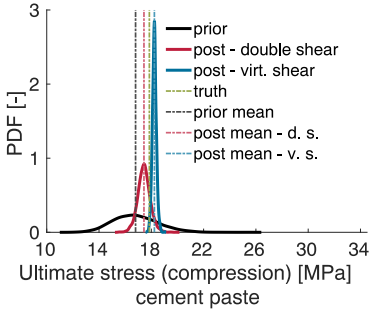

(b)

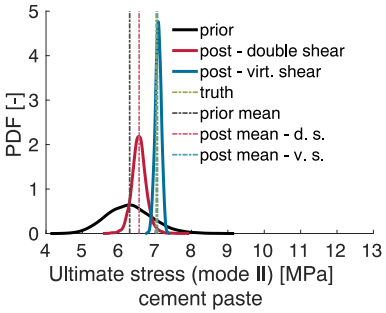

(c)

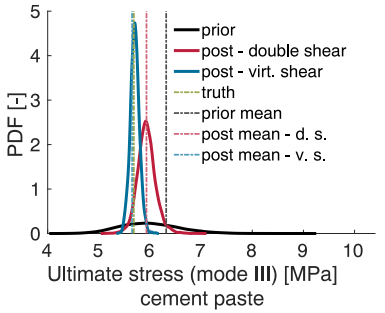

(d)

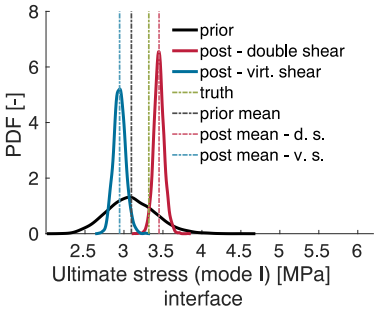

(e)

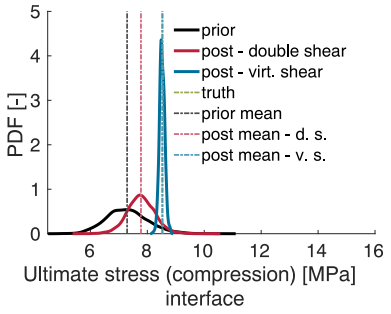

(f)

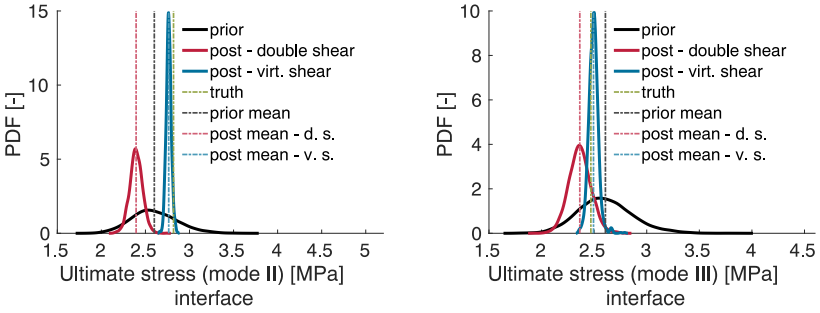

(g) (h)

Figure 5.30: Comparison of posterior PDFs estimated from double shear test and virtual shear test. Prior and posterior PDFs of the ultimate stresses in: a) mode I (cement); b) compression (cement); c) mode II (cement); d) mode III (cement); e) mode I (ITZ); f) compression (ITZ); g) mode II (ITZ); h) mode III (ITZ)

Furthermore, by comparing Figs. 5.30(a)–5.30(d) with Figs. 5.30(e)–5.30(h), one can note that the posterior estimates of the interface properties are more exact than their cement paste counterparts. Namely, the interface transition zone is typically the weakest part of the composite and hence, it is a part which is most prone to cracking. As the macroscopic cracks usually nucleate and propagate over the interface between the aggregate and the surrounding cement paste, it is expected that the observations are more sensitive to the interface parameters, leading to more accurate posterior quantities.

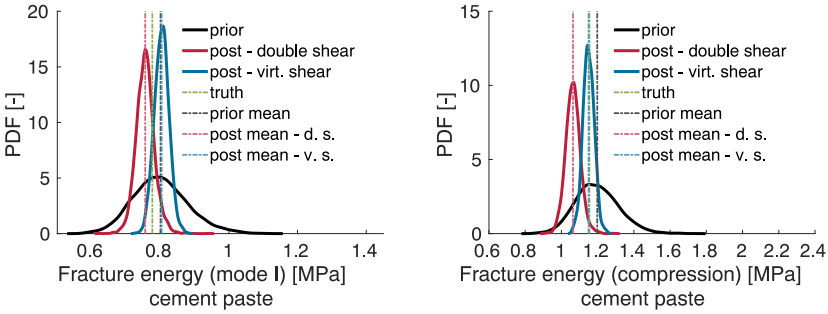

(a) (b)

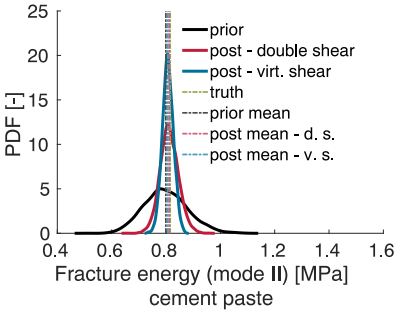

(c)

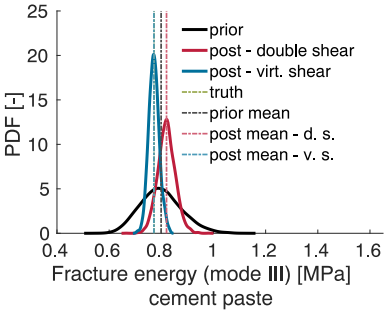

(d)

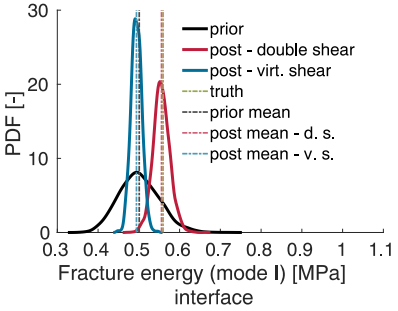

(e)

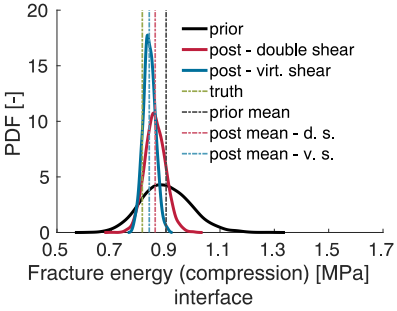

(f)

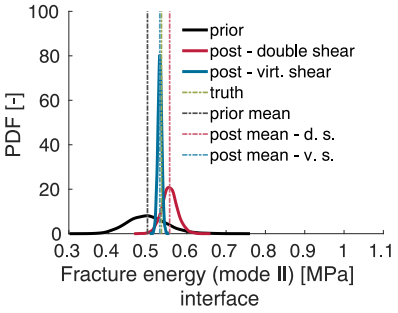

(g)

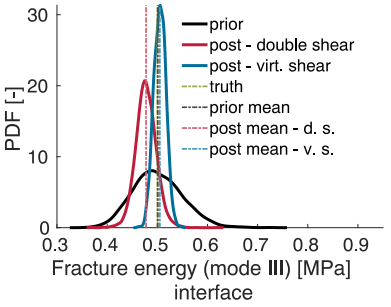

(h)

Figure 5.31: Comparison of posterior PDFs estimated from double shear test and virtual shear test. Prior and posterior PDFs of fracture energies in: a) mode I (cement); b) compression (cement); c) mode II (cement); d) mode III (cement); e) mode I (ITZ); f) compression (ITZ); g) mode II (ITZ); h) mode III (ITZ)

Everything that is stated above regarding the estimates of the ultimate stresses, holds for the estimates of the fracture energies as well. Fracture energies in mode II and III are very sensitive with respect to observations, which is reflected in very accurate estimates for these particular parameters, as shown in Fig. 5.31. Moreover, a very narrow posterior PDF of the fracture energy in mode II for the ITZ confirms that fracture is indeed a shear fracture, with dominant mode II and crack propagation through the interface transition zone.

Table 5.9: Prior and posterior probabilistic description of local properties: mean value and standard deviation of the uncertain softening parameters estimated from virtual shear experiment

Property	Prior		Posterior		True
	Mean	Std. dev.	Mean	Std. dev.	
$\sigma_{u_t,cm}$ [MPa]	7.80	0.78	7.30	0.182	7.968
$\sigma_{u_c,cm}$ [MPa]	16.80	1.68	18.24	0.163	17.850
$\tau_{u_1,cm}$ [MPa]	6.30	0.63	7.08	0.083	7.028
$\tau_{u_2,cm}$ [MPa]	6.30	0.63	5.70	0.088	5.685
$\bar{\bar{G}}_{f_t,cm}$ [N/mm]	0.80	0.08	0.80	0.021	0.777
$\bar{\bar{G}}_{f_c,cm}$ [N/mm]	1.20	0.12	1.15	0.031	1.154
$\bar{\bar{G}}_{f_{\tau_1},cm}$ [N/mm]	0.80	0.08	0.81	0.020	0.815
$\bar{\bar{G}}_{f_{\tau_2},cm}$ [N/mm]	0.80	0.08	0.77	0.020	0.772
$\sigma_{u_t,itz}$ [MPa]	3.10	0.31	2.94	0.077	3.319
$\sigma_{u_c,itz}$ [MPa]	7.30	0.73	8.53	0.096	8.543
$\tau_{u_1,itz}$ [MPa]	2.60	0.26	2.76	0.029	2.819
$\tau_{u_2,itz}$ [MPa]	2.60	0.26	2.49	0.067	2.469
$\bar{\bar{G}}_{f_t,itz}$ [N/mm]	0.50	0.05	0.49	0.013	0.560
$\bar{\bar{G}}_{f_c,itz}$ [N/mm]	0.90	0.09	0.84	0.022	0.814
$\bar{\bar{G}}_{f_{\tau_1},itz}$ [N/mm]	0.50	0.05	0.53	0.005	0.535
$\bar{\bar{G}}_{f_{\tau_2},itz}$ [N/mm]	0.50	0.05	0.51	0.012	0.500

Finally, one can conclude that the proposed virtual shear experiment leads to quite accurate posterior estimates of the fracture properties pertaining to mode II and mode III and the identifiability of the target parameters is significantly improved with respect to double shear experiment with externally bonded CFRP plates.

5.4 Concluding remarks

The aim of the work described in this chapter was to tackle the following issues:

- suitability of the far end supported double shear test with externally bonded CFRP plates for identification of the material parameters of mortar,
- uncertain boundary conditions resulting from the implementation of the actual experiment,
- high dimensionality of the stochastic inverse problem,
- coupling of the finite element solver and the computer program for stochastic analysis in sequential Bayesian inference,
- design of the experiment which improves the identifiability of the parameters of interest.

Double shear experiment introduced in this chapter was originally designed to investigate the bond between mortar and CFRP. Nevertheless, the available experimental data is here employed beyond its initial purpose for estimation of material parameters of mortar. The obtained results are in good agreement with the observational data. Moreover, the fracture pattern from the experiment can be reproduced with the employed lattice model.

Actual experiments often require certain arrangements to facilitate their implementation in testing facilities, such as the addition of a CFRP sheet in the example herein. These arrangements, however, may limit the usability of the experimental data, especially if one wants to use the generated experimental data beyond its initial purpose. The latter often becomes apparent in hindsight, after the experiment takes place. In order to ensure that the experiment meets the requirements of its potential applications, it should be simulated virtually beforehand. Namely, virtual experiments are a great tool for identifying weak aspects of the experimental design and they give an insight into many potential applications for which the data could be used. Moreover, they can be used for validation of the implementation of methods for stochastic parameter identification. Hence, a good practice would be to always adopt the virtual experiments as a first step in the experimental design, prior to investing time and resources into an experiment which has very limited usage.

Despite the shortcomings of the considered experimental setup, i.e. influence of the CFRP sheet on computational reproducibility, this chapter illustrates how loading conditions of a simplified experimental setup can be successfully identified using Bayesian inference methods and exploiting the indirect observations. As a result, the simplified experiment, which does not require modelling of the CFRP plates and sheet, is able to produce a response comparable to the one in the actual test.

Another limiting factor for using actual experimental data from the proposed experiment was the lack of measurement error assessment of the DIC. No amount of postprocessing was able to produce meaningful filtered curves without the knowledge about the magnitude of the measurement noise. Hence, the experimental data was only used qualitatively, whereas the quantitative representation was adopted from numerical simulations of the finite element model.

In the example considered in this chapter, posterior estimates of 34 material parameters and 11 uncertain load curves were sought, which leads to high dimensionality of the stochastic inverse problem. In this case, the use of PCE-based surrogate model was ruled out, as it would require a very high number of numerical simulations to accurately calculate coefficients of the expansion. A combination of EnGKF and the proposed sequential procedure combining offline prediction and online update has shown a good performance not only in terms of accuracy of the posterior estimates, but in terms of computational costs as well.

Most of the meaningful mechanical models are essentially nonlinear and as such they require either implementation of nonlinear Bayesian methods or incremental approach, which gathers one observation or a smaller portion of observations at discrete update steps. If the update steps are sufficiently small, one can achieve linearity (or quasi-linearity) within a particular update step. The implementation of such sequential procedures, however, can often be quite tedious, as it requires coupling of the finite element solver and the code for stochastic analysis. Namely, at each loading step, samples of uncertain input parameters are used for computing corresponding realisations of the finite element model. The resulting data needs to be imported in the software in which the procedure for solving the stochastic inverse problem is implemented. There one carries out the update of the input parameters. As the current state was computed with the prior description of model input parameters, before proceeding to the successive loading step, one needs to recompute the current step with the posterior distribution of the uncertain

model parameters. Only then, one can compute the response at the successive loading step. Such sequential update methods often require the use of restart procedures, which complicate the implementation. In some cases, it is not possible to have both the finite element analysis software and software for stochastic analysis at the same location (e.g. costly numerical simulations are often computed on clusters, compute servers or supercomputers) or the coupling between required computer programs is infeasible. Hence, an alternative method which preserves the sequential nature of the update, while allowing the complete independence between the computer programs for finite element and stochastic analysis is proposed. The obtained results show a good agreement with the observational data.

Lastly, the issue of parameter identifiability given experimental data from two distinct shear experiments has been investigated. One would expect that fracture in double shear experiment with externally bonded CFRP plates is purely a mode II shear sliding. However, the results of Bayesian inference show that observations are sensitive to the majority of parameters, which indicates that fracture is rather of a mixed type. While most of the target parameters are found to converge towards their true values, variance of the posterior distributions is still relatively high in the inelastic region, especially for the fracture energies. On contrary, employing the data from a virtual experiment resembling standard direct shear test, one cannot estimate all target parameters (e.g. parameters pertaining to tension), but the posterior estimates of the fracture parameters pertaining to shear fracture (mode II and III) are found to be more accurate. The dominant fracture mode in the virtual shear experiment is mode II, which is directly reflected in very accurate estimates of the corresponding parameters with increased variance reduction. If one aims to estimate tensile or compression properties as well, better results could be achieved by incorporating the observational data from a tensile or compression test, respectively.

Chapter 6

Concluding remarks and outlook

This chapter summarises the completed work, emphasises the most important findings and gives an outlook on future research.

6.1 Conclusions

This research work studies the concept of identifiability of uncertain parameters in nonlinear mechanical models describing the cracking behaviour of concrete and mortar. The issue of parameter identifiability has been tackled within the framework of Bayesian inference, through experiments simulating the two distinct types of fracture in concrete: tensile and shear fracture.

The former case concerns the investigation of identifiability of material parameters of reinforced concrete given data from a tensile test. The study shows that in order to achieve better posterior estimates of the parameters of interest, observations of a different type need to be included. The choice of the quantities of interest relies upon the following considerations: the experiment needs to be easy to implement in a testing facility at reasonable costs and needs to be in accordance with the nature of a particular target parameter. While the hardening modulus and elasticity limit are well estimated only from a stress-deformation curve, not all target parameters can be

retrieved from a single measurement type. Improvements in the posterior estimates of the ultimate stress and fracture energy are observed once one considers the observations of dissipation due to a particular crack. On the other hand, parameters such as the critical bond stress, which are closely related to the local phenomena, e.g. opening of a particular crack, tend to be more accurately estimated when observations of this type are included. Due to imperfections of the numerical model and the fact that the linear Bayesian update is adopted, the quantities of interest computed with the posterior values of parameters will not match perfectly all of the observed values at once. Hence, it is up to the modeller to evaluate which observations are relevant for the considered engineering problem, e.g. dissipation for the study on seismic safety or stress-deformation curve for the analysis of the material strength.

In the successive example, the identifiability of the material parameters of mortar mesostructure is explored by comparing two shear experiments: a double shear experiment with externally bonded CFRP plates and a virtual shear experiment. The steps that have been taken in order to facilitate the implementation of a double shear test in a testing facility have resulted in a mixed-type fracture rather than a pure shear fracture as one would expect. This caused the observations being sensitive to the majority of the target parameters. On contrary, the virtual shear experiment shows greater sensitivity with respect to shear properties of the material and subsequently, improves their identifiability. In addition, difficulties arising from peculiarities of the experimental setup, e.g. uncertain loading or boundary conditions, are reported and possible solution approaches are given.

Other topics that are tackled within this thesis are the Bayesian estimation of parameters in highly nonlinear mechanical models, computational efficiency in solving the stochastic inverse problems and dealing with high dimensionality of the stochastic problems.

For time dependent nonlinear problems such as the ones analysed in this work, it is highly beneficial to adopt the sequential scheme for parameter estimation. The step-wise approach, with estimates of the uncertain parameters produced at each update step, leads to quasi-linearity within a particular update step, under the assumption that the chosen step size is sufficiently small. This alleviates the need for implementation of the nonlinear filters. Furthermore, a novel approach to sequential update, which fully decouples the computation of model predictions and the online parameter updates, while preserving

the accuracy of the posterior estimates, is proposed and its performance is validated in Chapter 5.

Bayesian update, especially its sequential version, is found to be computationally exhaustive. Nevertheless, it can be accelerated by the use of functional approximations, e.g. via polynomial chaos expansion. The use of PCE approximations, however, may be limiting in case of high dimensionality of a stochastic problem as it requires many simulations of the FE solver to accurately compute the polynomial coefficients. In that case, a more natural choice are sampling methods, such as MCMC or EnKF, the latter being more favourable from the point of view of computational efficiency.

6.2 Outlook

In order to obtain better numerical predictions and posterior estimates of the parameters of interest, possible improvements within the field of computational modelling and parameter estimation can be implemented. Moreover, possible extensions of the mechanical models may lead to a broader range of practical applications.

The 2D model of reinforced concrete introduced in Section 3.2 could be improved by extending it to the 3D space. This would allow a more realistic representation of bond-slip as a full slip field, which is in 2D case reduced merely to a line.

One could model the uncertain model parameters by means of spatially varying random fields instead of random variables utilised herein. Random fields could better capture heterogeneities of the inner structure of concrete, as well as the local bond effects. However, if one desires to update the random fields, many repetitions of the tensile tests would be required in order to obtain meaningful results.

Lattice model introduced in Section 3.3 could be extended to reinforced concrete by implementing the steel bars and modelling the bond between the reinforcement and surrounding concrete. All civil engineering structures made of concrete contain some kind of reinforcement, typically either the classical steel bars or fibres. Modelling of reinforcement would result in a wider practical applicability of the numerical model, especially in the domain of study of structural durability.

In this work, the lattice model was employed for studying the shear behaviour of mortar. However, one could also model the CFRP plates and the bond in order to study the bond behaviour, for which purpose the experiment was intended. One could then identify the bond properties, which would enrich the research on this relatively recent method for repairing existing structures.

The studied problem could also be observed over multiple scales and depending on the research application, the parameters of interest could be either upscaled (e.g. to obtain the homogenised properties of large-scale structures) or downscaled (e.g. to obtain the properties of a single aggregate), in the framework of multi-scale analysis.

As concrete is highly heterogeneous material, to improve the reliability of the parameter estimates one should consider observations from repeated experiments. Testing facilities typically have a limited capability, they are constrained either by the size of specimens or by the number of repetitions of a particular experiment. Hence, one could use the computed tomography scans of different specimens, from which the features could be extracted and classified by the artificial neural networks. In the process of unsupervised learning, many different random mesostructures could be generated and thus, one could perform many repeated experiments. From the perspective of cracking behaviour, such experiments would yield more reliable results compared to virtual experiments with artificially introduced spatial variability.

On a general note, in the context of reliability of parameter identification schemes and following the new initiative of the German Research Foundation (DFG) for long-term storage and management of valuable research data, a recent research challenge pertains to a more comprehensive use of experimental data. A considerable amount of repeated experiments would certainly benefit the field of Bayesian parameter identification, as well as the practical application of it to the study of structural durability. Nevertheless, the question of combining measurements from different testing facilities and overcoming their dependence on the environmental conditions in a particular lab, yet remains unresolved.

List of Figures

List of Tables

List of Symbols

Abbreviations

RV	Random variable
RF	Random field
QoI	Quantity of Interest
CE	Conditional expectation
PDF	Probability density function
MLE	Maximum likelihood estimator
MAP	Maximum a posteriori estimator
MMSE	Minimum mean square error estimator
MC	Monte Carlo method
MCMC	Markov chain Monte Carlo
MH	Metropolis-Hastings algorithm
KF	Kálmán filter
EKF	Extended Kálmán filter
EnKF	Ensemble Kálmán filter
PF	Particle filter
GMKF	Gauss-Markov-Kálmán filter
PCE	Polynomial chaos expansion
SRPCU	Square-root PCE-based GMKF
ANN	Artificial Neural Networks
PINN	Physics-informed neural network
MSE	Mean square error

SA	Sensitivity analysis
ANOVA	Analysis of variance
EnGKF	Generalised ensemble Kálmán filter
FE	Finite element
RC	Reinforced concrete
FPZ	Fracture process zone
DOF	Degree of freedom
FEM	Finite element method
ED	Embedded discontinuity
ED-FEM	Embedded discontinuity finite element method
X-FEM	Extended finite element method
PUFEM	Partition of unity finite element method
CST	Constant strain triangle
BVP	Boundary value problem
CT	Computed tomography
DIC	Digital image correlation
ITZ	Interface transition zone
FEAP	Finite Element Analysis Program
CFRP	Carbon fibre reinforced polymers
ODE	Ordinary differential equation

General notation

a	Scalar
$\boldsymbol{a}$	Vector
$\boldsymbol{A}$	Tensor

Symbols

q	Random variable
$\boldsymbol{q}$	Vector of random variables

$(\Omega, \mathfrak{F}, \mathbb{P})$	Probability space
Ω	Sample space
$\mathfrak{F}$	σ-algebra
$\mathbb{P}$	Probability measure
$\mathcal{Q}$	Parameter space
$\mathcal{Y}$	Measurement space
$\langle q_1, q_2 \rangle_{\mathcal{Q}}$	Inner product
$\|\|q\|\|_{\mathcal{Q}} = \sqrt{q \cdot q}$	Vector norm
$\boldsymbol{u}$	System's response
$L_2(\Omega, \mathfrak{F}, \mathbb{P})$	Hilbert space
$f(\boldsymbol{q})$	Source term
$\mathcal{U}^*$	Dual space
$\mathscr{A}$	Forward model
S	Solution operator
Y_Q	Observation operator
$\boldsymbol{y}$	Observations
$\boldsymbol{\varepsilon}$	Measurement noise
$\boldsymbol{q}_f$	Prediction of random variables
$\boldsymbol{y}_f$	Prediction of the observations
$\boldsymbol{z}_f$	Noisy observations
$\boldsymbol{C}_{\boldsymbol{\varepsilon}}$	Covariance of the measurement noise
Ψ_α	Orthogonal polynomials
θ	Standard Gaussian random variables
$q^{(\alpha)}$	Coefficients of the PCE
$\mathcal{J}_M$	Multi-index set
M	Required number polynomials in PCE
N_p	Maximal degree of polynomials
N_θ	Number of random variables
δ_{ij}	Kronecker delta function
$Var(\boldsymbol{y})$	Total output variance
$D_i(\boldsymbol{y})$	First-order partial variances
$D_{i,j}(\boldsymbol{y})$	Second-order partial variances
S_i	First-order Sobol indices
$S_{i,j}$	Second-order Sobol indices
S_{T_i}	Total sensitivity indices
$\mathbb{E}(\boldsymbol{y})$, μ	Expected or mean value
$\hat{\boldsymbol{z}}$	Noisy observations
$\pi_0(\boldsymbol{q})$	Prior probability density function
$\pi(\boldsymbol{q}\|\hat{\boldsymbol{z}})$	Posterior probability density function
$L(\boldsymbol{q})$, $\pi(\hat{\boldsymbol{z}}\|\boldsymbol{q})$	Likelihood function

$P(\hat{\boldsymbol{z}})$	Normalising constant or evidence
$\mathbb{E}(\boldsymbol{q}\|\mathfrak{B})$, $\mathbb{E}(\boldsymbol{q}\|z_f)$	Conditional expectation
$\mathfrak{B}$	Borel sub-σ-algebra
$P_{\mathfrak{B}}$	Orthogonal projection
$\mathcal{S}$	Space of RVs with finite variance
$\mathcal{S}_{\mathfrak{B}}$	Space of RVs consistent with observations
$\tilde{\boldsymbol{q}}$	Optimal parameters satisfying the MMSE minimisation
$\boldsymbol{q}_p$, $P_{\mathfrak{B}}\boldsymbol{q}$	Projected component of the vector of RVs
$\boldsymbol{q}_o$, $(I - P_{\mathfrak{B}})\boldsymbol{q}$	Orthogonal component of the vector of RVs
$\boldsymbol{q}_a$	Vector of posterior RVs
φ	Measurable map
$\boldsymbol{K}$	Kálmán gain
$\dagger$	Pseudo-inverse
$\boldsymbol{C}_{\boldsymbol{q}_f,\boldsymbol{y}_f}$	Covariance of RVs and predicted observations
$\boldsymbol{C}_{\boldsymbol{y}_f}$	Covariance of observations
$\boldsymbol{C}_{\boldsymbol{\varepsilon}}$	Covariance of measurement error
$\tilde{\boldsymbol{q}}_f$	Fluctuating part of RVs
$\tilde{\boldsymbol{z}}_f$	Fluctuating part of predicted observations
$\bar{\boldsymbol{q}}_f$	Mean of RVs
α	Multi-index
$\Psi_\alpha(\boldsymbol{\theta}(\omega))$	PCE basis of RVs
$\Psi_\alpha(\boldsymbol{\xi}(\eta))$	PCE basis of measurement error
$\Psi_\gamma(\boldsymbol{\theta}, \boldsymbol{\xi})$	Extended PCE basis
$\boldsymbol{q}_f^{(\gamma)}$	PCE coefficients of predicted uncertain parameters
$\boldsymbol{y}^{(\gamma)}$	PCE coefficients of predicted observations
$\boldsymbol{e}^{(\gamma)}$	PCE coefficients of measurement error
$\boldsymbol{q}_a^{(\gamma)}$	PCE coefficients of updated uncertain parameters
$\boldsymbol{Q}_f$	Ensemble of predicted uncertain parameters
$\boldsymbol{Y}_f$	Ensemble of predicted observations
$\boldsymbol{E}$	Ensemble of measurement errors
$\hat{\boldsymbol{Z}}$	Ensemble of actual noisy observations
$\hat{\boldsymbol{Z}}_f$	Ensemble of predicted noisy observations
$\boldsymbol{Q}_a$	Ensemble of updated uncertain parameters
$\boldsymbol{P}$, $\boldsymbol{R}$, $\boldsymbol{F}$	Matrices in nonlinear GMKF formulation
t_k	Discrete update steps
N_t	Number of update steps
N	Number of samples
n	Number of linear segments
β_0	y-intercept
Δ_j	Location of the slope change

β_j	Coefficients of the piecewise-linear function
$[a, b]$	Bounds of the uniform distribution
$\mathcal{U}(a, b)$	Uniform probability distribution
$c(\omega)$	Samples of coefficients of the piecewise-linear function
$\bar{\beta}$	Mean of the deterministic interpolation coefficients
$l\mathcal{N}(\mu_q, \boldsymbol{C}_q)$	Lognormal probability distribution
$\boldsymbol{Y}_{fe}$	Forecast of evolution
$\boldsymbol{G}^{(k)}$	Pseudo-Kálmán gain relating $\boldsymbol{Q}_f^{(0)}$ to $\boldsymbol{Y}_{fe}^{(k)}$
$\boldsymbol{W}^{(k)}$	Pseudo-Kálmán gain relating $\boldsymbol{Q}_f^{(k)}$ to $\boldsymbol{Y}_f^{(k)}$
Ω^e	Finite element domain
$\bar{\boldsymbol{D}}$	Damage compliance tensor for hardening
$\bar{\xi}$	Strain-like hardening variable
$\bar{\phi}(\boldsymbol{\sigma}, \bar{q}(\bar{\xi}))$	Damage function for hardening
$\boldsymbol{\sigma}$	Stress field
$\boldsymbol{D}^e$	Elastic compliance tensor for the bulk material
E^c	Young's modulus for concrete
$\bar{\sigma}_f$	Elasticity limit
$\bar{q}(\bar{\xi})$	Stress-like hardening variable
$\bar{K}$	Hardening modulus
σ_{pr}	Principal stress
$\boldsymbol{t}$	Traction at discontinuity
$\boldsymbol{\alpha}^c$	Crack opening
$\bar{\bar{\boldsymbol{Q}}}$	Damage compliance tensor at discontinuity
$\boldsymbol{n}$	Normal component of traction at discontinuity
$\boldsymbol{m}$	Tangential component of traction at discontinuity
$\bar{\bar{\phi}}_1(\boldsymbol{t}, \bar{\bar{q}}(\bar{\bar{\xi}}))$	Damage function for softening (mode I)
$\bar{\bar{\phi}}_2(\boldsymbol{t}, \bar{\bar{q}}(\bar{\bar{\xi}}))$	Damage function for softening (mode II)
$\bar{\bar{\sigma}}_s$	Ultimate stress in shear
$\bar{\bar{\sigma}}_f$	Ultimate stress in tension
$\bar{\bar{\xi}}$	Strain-like softening variable
$\bar{\bar{q}}(\bar{\bar{\xi}})$	Traction-like softening variable
$\bar{\bar{\beta}}^c$	Slope of the softening curve
$\boldsymbol{u}(\boldsymbol{x})$	FE approximation of displacement field
$\boldsymbol{d}^c$	Concrete nodal displacements for standard DOFs
$\boldsymbol{N}$	Standard FE shape functions
$\boldsymbol{M}$	Incompatible shape functions
H_Γ	Heaviside function
$\boldsymbol{\epsilon}^c(\boldsymbol{x})$	Strain field in concrete

$\boldsymbol{B}$	Derivatives of the standard FE shape functions
$\boldsymbol{G}_r$	Derivatives of the incompatible shape functions
$\bar{\boldsymbol{G}}_r$	Regular part of the $\boldsymbol{G}_r$ operator
$\bar{\bar{\boldsymbol{G}}}_r$	Singular part of the $\boldsymbol{G}_r$ operator
Γ_s	Crack discontinuity surface
δ_{Γ_s}	Dirac delta function centered at Γ_s
$\psi(\boldsymbol{\varepsilon}, \boldsymbol{D}, \xi)$	Helmholtz free energy
$\psi(\boldsymbol{\varepsilon}, \bar{\boldsymbol{D}}, \bar{\xi})$	Regular part of the Helmholtz free energy
$\psi(\boldsymbol{\alpha}^c, \bar{\bar{\boldsymbol{Q}}}, \bar{\bar{\xi}})$	Irregular part of the Helmholtz free energy
$D^d(\boldsymbol{\varepsilon}, \bar{\boldsymbol{D}}, \bar{\xi}, \boldsymbol{\alpha}^c, \bar{\bar{\boldsymbol{Q}}}, \bar{\bar{\xi}})$	Total dissipation due to damage
G_f	Fracture energy
l_{Γ_s}	Length of the discontinuity
t_{loc}	Start of the localisation
$\boldsymbol{\alpha}^{bs}$	Nodal bond-slip
$\bar{\bar{\alpha}}^{bs}$	FE approximation of bond-slip
$\bar{\bar{\boldsymbol{D}}}$	Damage compliance for bond-slip
$\bar{\bar{\xi}}$	Hardening displacement-like variable for bond-slip
$\bar{\bar{K}}$	Hardening modulus for bond-slip
$D^{bs}(\bar{\bar{\alpha}}^{bs}, \bar{\bar{\xi}})$	Dissipation due to bond-slip
$\bar{\bar{q}}(\bar{\bar{\xi}})$	Stress-like hardening variable for bond-slip
Γ_{bs}	Bond-slip surface
$\Phi(\boldsymbol{x})$	Enrichment function
$\boldsymbol{\psi}(\boldsymbol{x})$	Enriched shape functions
$\bar{\boldsymbol{y}}$	Location of the reinforcement bar
N_e	Number of finite elements
$\mathbb{A}_{e=1}^{N_e}$	Finite element assembly operator
$G^{int,e}$	Virtual work of the internal forces
$G^{ext,e}$	Virtual work of the external forces
$\boldsymbol{b}$	Body forces
$\boldsymbol{t}_{\Gamma_\sigma}$	Traction acting at the specimen boundary
$\boldsymbol{w}$	Virtual displacement field
$\boldsymbol{w}_a^c$	Virtual displacements of concrete
$\boldsymbol{w}_a^{bs}$	Virtual bond-slip displacements
$\boldsymbol{f}_a^{cs,int}$	Vector of internal forces - concrete & steel
$\boldsymbol{f}_a^{sbs,int}$	Vector of internal forces - steel & bond-slip
$\boldsymbol{f}_a^{ext}$	Vector of external forces
$\boldsymbol{r}^{cs}$	Residual vector - concrete & steel
$\boldsymbol{f}_a^{c,int}$	Vector of internal forces - concrete
$\boldsymbol{f}_a^{s,int}$	Vector of internal forces - steel

$\boldsymbol{r}^{sbs}$	Residual vector - steel & bond-slip
$\boldsymbol{f}_a^{bs,int}$	Vector of internal forces - bond-slip
u	Nodal displacements of Timoshenko beam in x-dir.
v	Nodal displacements of Timoshenko beam in y-dir.
w	Nodal displacements of Timoshenko beam in z-dir.
φ	Nodal rotations of Timoshenko beam around x-axis
ψ	Nodal rotations of Timoshenko beam around y-axis
θ	Nodal rotations of Timoshenko beam around z-axis
α_u	Crack opening in mode I
α_v	Crack opening in mode II
α_w	Crack opening in mode III
$\bar{\sigma}_u$	Yield stress in mode I
$\bar{\tau}_v$	Yield stress in mode II
$\bar{\tau}_w$	Yield stress in mode III
$\bar{\xi}_u$	Strain-like hardening variable in mode I
$\bar{\xi}_v$	Strain-like hardening variable in mode II
$\bar{\xi}_w$	Strain-like hardening variable in mode III
$\bar{q}_u(\bar{\xi}_u)$	Stress-like hardening variable in mode I
$\bar{q}_v(\bar{\xi}_v)$	Stress-like hardening variable in mode II
$\bar{q}_w(\bar{\xi}_w)$	Stress-like hardening variable in mode III
K_c	Hardening modulus for compression
K_{τ_1}	Hardening modulus for shear (mode II)
K_{τ_2}	Hardening modulus for shear (mode III)
$\bar{\phi}_u(\bar{\sigma}_y, \bar{q}_u(\bar{\xi}_u))$	Yield function for mode I
$\bar{\phi}_v(\bar{\tau}_{y_1}, \bar{q}_v(\bar{\xi}_v))$	Yield function for mode I
$\bar{\phi}_w(\bar{\tau}_{y_2}, \bar{q}_w(\bar{\xi}_w))$	Yield function for mode I
t_u	Traction in mode I
t_v	Traction in mode II
t_w	Traction in mode III
$\bar{\bar{\phi}}_u(t_u, \bar{\bar{q}}_u(\bar{\bar{\xi}}_u))$	Damage function for mode I fracture
$\bar{\bar{\phi}}_v(t_v, \bar{\bar{q}}_v(\bar{\bar{\xi}}_v))$	Damage function for mode II fracture
$\bar{\bar{\phi}}_w(t_w, \bar{\bar{q}}_w(\bar{\bar{\xi}}_w))$	Damage function for mode III fracture
$\bar{\bar{\xi}}_u$	Strain-like softening variable in mode I
$\bar{\bar{\xi}}_v$	Strain-like softening variable in mode II
$\bar{\bar{\xi}}_w$	Strain-like softening variable in mode III
$\bar{\bar{q}}_u(\bar{\bar{\xi}}_u)$	Stress-like softening variable in mode I
$\bar{\bar{q}}_v(\bar{\bar{\xi}}_v)$	Stress-like softening variable in mode II
$\bar{\bar{q}}_w(\bar{\bar{\xi}}_w)$	Stress-like softening variable in mode III
$\bar{\bar{\sigma}}_u$	Ultimate stress in mode I

$\bar{\bar{\tau}}_v$	Ultimate stress in mode II
$\bar{\bar{\tau}}_w$	Ultimate stress in mode III
$\bar{\bar{G}}_{f,u}$	Characteristic unit fracture energy in mode I
$\bar{\bar{G}}_{f,v}$	Characteristic unit fracture energy in mode II
$\bar{\bar{G}}_{f,w}$	Characteristic unit fracture energy in mode III
$\boldsymbol{r}$	Residual vector
$\boldsymbol{f}^{(e),int}$	Vector of internal forces
$\boldsymbol{f}^{ext}$	Vector of external forces
$\boldsymbol{h}^e$	Enhanced part of the residual vector
l_e	Length of the beam element
$\bar{\boldsymbol{G}}$	Regular part of the G operator
$\bar{\boldsymbol{d}}$	Vector of truss bar displacements
$d^s_{x,I}$	Axial displacements of the bar at the left node
$d^s_{x,II}$	Axial displacements of the bar at the right node
$\boldsymbol{T}$	Transformation matrix
$\bar{\boldsymbol{k}}$	Stiffness matrix of the truss bar
$\bar{\boldsymbol{f}}$	Vector of internal forces of the truss bar
$\boldsymbol{C}$	Elasticity tensor
σ^s	Stress in the reinforcement bar
A_s	Cross-section of the reinforcement bar
$\bar{\sigma}_f$	Elasticity limit of concrete
K_h	Hardening modulus of concrete
$\bar{\bar{\sigma}}_f$	Ultimate stress of concrete
$\bar{\bar{G}}_f$	Fracture energy
τ_y	Critical bond stress
K	Bulk modulus of concrete
G	Shear modulus of concrete
E_s	Young's modulus of steel
K_{bs}	Elastic bond modulus
K_{PVC}	Elastic modulus of PVC
A_{bs}	Bond area

Bibliography

[1] Acciaioli, A., Lionello, G., and Baleani, M. Experimentally achievable accuracy using a digital image correlation technique in measuring small-magnitude (<0.1%) homogeneous strain fields. *Materials 11*, 5 (2018).

[2] ACI Committee 408. *ACI 408.2R Report on bond of steel reinforcing bars under cyclic loads.* Tech. rep. American Concrete Institute, 2012.

[3] Adeli, E., Rosić, B., Matthies, H. G., Reinstädler, S., and Dinkler, D. Comparison of Bayesian methods on parameter identification for a viscoplastic model with damage. *Metals 10*, 7 (2020).

[4] Alfaiate, J., and Sluys, L. J. Discontinuous numerical modeling of fracture using embedded discontinuities. In *Proceedings of the VIII International Conference on Computational Plasticity (COMPLAS VIII)* (Barcelona, Spain, 2005), E. Oñate and D. R. J. Owen, Eds.

[5] Ambati, M., Gerasimov, T., and De Lorenzis, L. A review on phase-field models of brittle fracture and a new fast hybrid formulation. *Comput. Mech. 55* (2014), 383–405.

[6] Anderson, B. D. O., and Moore, J. B. *Optimal filtering.* Prentice-Hall, 1979.

[7] Anton, D., and Wessels, H. Identification of material parameters from full-field displacement data using physics-informed neural networks. Preprint available at 10.13140/RG.2.2.24558.89924/1.

[8] Armero, F., and Kim, J. Three-dimensional finite elements with embedded strong discontinuities to model material failure in the infinitesimal range. *Int J Numer Methods Eng 91*, 12 (2012), 1291–1330.

[9] Arnst, M., Ghanem, R., and Soize, C. Identification of Bayesian posteriors for coefficients of chaos expansions. *J. Comput. Phys. 229*, 9 (2010), 3134–3154.

[10] Babuška, I., and Melenk, J. M. The partition of unity method. *Int J Numer Methods Eng 40*, 4 (1997), 727–758.

[11] Balaji Rao, K. Characterisation of large fluctuations in response evolution of reinforced concrete members. In *Proceedings of the International Symposium on Engineering under Uncertainty: Safety Assessment and Management (ISEUSAM - 2012)* (Kolkata, India, 2012), S. Chakraborty and G. Bhattacharya, Eds., Springer, India.

[12] Bassett, R., and Deride, J. Maximum a posteriori estimators as a limit of Bayes estimators. *Math. Program 174*, 1–2 (2019), 129–144.

[13] Bažant, Z. P., Caner, F. C., Carol, I., Adley, M. D., and Akers, S. A. Microplane model M4 for concrete. I: Formulation with work-conjugate deviatoric stress. *J Eng Mech 126*, 9 (2000), 944–953.

[14] Bažant, Z. P., and Gambarova, P. Rough cracks in reinforced concrete. *J. Struct. Div. 106*, 4 (1980), 819–842.

[15] Bažant, Z. P., and Oh, B. H. Crack band theory for fracture of concrete. *Mat. Constr. 16* (1983), 155–177.

[16] Bellman, R., and Åström, K. J. On structural identifiability. *Mathematical Biosciences 7*, 3–4 (1970), 329–339.

[17] Belytschko, T., and Black, T. Elastic crack growth in finite elements with minimal remeshing. *Int J Numer Methods Eng 45*, 5 (1999), 601–620.

[18] Belytschko, T., Moës, N., Usui, S., and Parimi, C. Arbitrary discontinuities in finite elements. *Int J Numer Methods Eng 50*, 4 (2001), 993–1013.

[19] Bishop, C. M. *Pattern Recognition and Machine Learning*, 1st ed. Springer-Verlag New York, 2006.

[20] Boulekbache, B., Hamrat, M., Chemrouk, M., and Amziane, S. Influence of yield stress and compressive strength on direct shear behaviour of steel fibre-reinforced concrete. *Constr Build Mater. 27*, 1 (2012), 6–14.

[21] Boulkertous, A. *Interaction Feu/Ouvrages en béton armé dans le cas d'un incendie confiné: prédiction de la fissuration. Application à la problématique des installations nucléaires.* PhD thesis, ENS Cachan, 2009.

[22] Brancherie, D. *Modèles continus et discrets pour les problèmes de localisation et de rupture fragile et/ou ductile.* PhD thesis, ENS Cachan, 2003.

[23] Brancherie, D., and Ibrahimbegovic, A. Novel anisotropic continuum-discrete damage model capable of representing localized failure. Part I: theoretical formulation and numerical implementation. *Eng. Comput. 26*, 1/2 (2009), 100–127.

[24] Cairns, J. Bond and anchorage of embedded steel reinforcement in *fib* Model Code 2010. *Structural Concrete 16*, 1 (2015), 45–55.

[25] Carpenter, J., Clifford, P., and Fearnhead, P. An improved particle filter for nonlinear problems. *IEEE Proc. Radar Son. Nav. 146*, 1 (1999), 2–7.

[26] Chen, J. F., and Teng, J. G. Anchorage strength models for FRP and steel plates bonded to concrete. *J. Struct. Eng. 127*, 7 (2001), 784–791.

[27] Chib, S., and Greenberg, E. Understanding the Metropolis-Hastings algorithm. *Am Stat 49*, 4 (1995), 327–335.

[28] Chui, C. K., and Chen, G. *Kalman filtering with real-time applications*, 1st ed. Springer-Verlag Berlin, Heidelberg, 1987.

[29] Cope, R. J., Rao, P. V., Clark, L. A., and Norris, P. Modelling of reinforced concrete behaviour for finite element analysis of bridge slabs. In *Numerical Methods for Nonlinear Problems I* (1980), C. Taylor, E. Hinton, and D. R. J. Owen, Eds., pp. 457–470.

[30] Czaderski, C., and Meier, U. EBR strengthening technique for concrete, long-term behaviour and historical survey. *Polymers 10*, 1 (2018).

[31] Daghia, F., de Miranda, S., Ubertini, F., and Viola, E. Estimation of elastic constants of thick laminated plates within a Bayesian framework. *Compos. Struct. 80*, 3 (2007), 461–473.

[32] de Borst, R. Some recent developments in computational modelling of concrete fracture. *Int. J. Fract. 86* (1997), 5–36.

[33] de Borst, R., and Nauta, P. Non-orthogonal cracks in a smeared finite element model. *Eng Comput 2*, 1 (1985), 35–46.

[34] de Borst, R., and Verhoosel, C. V. Gradient damage vs phase-field approaches for fracture: Similarities and differences. *Comput Methods Appl Mech Eng 312* (2016), 78–94.

[35] Der Kiureghian, A., and Ditlevsen, O. Aleatory or epistemic? Does it matter? *Struct. Saf 31*, 2 (2009), 105–112.

[36] Dominguez, N. *Etude de la liaison acier-béton. De la modélisation du phènomène à la formulation d' un élément fini enrichi "Béton Armé"*. PhD thesis, ENS Cachan, 2005.

[37] Dominguez, N., Brancherie, D., Davenne, L., and Ibrahimbegovic, A. Prediction of crack pattern distribution in reinforced concrete by coupling a strong discontinuity model of concrete cracking and a bond-slip of reinforcement model. *Eng Comput 22*, 5/6 (2005), 558–582.

[38] Doucet, A., de Freitas, J. F. G., and Gordon, N. J. *Sequential Monte Carlo Methods in Practice*. Springer-Verlag, 2000.

[39] Dujc, J., Brank, B., and Ibrahimbegovic, A. Quadrilateral finite element with embedded strong discontinuity for failure analysis of solids. *Comput. Model. Eng. Sci. 69*, 3 (2010), 223–260.

[40] Dvorkin, E. N., and Assanelli, A. P. 2D finite elements with displacement interpolated embedded localization lines: The analysis of fracture in frictional materials. *Comput Methods Appl Mech Eng 90*, 1–3 (1991), 829–844.

[41] Engl, H., Hanke, M., and Neubauer, A. *Regularization of inverse problems*. Springer Dordrecht, Kluwer, 2000.

[42] Ernst, O. G., Sprungk, B., and Starkloff, H. J. Bayesian inverse problems and Kálmán filters. In Lecture Notes in Computational Science and Engineering. *Springer, Cham 102* (2014), 133–159.

[43] Evensen, G. *Data Assimilation – The Ensemble Kalman Filter*, 2nd ed. Springer-Verlag Berlin, Heidelberg, 2009.

[44] Evensen, G. The ensemble Kalman filter for combined state and parameter estimation. *IEEE Control Systems Magazine 29*, 3 (2009), 83–104.

[45] Farra, B. *Influence de la résistance du béton et de son adhérence avec l'armature sur la fissuration.* PhD thesis, EPFL, Lausanne, 1995.

[46] Francfort, G. A., and Marigo, J.-J. Revisiting brittle fracture as an energy minimization problem. *J Mech Phys Solids 46*, 8 (1998), 1319–1342.

[47] Furukawa, T., and Pan, J. W. Stochastic identification of elastic constants for anisotropic materials. *Int J Numer Methods Eng 81*, 4 (2010), 429–452.

[48] Gajewski, T., and Garbowski, T. Calibration of concrete parameters based on digital image correlation and inverse analysis. *Arch. Civ. Mech. 14*, 1 (2014), 170–180.

[49] Gao, Z., Xu, X., Su, Y., and Zhang, Q. Experimental analysis of image noise and interpolation bias in digital image correlation. *Opt Lasers Eng 81* (2016), 46–53.

[50] Garbacz, A., Piotrowski, T., Courard, L., and Kwaśniewski, L. On the evaluation of interface quality in concrete repair system by means of impact-echo signal analysis. *Constr Build Mater 134* (2017), 311–323.

[51] Geman, S., and Geman, D. Stochastic relaxation, Gibbs distributions, and the Bayesian restoration of images. *IEEE Transactions on Pattern Analysis and Machine Intelligence 6*, 6 (1984), 721–741.

[52] Glover, K., and Willems, J. C. Parameterizations of linear dynamical systems: Canonical forms and identifiability. *IEEE Trans. Automatic Control 19*, 6 (1974), 640–646.

[53] Godfrey, K. R., and Chapman, M. J. Identifiability and indistinguishability of linear compartmental models. *Math. Comput. Simul. 32*, 3 (1990), 273–295.

[54] Godsill, S., Doucet, A., and West, M. Maximum a posteriori sequence estimation using Monte Carlo particle filters. *Ann. I. Stat. Math. 53* (2001), 82–96.

[55] Gogu, C., Haftka, R., Le Riche, R., Molimard, J., and Vautrin, A. Introduction to the Bayesian approach applied to elastic constants identification. *Am. Inst. Aeronaut. Astronaut. J. 48*, 5 (2010), 893–903.

[56] Goodfellow, I., Bengio, Y., and Courville, A. *Deep learning*. The MIT Press, 2016.

[57] Gordon, N. J., Salmond, D. J., and Smith, A. F. M. Novel approach to nonlinear/non-Gaussian Bayesian state estimation. In *IEE Proceedings F: Radar and Signal Processing* (1993), vol. 140, pp. 107–113.

[58] Green, P. J. Reversible jump Markov chain Monte Carlo computation and Bayesian model determination. *Biometrika 82*, 4 (1995), 711–732.

[59] Grewal, M. S., and Glover, K. Identifiability of linear and nonlinear dynamical systems. *IEEE Trans. Automatic Control 21*, 6 (1976), 833–837.

[60] Griffith, A., and Eng, M. VI. The phenomena of rupture and flow in solids. *Philosophical Transactions of the Royal Society of London. Series A 221* (1921), 163–198.

[61] Gupta, A. K., and Akbar, H. Cracking in reinforced concrete analysis. *J. Struct. Eng. 110*, 8 (1984), 1735–1746.

[62] Hastings, W. K. Monte Carlo sampling methods using Markov chains and their applications. *Biometrika 57*, 1 (1970), 97–109.

[63] Herrmann, H. J., Hansen, H., and Roux, S. Fracture of disordered, elastic lattices in two dimensions. *Phys. Rev. B 39*, 1 (1989), 637–648.

[64] Hinze, M., Xiao, S., Schmidt, A., and Nowak, W. Experimental evaluation and uncertainty quantification for a fractional viscoelastic model of salt concrete. *Mech Time-Depend Mater 27* (2022), 139–162.

[65] Hoeffding, W. A class of statistics with asymptotically normal distribution. *Ann. Math. Statist. 19*, 3 (1948), 293–325.

[66] Homma, T., and Saltelli, A. Importance measures in global sensitivity analysis of nonlinear models. *Reliab. Eng. Syst. Saf. 52*, 1 (1996), 1–17.

[67] Hrennikoff, A. Solution of problems of elasticity by the framework method. *J. Appl. Mech. 8*, 4 (1941), 169–175.

[68] Huang, L., Chi, Y., Xu, L., and Deng, F. A thermodynamics-based damage-plasticity model for bond stress-slip relationship of steel reinforcement embedded in fiber reinforced concrete. *Eng. Struct. 180* (2019), 762–778.

[69] Ibrahimbegovic, A. *Nonlinear solid mechanics: Theoretical formulations and finite element solution methods.* Springer Dordrecht, 2009.

[70] Ibrahimbegovic, A., Boulkertous, A., Davenne, L., and Brancherie, D. Modelling of reinforced-concrete structures providing crack-spacing based on X-FEM, ED-FEM and novel operator split solution procedure. *Int J Numer Methods Eng 83*, 4 (2010), 452–481.

[71] Ibrahimbegovic, A., Matthies, H. G., and Karavelić, E. Reduced model of macro-scale stochastic plasticity identification by Bayesian inference: Application to quasi-brittle failure of concrete. *Comput Methods Appl Mech Eng 372* (2020).

[72] Ibrahimbegovic, A., and Melnyk, S. Embedded discontinuity finite element method for modelling of localised failure in heterogeneous materials with structured mesh: an alternative to extended finite element method. *Comput. Mech. 40*, 1 (2007), 149–155.

[73] Ibrahimbegovic, A., Melnyk, S., Hautefeuille, M., Colliat, J.-B., and Kučerová, A. Modèles numériques multi-échelles du comportement anélastique des matériaux hétérogènes et prise en compte des aspects probabilistes. In *Archives ouvertes du 8e Colloque national en calcul des structures 21-25 mai 2007* (2007), pp. 1–15.

[74] Ibrahimbegovic, A., and Wilson, E. A modified method of incompatible modes. *Communications in Applied Numerical Methods 7*, 3 (1991), 187–194.

[75] Iglesias, M. A., Law, K. J. H., and Stuart, A. M. Ensemble Kálmán methods for inverse problems. *Inverse Problems 29*, 4 (2013).

[76] Ingraffea, A. R., and Saouma, V. Numerical modeling of discrete crack propagation in reinforced and plain concrete. In *Fracture mechanics of concrete: Structural application and numerical calculation. Engineering Application of Fracture Mechanics*, G. C. Sih and A. DiTommaso, Eds., vol. 4. Springer, Dordrecht, 1985, pp. 171–225.

[77] Isenberg, J. Progressing from least squares to Bayesian estimation. In *Proceedings of the 1979 ACME Design Engineering Technical Conference* (New York, 1979), pp. 1–11.

[78] Janouchová, E., Kučerová, A., Sýkora, J., Vorel, J., and Wan-Wendner, R. Robust probabilistic calibration of a stochastic lattice discrete particle model for concrete. *Eng Struct 236* (2021).

[79] Janouchová, E., and Kučerová, A. Bayesian inference of heterogeneous viscoplastic material parameters. *Acta Polytechnica CTU Proceedings 15* (2018), 41–45.

[80] Jasiński, R., Stebel, K., and Domin, J. Application of the DIC technique to remote control of the hydraulic load system. *Remote Sens 12*, 21 (2020).

[81] Jazwinski, A. H. *Stochastic Processes and Filtering Theory.* Academic Press, Inc., New York, 1970.

[82] Jirásek, M. Comparative study on finite elements with embedded discontinuities. *Comput Methods Appl Mech Eng 188*, 1–3 (2000), 307–330.

[83] Jirásek, M., and Belytschko, T. Computational resolution of strong discontinuities. In *Proceedings of Fifth World Congress on Computational Mechanics, WCCM V* (Vienna, Austria, 2002), H. A. Mang, F. G. Rammerstorfer, and J. Eberhardsteiner, Eds.

[84] Jirásek, M. Modelling of localized damage and fracture in quasibrittle materials. In *Continuous and Discontinuous Modelling of Cohesive-Frictional Materials. Lecture Notes in Physics*, P. A. Vermeer, H. J. Herrmann, S. Luding, W. Ehlers, S. Diebels, and E. Ramm, Eds. Springer Berlin, Heidelberg, 2001, pp. 17–29.

[85] JSCE-G-533. Test method for shear strength of steel fiber reinforced concrete. In *Standard Specifications for Concrete Structures, Test Methods and Specifications.* JSCE: Tokyo, Japan, 2005, p. 362.

[86] Kaipio, J., and Somersalo, E. *Statistical and Computational Inverse Problems, Vol. 160 of Applied Mathematical Sciences.* Springer-Verlag New York, 2005.

[87] Kálmán, R. E. A new approach to linear filtering and prediction problems. *Trans. ASME J. Basic Eng. 82*, 1 (1960), 35–45.

[88] Karavelić, E., Nikolić, M., Ibrahimbegovic, A., and Kurtović, A. Concrete meso-scale model with full set of 3D failure modes with random distribution of aggregate and cement phase. Part I: Formulation and numerical implementation. *Comput Methods Appl Mech Eng 344* (2019), 1051–1072.

[89] Karimpour, A., and Rahmatalla, S. Identification of structural parameters and boundary conditions using a minimum number of measurement points. *Front. Struct. Civ. Eng. 14*, 6 (2020), 1331–1348.

[90] Kay, S. M. *Fundamentals of statistical signal processing: Estimation theory*. Prentice-Hall, Inc., Upper Saddle River, USA, 2005.

[91] Koutsourelakis, P. S. A novel Bayesian strategy for the identification of spatially varying material properties and model validation: an application to static elastography. *Int J Numer Methods Eng 91*, 3 (2012), 249–268.

[92] Kožar, I., Bede, N., Bogdanić, A., and Mrakovčić, S. Data driven inverse stochastic models for fiber reinforced concrete. *Coupled Systems Mechanics 10*, 6 (2021), 509–520.

[93] Kožar, I., Torić Malić, N., Simonetti, D., and Smolčić, v. Bond-slip parameter estimation in fiber reinforced concrete at failure using inverse stochastic model. *Eng. Fail. Anal. 104* (2019), 84–95.

[94] Král, P., Hokeš, F., Hušek, Kala, J., and Hradil, P. Optimization-based inverse identification of the parameters of a concrete cap material model. *IOP Conf. Ser.: Mater. Sci. Eng. 245* (2017).

[95] Král, P., Hušek, M., Hradil, P., Kala, J., and Maňas, P. Optimization of the material parameters of the continuous surface cap model for concrete. In *2017 International Conference on Military Technologies (ICMT)* (Brno, Czech Republic, 2017), pp. 298–302.

[96] Kučerová, A., and Lepš, M. Soft computing-based calibration of microplane M4 model parameters: Methodology and validation. *Adv. Eng. Softw. 72* (2014), 226–235.

[97] Kučerová, A., Sýkora, J., Rosić, B. V., and Matthies, H. G. Acceleration of uncertainty updating in the description of transport processes in heterogeneous materials. *J. Comput. Appl. Math. 236*, 18 (2012), 4862–4872.

[98] Kučerová, A., Brancherie, D., Ibrahimbegovic, A., Zeman, J., and Bittnar, Z. Novel anisotropic continuum-discrete damage model capable of representing localized failure. Part II: Identification from tests under heterogeneous stress field. *Eng. Comput. 26*, 1–2 (2009), 128–144.

[99] Laplace, P. S. Mémoire sur la Probabilité des Causes par les Évènements. Mémoires de l'Académie royale des sciences de Paris. *Divers Savan 6* (1774), 27–65.

[100] Lemaitre, J., and Chaboche, J. L. *Mecanique des materiaux solides*, 2nd ed. Dunod, 1988.

[101] Linder, C., and Armero, F. Finite elements with embedded strong discontinuities for the modeling of failure in solids. *Int J Numer Methods Eng 72* (2007), 1391–1433.

[102] Litvinenko, A., and Matthies, H. G. Inverse problems and uncertainty quantification. *arXiv:1312.5048* (2014).

[103] Liu, J. S. *Monte Carlo Strategies in Scientific Computing*. Springer-Verlag New York, 2003.

[104] Ljung, L., and Glad, T. On global identifiability for arbitrary model parameterizations. *Automatica 30*, 2 (1994), 265–276.

[105] Lubliner, J. *Plasticity Theory*. Macmillan, New York, USA, 1990.

[106] Luo, Y. An efficient 3D Timoshenko beam element with consistent shape functions. *Adv. Theor. Appl. Mech. 1*, 3 (2008), 95–106.

[107] Mareš, T., Janouchová, E., and Kučerová, A. Artificial neural networks in calibration of nonlinear mechanical models. *Adv. Eng. Softw. 95* (2016), 68–81.

[108] Matthies, H. G. Uncertainty quantification and Bayesian inversion. In *Encyclopedia of Computational Mechanics Second Edition. Part 1. Fundamentals*, E. Stein, R. Borst, and T. J. R. Hughes, Eds. John Wiley & Sons, 2017, pp. 1–51.

[109] Matthies, H. G., Zander, E., Rosić, B. V., and Litvinenko, A. Bayesian parameter estimation via filtering and functional approximations. *arXiv: 1611.09293* (2016).

[110] Matthies, H. G., Zander, E., Rosić, B. V., and Litvinenko, A. Parameter estimation via conditional expectation: a Bayesian inversion. *Adv. Model. Simul. Eng. Sci. 3*, 24 (2016).

[111] Matthies, H. G., Zander, E., Rosić, B. V., Litvinenko, A., and Pajonk, O. Inverse problems in a Bayesian setting. In *Computational Methods for Solids and Fluids. Computational Methods in Applied Sciences*, A. Ibrahimbegovic, Ed., vol. 41. Springer Cham, 2016, pp. 245–286.

[112] Mazzoleni, P. *Uncertainty estimation and reduction in digital image correlation measurements*. PhD thesis, Politecnico di Milano, 2013.

[113] Melenk, J. M., and Babuška, I. The partition of unity finite element method: Basic theory and applications. *Comput Methods Appl Mech Eng 139*, 1–4 (1996), 289–314.

[114] Metropolis, N., Rosenbluth, A. W., Rosenbluth, M. N., Teller, A. H., and Teller, E. Equation of state calculations by fast computing machines. *J. Chem. Phys. 21*, 6 (1953), 1087–1092.

[115] Metropolis, N., and Ulam, S. The Monte Carlo method. *J Am Stat Assoc 44*, 247 (1949), 335–341.

[116] Miehe, C., Hofacker, M., and Welschinger, F. A phase field model for rate-independent crack propagation: Robust algorithmic implementation based on operator splits. *Comput Methods Appl Mech Eng 199*, 45–48 (2010), 2765–2778.

[117] Moës, N., and Belytschko, T. Extended finite element method for cohesive crack growth. *Eng Fract Mech 69*, 7 (2002), 813–833.

[118] Moës, N., Dolbow, J., and Belytschko, T. A finite element for crack growth without remeshing. *Int J Numer Methods Eng 46*, 1 (1999), 131–150.

[119] Morbiducci, R. Non-linear parameter identification of models for masonry. *Int. J. Solids Struct. 40*, 15 (2003), 4071–4090.

[120] Mosler, J. On the modeling of highly localized deformations induced by material failure: The strong discontinuity approach. *Arch Comput Methods Eng 11* (2004), 389–446.

[121] Ngo, D., and Scordelis, A. C. Finite element analysis of reinforced concrete beams. *ACI Journal Proceedings 64*, 3 (1967), 152–163.

[122] Nikolić, M. *Rock Mechanics, Failure Phenomena with Pre-Existing Cracks and Internal Fluid Flow through Cracks.* PhD thesis, ENS Cachan and University of Split, 2015.

[123] Nikolić, M., Do, X. N., Ibrahimbegovic, A., and Nikolić, Ž. Crack propagation in dynamics by embedded strong discontinuity approach: Enhanced solid versus discrete lattice model. *Comput Methods Appl Mech Eng 340* (2018), 480–499.

[124] Nikolić, M., and Ibrahimbegovic, A. Rock mechanics model capable of representing initial heterogeneities and full set of 3D failure mechanisms. *Comput Methods Appl Mech Eng 290* (2015), 209–227.

[125] Nikolić, M., Ibrahimbegovic, A., and Miščević, P. Brittle and ductile failure of rocks: Embedded discontinuity approach for representing mode I and mode II failure mechanisms. *Int J Numer Methods Eng 102*, 8 (2015), 1507–1526.

[126] Nikolić, M., Karavelić, E., Ibrahimbegovic, A., and Miščević, P. Lattice element models and their peculiarities. *Arch Computat Methods Eng 25*, 3 (2018), 753–784.

[127] Nilson, A. H. Nonlinear analysis of reinforced concrete by the finite element method. *J. Am. Concrete Inst. 65*, 9 (1968), 757–766.

[128] Nolan, S., Smerzi, A., and Pezzè, L. A machine learning approach to Bayesian parameter estimation. *npj Quantum Inf 7* (2021).

[129] Oliver, J. Continuum modeling of strong discontinuities in solid mechanics using damage models. *Comput. Mech. 17* (1995), 49–61.

[130] Oliver, J., Huespe, A. E., and Dias, I. F. Strain localization, strong discontinuities and material fracture: Matches and mismatches. *Comput Methods Appl Mech Eng 241–244* (2012), 323–336.

[131] Oliver, J., Huespe, A. E., and Sánchez, P. J. A comparative study on finite elements for capturing strong discontinuities: E-FEM vs X-FEM. *Comput Methods Appl Mech Eng 195*, 37–40 (2006), 4732–4752.

[132] Opper, M. On-line versus off-line learning from random examples: General results. *Phys. Rev. Lett. 77*, 22 (1996).

[133] Opper, M., and Winther, O. A Bayesian approach to on-line learning. In *On-line Learning in Neural Networks* (Cambridge University Press, 1999), D. Saad, Ed., pp. 363–378.

[134] Ostoja-Starzewski, M. Lattice models in micromechanics. *Appl. Mech. Rev. 55*, 1 (2002), 35–60.

[135] Pajonk, O. *Stochastic Spectral Methods for Linear Bayesian Inference.* PhD thesis, TU Braunschweig, 2012.

[136] Pajonk, O., Rosić, B. V., Litvinenko, A., and Matthies, H. G. A deterministic filter for non-Gaussian state estimation. *Proc. Appl. Math. and Mech. (PAMM) 11* (2011), 703–704.

[137] Pajonk, O., Rosić, B. V., Litvinenko, A., and Matthies, H. G. A deterministic filter for non-Gaussian state estimation – Applications to dynamical system estimation with noisy measurements. *Physica D: Nonlinear Phenomena 241*, 7 (2012), 775–788.

[138] Pajonk, O., Rosić, B. V., and Matthies, H. G. Sampling-free linear Bayesian updating of model state and parameters using a square root approach. *Computers & Geosciences 55* (2013), 70–83.

[139] Ragueneau, F., Dominguez, N., and Ibrahimbegovic, A. Thermodynamic-based interface model for cohesive brittle materials: Application to bond slip in RC structures. *Comput Methods Appl Mech Eng 195*, 52 (2006), 7249–7263.

[140] Rappel, H., Beex, L. A. A., and Bordas, S. P. A. Bayesian inference to identify parameters in viscoelasticity. *Mech Time-Depend Mater 22*, 2 (2018), 221–258.

[141] Rappel, H., Beex, L. A. A., Hale, J. S., and Bordas, S. P. A. Bayesian inference for the stochastic identification of elastoplastic material parameters: Introduction, misconceptions and insights. *arXiv:1606.02422* (2017).

[142] Rappel, H., Beex, L. A. A., Noels, L., and Bordas, S. P. A. Identifying elastoplastic parameters with Bayes' theorem considering output error, input error and model uncertainty. *Probabilistic Eng. Mech. 55* (2019), 28–41.

[143] Rashid, Y. R. Analyis of pre-stressed concrete pressure vessels. *Nucl. Eng. Design 7*, 4 (1968), 334–355.

[144] Rosić, B. V. Litvinenko, A., Pajonk, O., and Matthies, H. G. Sampling-free linear Bayesian update of polynomial chaos representations. *J. Comput. Phys. 231*, 17 (2012), 5761–5787.

[145] Rosić, B. V., Kučerová, A., Sýkora, J., Pajonk, O., Litvinenko, A., and Matthies, H. G. Parameter identification in a probabilistic setting. *Eng. Struct. 50* (2013), 179–196.

[146] Rots, J. G., and Blaauwendraad, J. Crack models for concrete: discrete or smeared? Fixed, multi-directional or rotating? *HERON 34*, 1 (1989), 1–59.

[147] Rots, J. G., Nauta, P., Kusters, G. M. A., and Blaauwendraad, J. Smeared crack approach and fracture localization in concrete. *HERON 30*, 1 (1985), 1–48.

[148] Rukavina, T., Ibrahimbegovic, A., and Kozar, I. Multi-scale representation of plastic deformation in fiber-reinforced materials: application to reinforced concrete. *Lat. Am. J. Solids Struct. 16*, 7 (2018).

[149] Rukavina, T., Ibrahimbegovic, A., and Kozar, I. Fiber-reinforced brittle material fracture models capable of capturing a complete set of failure modes including fiber pull-out. *Comput Methods Appl Mech Eng 355* (2019), 157–192.

[150] Saksala, T., Brancherie, D., Harari, I., and Ibrahimbegovic, A. Combined continuum damage-embedded discontinuity model for explicit dynamic fracture analyses of quasi-brittle materials. *Int J Numer Methods Eng 101*, 3 (2015), 230–250.

[151] Sarfaraz, M. S., Rosić, B. V., Matthies, H. G., and Ibrahimbegovic, A. Bayesian stochastic multi-scale analysis via energy considerations. *Adv. Model. Simul. Eng. Sci. 7*, 50 (2020).

[152] Sarhosis, V., and Sheng, Y. Identification of material parameters for modeling of masonry structures. *Eng. Struct. 60* (2014), 100–110.

[153] Schiehlen, W., and Wedig, W. *Analysis and Estimation of Stochastic Mechanical Systems*, 1st ed. Springer Vienna, 1988.

[154] Schlangen, E. Computational aspects of fracture simulations with lattice models. In *Proceedings FRAMCOS-2* (Zürich, Switzerland, 1995), F. H. Wittmann, Ed., AEDIFICATIO Publishers, Freiburg, Germany, pp. 913–928.

[155] Schlangen, E., and Garboczi, E. J. New method for simulating fracture using an elastically uniform random geometry lattice. *Int. J. Eng. Sci. 34* (1996), 1131–1144.

[156] Schlangen, E., and Van Mier, J. G. M. Experimental and numerical analysis of micromechanisms of fracture of cement-based composites. *Cem. Conc. Compos. 14*, 2 (1992), 105–118.

[157] Schlangen, E., and Van Mier, J. G. M. Simple lattice model for numerical simulation of fracture of concrete materials and structures. *Mater. Struct. 25* (1992), 534–542.

[158] Schnur, D. S., and Zabaras, N. An inverse method for determining elastic material properties and a material interface. *Int J Numer Methods Eng 33*, 10 (1992), 2039–2057.

[159] Sevieri, G., Andreini, M., De Falco, A., and Matthies, H. G. Concrete gravity dams model parameters updating using static measurements. *Eng. Struct. 196* (2019).

[160] Sevieri, G., and De Falco, A. Dynamic structural health monitoring for concrete gravity dams based on the Bayesian inference. *J Civil Struct Health Monit 10* (2020), 235–250.

[161] Simo, J. C., Oliver, J., and Armero, F. An analysis of strong discontinuities induced by strain-softening in rate-independent inelastic solids. *Comput. Mech. 12* (1993), 277–296.

[162] Smith, R. C. *Uncertainty Quantification: Theory, Implementation, and Applications*. Society for Industrial and Applied Mathematics, USA, 2013.

[163] Sobol, I. M. Global sensitivity indices for nonlinear mathematical models and their Monte Carlo estimates. *Math Comput Simul, The Second IMACS Seminar on Monte Carlo Methods 55*, 1–3 (2001), 271–280.

[164] Stanić, A., Brank, B., and Brancherie, D. Fracture of quasi-brittle solids by continuum and discrete-crack damage models and embedded discontinuity formulation. *Eng Fract Mech 227* (2020).

[165] Stanić, A., Brank, B., Ibrahimbegovic, A., and Matthies, H. G. Crack propagation simulation without crack tracking algorithm: Embedded discontinuity formulation with incompatible modes. *Comput Methods Appl Mech Eng 386* (2021).

[166] Stanić, A., Brank, B., and Korelc, J. On path-following methods for structural failure problems. *Comput Mech 58* (2016), 281–306.

[167] Stuart, A. M. Inverse problems: A Bayesian perspective. *Acta Numerica 19* (2010), 451–559.

[168] Sukumar, N., Moës, N., Moran, B., and Belytschko, T. Extended finite element method for three-dimensional crack modelling. *Int J Numer Methods Eng 48*, 11 (2000), 1549–1570.

[169] Sullivan, T. J. *Introduction to Uncertainty Quantification*. Springer, Cham, 2015.

[170] Tarantola, A. *Inverse problem theory and methods for model parameter estimation*. SIAM, 2005.

[171] Taylor, R. FEAP: Finite Element Analysis Program. `http://projects.ce.berkeley.edu/feap/`, 2014. Accessed February 18, 2022.

[172] Tierney, L. Markov chains for exploring posterior distributions. *The Annals of Statistics 22*, 4 (1994), 1701–1728.

[173] Tikhonov, A. N. On the stability of inverse problems. *C. R. (Doklady) Acad. Sci. URSS 39* (1943), 176–179.

[174] Tikhonov, A. N. On the solution of incorrectly put problems and the regularisation method. In *Outlines Joint Sympos. Partial Differential Equations (Novosibirsk, 1963)*. Acad. Sci. USSR Siberian Branch, Moscow, 1963, pp. 261–265.

[175] Truesdell, C., and Noll, W. *The Non-Linear Field Theories of Mechanics*. Springer Berlin, Germany, 1965.

[176] Valliappan, S., and Doolan, T. F. Nonlinear stress analysis of reinforced concrete. *J. Struct. Div. 98*, 4 (1972), 885–897.

[177] Van den Hof, P. M. J., Van Doren, J. F. M., and Douma, S. G. Identification of parameters in large scale physical model structures, for the purpose of model-based operations. In *Model-Based Control*, P. Hof, C. Scherer, and P. Heuberger, Eds., vol. 4. Springer, Boston, MA, 2009, pp. 125–143.

[178] Van Doren, J. F. M., Van den Hof, P. M. J., Jansen, J. D., and Bosgra, O. H. Determining identifiable parameterizations for large-scale physical models in reservoir engineering. In *Proc. 17th IFAC World Congress* (2008), M. Chung, P. Misra, and H. Shim, Eds., vol. 41, pp. 11421–11426.

[179] Červenka, J. *Discrete crack modeling in concrete structures.* PhD thesis, Univeristy of Colorado, Boulder, 1994.

[180] Červenka, V. *Inelastic finite element analysis of reinforcement concrete panels under in-plane loads.* PhD thesis, Univeristy of Colorado, Boulder, 1970.

[181] Červenka, V., and Gerstle, K. Inelastic analysis of reinforced concrete panels: Part I. Theory, Part II: Experimental verification. *Int. Assoc. of Bridge and Structural Eng. Publications* (1971,1972), Part I: Vol. 31, pp. 32–45, Part II: Vol. 32, pp. 26–39.

[182] Waeytens, J., and Rosić, B. Comparison of deterministic and probabilistic approaches to identify the dynamic moving load and damages of a reinforced concrete beam. *Appl. Math. Comput. 267* (2015), 3–16.

[183] Walter, E. *Identifiability of Parametric Models.* Pergamon Press, Oxford, 1987.

[184] Washizu, K. *Variational methods in elasticity and plasticity*, 3rd ed. Pergamon Press, New York, 1983.

[185] Wei, Y. M., and Jiang, Z. Estimating parameters of structural models using neural networks. *ERN: Neural Networks & Related Topics* (2020).

[186] Wiener, N. The homogeneous chaos. *Am. J. Math. 60*, 4 (1938), 897–936.

[187] Willam, K., Pramono, E., and Sture, S. Fundamental issues of smeared crack models. In *Proc. SEM-RILEM Int. Conf. on Fracture of Concrete and Rock, S. P. Shah and S. E. Swartz (Eds.)* (1989), pp. 142–157.

[188] Winther, O., and Solla, S. A. Optimal Bayesian online learning. In *Theoretical Aspects of Neural Computation (TANC-97)* (Springer Verlag, Singapore, 1998), K. Y. M. Wong, I. King, and D.-Y. Yeung, Eds.

[189] Wu, J.-Y., Li, F. B., and Xu, S.-L. Extended embedded finite elements with continuous displacement jumps for the modeling of localized failure in solids. *Comput Methods Appl Mech Eng 285* (2015), 346–378.

[190] Wu, T., Rosić, B., De Lorenzis, L., and Matthies, H. G. Parameter identification for phase-field modeling of fracture: a Bayesian approach with sampling-free update. *Comp Mech 67* (2021), 435–453.

[191] Xiu, D. *Numerical methods for stochastic computations - a spectral method approach*. Princeton University Press, 2010.

[192] Xu, L., and Huang, Y. Effects of voids on concrete tensile fracturing: A mesoscale study. *Adv. Mater. Sci. Eng.* (2017), 1–14.

[193] Yao, J., Teng, J. G., and Chen, J. F. Experimental study on FRP-to-concrete bonded joints. *Composites Part B: Engineering 36*, 2 (2005), 99–113.

[194] Yuan, X., Zhu, C., Zheng, W., Hu, J., and Tang, B. Flexure performance of externally bonded CFRP plates-strengthened reinforced concrete members. *Mathematical Problems in Engineering 2020* (2020).

[195] Zainal, S. M. I. S., Hejazi, F., Aziz, F. N. A. A., and Jaafar, M. S. Effects of hybridized synthetic fibers on the shear properties of cement composites. *Materials 13*, 22 (2020).